ELECTROCHEMICAL INVESTIGATION ON ENVIRONMENTAL DEGRADATION OF MAGNESIUM RARE EARTH ALLOYS

A Thesis
Presented in Partial Fulfillment of the Requirements for the
Degree of Master of Science
with a
Major in Metallurgical Engineering
in the
College of Graduate Studies
University of Idaho
by

Jakraphan Ninlachart

Major Professor: Krishnan S. Raja, Ph.D.
Committee Members: Indrajit Charit, Ph.D.; I. Francis Cheng, Ph.D.
Department Administrator: D. Eric Aston, Ph.D.

August 2017

Authorization to Submit Thesis

This thesis of Jakraphan Ninlachart, submitted for the degree of Master of Science with a Major in Metallurgical Engineering and titled "ELECTROCHEMICAL INVESTIGATION ON ENVIRONMENTAL DEGRADATION OF MAGNESIUM RARE EARTH ALLOYS," has been reviewed in final form. Permission, as indicated by the signatures and dates below, is now granted to submit final copies to the College of Graduate Studies for approval.

Major Professor: _____ Date: _____
Krishnan S. Raja, Ph.D.

Committee Members: _____ Date: _____
Indrajit Charit, Ph.D.

_____ Date: _____
I. Francis Cheng, Ph.D.

Department
Administrator: _____ Date: _____
D. Eric Aston, Ph.D.

Abstract

Magnesium rare earth alloys have excellent mechanical properties and good corrosion resistance; as a result, they are used in automobile and aerospace applications. EV31A (Elektron 21) and WE43C (Elektron 43) the two major types of magnesium rare earth alloys that were developed for high performance applications at elevated temperatures. Passivation and stress corrosion cracking behaviors of these magnesium rare earth alloys were investigated in this study. The effect of different heat treatment conditions of EV31A and WE43C on the environmental degradation behavior in alkaline solutions containing different chloride concentrations was investigated. In general, peak-aged condition show better passivation behavior in both alloys. The threshold chloride concentration for passivity break down in 0.1 M NaOH solution was 80 ppm for EV31A, and 200 ppm for WE43C in any heat treatment conditions. EV31A shows higher susceptibility to stress corrosion cracking than WE43C.

Acknowledgements

My research would have been impossible without the support of Royal Thai Navy. I also acknowledge the support of U.S. Nuclear Regulatory Commission through a faculty development grant NRC-HQ-84-15-G-0025. I would like to thank Dr. Krishnan S. Raja who is my major professor and advisor, Dr. Indrajit Charit, Dr. Batric Pesic, and the Department of Chemical and Materials Engineering staff. I would also like to thank Dr. Thomas Williams for supporting instrumental analysis.

Dedication

I dedicate this thesis to my family, my wife, my teachers, my colleagues, and ones who supported me but I do not mention.

Table of Contents

List of Figures

List of Tables

CHAPTER 1
Introduction

Magnesium has a long history back to 1755. Joseph Black, a Scottish chemist, discovered magnesium in the form of magnesia, but he was not able to extract this element. Until 1808, Sir Humphrey Davy, a British chemist and scientist, was able to extract magnesium, and he was named a person who discovered magnesium [1]. After that, many people tried to extract this metal in different methods. In 1941, the extraction of magnesium from dolomite by ferrosilicon at high temperature known as the Pigeon process was introduced and was used since then [2].

Magnesium is considered as a light metal because the density of magnesium is 1.738 g/cm^3 which is lower than iron (7.874 g/cm^3) [3], the famous structural metal. Magnesium is rarely used in a pure form; in contrast, it is a popular structural material alloying with other metals. In the past, aluminum alloys were widely used in the industries where required light weight and corrosion resistance; for example, automobile and aerospace industries. However, magnesium alloys become competitive alloys for those industries because magnesium alloys are lighter than aluminum alloys around 20% - 30%. Moreover, their mechanical properties and corrosion resistance were improved when alloyed with other metals.

Many elements are used to alloy with magnesium which can be widely divided into 2 types; zirconium-free and zirconium-containing magnesium alloys. Zirconium is used as a grain refiner; however, some elements such as aluminum and manganese are not compatible with zirconium and tend to suppress liquid solubility of zirconium. As a result, zirconium is a factor to classify magnesium alloys. For the zirconium-free types, aluminum is a major alloying element with minor elements such as manganese, silicon, and zinc. The examples of magnesium alloys in this category are aluminum-manganese such as AM20, AM50, AM60, aluminum-silicon such as AS21, AS41, and aluminum-zinc, the most widely used, such as AZ31, AZ81, AZ91. Zirconium-containing magnesium alloy has zirconium as a grain refiner to improve mechanical properties, castability, and corrosion resistance. Moreover, zirconium co-precipitates with impurities such as iron, nickel, and cobalt then they are removed during casting process. In addition to zirconium, many elements except aluminum and manganese are alloyed with magnesium; for example, zinc, silver, thorium, rare-earth elements, and yttrium.

The examples of systems consisted of these elements are magnesium-zinc-zirconium such as ZK51, ZK61, magnesium-rare earth-zinc-zirconium such as ZE41, EZ33, magnesium- silver such as QE22, and magnesium-yttrium such as WE54, WE43.

In addition to zirconium-free and zirconium-containing magnesium alloys, classifying in casting and wrought magnesium alloys is another way to categorize the alloys. However, casting magnesium alloys account for more than 80% compare to wrought magnesium alloys because magnesium has a hexagonal crystal structure. A hexagonal crystal structure has limited slip systems which leads to difficult deformation. The example of wrought magnesium alloys is AZ31, the most widely used found in sheet, plate, and extrusion forms. Another example is AZ81, found in extrusion and forging forms.

Because of high strength to weight ratio of magnesium alloys, many commercial alloys are introduced to the industries, especially automobile and aerospace applications. Magnesium-aluminum alloys are the most well-known and used wide spread because aluminum is the early element used to alloy with magnesium. Moreover, aluminum content can be varied to achieve desirable properties; for example, low aluminum content provides good ductility, 6 wt% of aluminum provides best mechanical properties [1], and high aluminum content provides high strength and good castability. In magnesium-aluminum alloy system, zinc may be added to improve tensile properties while manganese is added to improve corrosion resistance. Magnesium-zinc-copper alloys are developed to get ductility and stability at elevated temperature whereas tensile properties are similar to AZ91 which is in magnesium-aluminum system. Magnesium-zinc-zirconium alloys are another type of commercial magnesium alloys. However, microporosity is a problem of these alloys, so they are not widely used.

Rare earth elements improve strength at elevated temperature and creep resistance of magnesium alloys. The word “rare” does not mean that these elements are scarce; in contrast, they are abundant in nature. Some elements may be more available than silver. In fact, the word “rare” refer to the difficulty to extract from the minerals [4]. Rare earths are added in several systems. The first system is magnesium-rare earth-zinc-zirconium alloys. The microporosity problem in magnesium-zinc-zirconium is resolved when rare earths are introduced to improve fluidity of the alloys. Another system is magnesium-silver alloys. These alloys; for example, QE22, have high strength at high temperature up to 250 °C while creep resistance is up to 200 °C; however, the price of these alloys is high. Magnesium-yttrium alloys

are developed to increase creep properties and corrosion resistance. Compare to magnesium-silver alloys, magnesium-yttrium alloys have higher strength and better creep resistance.

Table 1.1 shows the comparison of mechanical properties of selected casting and wrought magnesium alloys.

Table 1.1 Mechanical properties at room temperature of selected magnesium alloys.

Mechanical property at room temperature	Magnesium alloy					
	Casting alloy			Wrought alloy		
	AZ91-T6	AM50	AS41	AZ31 sheet	WE54-T6 forging	WE43-T6 extrusion
Yield strength (MPa)	120	125	135	120	180	160
Ultimate tensile strength (MPa)	200	200	225	240	280	260
Elongation %	3	7	4.5	10	6	6

Even though magnesium alloys are competitive in aerospace, automobile, and other industries where require light weight, corrosion is a problem which is tried to overcome. Magnesium is a very active metal which has an electrode potential at -2.37 V_{SHE} whereas an electrode potential of aluminum is -1.66 V_{SHE}. In addition, the ratio between magnesium substrate and its passive film, known as Pilling-Bedworth ratio, is 0.81 while the Pilling-Bedworth ratio of aluminum is 1.38. This ratio shows the ability of passive film of metals. If the ratio is more than 1, it means that the surface of that metal is completely protected by its passive film. In contrast, if Pilling-Bedworth ratio is less than 1, a passive film does not completely protect a substrate metal. The passive film of magnesium and magnesium alloys consists of two layers; an outer layer which is $Mg(OH)_2$, and an inner layer which is MgO [5]. The passive film is stable in pH > 10.5, and it will be more protective in electrolytes containing F^- ion. However, the passive film is susceptible to Cl^-, SO_3^{2-}, SO_4^{2-} , NO_3^- , PO_4^{3-} , and CO_3^{2-}.

When magnesium alloy applications are in service, they are usually under stress and corrosive environment. Two of these factors as well as magnesium alloy itself are all three factors which cause stress corrosion cracking. The trend of using magnesium alloys in high performance applications such as aerospace and racing car is increasing. It means that the alloys encounter higher stress than normal applications. In addition, if stress corrosion cracking occurs with these applications, it will lead to serious catastrophe. Different types of magnesium alloys react with stress corrosion cracking in different levels; for example, zirconium-containing

magnesium alloys are less susceptible than zirconium-free magnesium alloys, and casting magnesium alloys are also less susceptible than wrought alloys [2].

In the late 1980s, magnesium alloy WE43 (Mg-Y-RE-Zr) was produced and developed since then to the latest series known as WE43C or Elektron 43. In the late 1990s, EV31A or Elektron 21 (Mg-Zn-Gd-Nd-Zr) was launched to the market [6]. Both alloys show good mechanical properties at elevated temperature, and good corrosion resistance. EV31A is a casting magnesium alloy which can be used at the temperature up to 200 °C. Additionally, it has good castability because of the absence of yttrium which is present in WE43 and Elektron 43. Moreover, the absence of yttrium can reduce the price of EV31A. WE43C is a wrought magnesium alloy which can be used at the temperature up to 250 °C. Mechanical properties of WE43C are better than of EV31A as shown in Table 1.2. Table 1.2 also shows mechanical properties of magnesium alloys AZ91 and AZ31, aluminum alloy 2024 in T6 condition, and low carbon steel 1020. The last two materials are used in aerospace applications.

While EV31A and WE43C become more widely used because they have good mechanical properties, and good corrosion resistance, the studies of their corrosion behavior in different corrosive environment are limited. Most of the experiments were conducted on very aggressive chloride concentration such as 3.5 wt% of NaCl (~21300 ppm Cl^-). At this concentration, it may be difficult to study passivation behavior of both EV31A and WE43C because passive film may not repassivate. In addition, it may be difficult to study pit initiation that causes pitting corrosion and may lead to stress corrosion cracking because pits may grow too fast to notice after they initiate. In terms of materials, most of the studies focused on magnesium-aluminum alloys which has been invented since 1930s [6], and WE43 which is the casting magnesium alloy.

Due to the fact that demand of using EV31A and WE43C increases, especially in the industries where require high performance and good corrosion resistant materials, but the understanding of pitting corrosion, and stress corrosion cracking is restricted, the project in this thesis was conducted to fulfill the knowledge of pitting corrosion, and stress corrosion cracking.

Table 1.2 Mechanical properties at room temperature of magnesium alloys EV31A, WE43C, AZ91, AZ31, aluminum alloy 2024-T6, and low carbon steel 1020.

Material	EV31A Casting	WE43C Wrought	AZ91 Casting	AZ31 Wrought	Al alloy 2024-T6 Wrought	Low carbon steel 1020 Wrought
Yield strength (MPa)	170	235	120	120	395	330
Ultimate tensile strength (MPa)	280	345	200	240	475	445
Elongation %	5	12	3	10	10	36

Aluminum alloy 2024, and low carbon steel 1020 are used in the same aerospace industry as EV31A, and WE43C.

This project focuses on two magnesium rare earth alloys which are EV31A and WE43C. These alloys were used to study passivation behavior and pitting protection in different heat treatment conditions, and in alkaline solution (0.1 M NaOH, pH 13) with different chloride concentration from 0 to 1000 ppm. Moreover, pit initiation was investigated. The study of EV31A is introduced in Chapter 2, and of WE43C is discussed in Chapter 3. To understand the passivation of these magnesium rare earth alloys more, EV31A and WE43C were passivated in different concentration of NaOH which were 0.01 M, 0.1 M, and 1 M as discussed in Chapter 4. Chapter 5 is discussed stress corrosion cracking of the alloys. The U-bend tests were applied to the specimens because they were economically, and many experiments could be run at the same time. The corrosive environment was simulated in 80, 100, 200 ppm chloride concentrations.

References

[1] Friedrich, H. E., & Mordike, B. L. (Eds.). (2006). *Magnesium technology: metallurgy, design data, applications*. Verlag Berlin Heidelberg, Germany: Springer.

[2] Polmear, I. (2006). *Light alloys from traditional alloys to nanocrystals* (4th ed.). Burlington, MA: Butterworth-Heinemann.

[3] American Society for Metals. (1986). *Metals Handbook Desk Edition*. Metals Park, OH: American Society for Metals.

[4] *Introduction to the Rare Earths* [PDF document]. Retrieved from https://www.liverpool.ac.uk/~sdb/Research/Chapter1.pdf

[5] Chu, P. W., & Marquis, E.A. (2015) Linking Microstructure of a Heat-Treated WE43 Mg Alloy with its Corrosion Behavior. *Corrosion Science*, 101, 94 - 104.

[6] Gwynne, B., & Lyon, P. (2007). *Magnesium alloys in aerospace applications, past concerns, current solutions* [PDF document]. Retrieved from https://www.fire.tc.faa.gov/2007conference/files/Materials_Fire_Safety/WedAM/GwynneMagnesium/GwynneMagnesiumPres.pdf

CHAPTER 2

Threshold Chloride Concentration for Passivity Breakdown of Mg-Zn-Gd-Nd-Zr Alloy (EV31A) in Basic Solution

Jakraphan Ninlachart, Krishnan S. Raja
Chemical and Materials Engineering, University of Idaho, Moscow, ID 83844-1021, USA

Threshold Chloride Concentration for Passivity Breakdown of Mg-Zn-Gd-Nd-Zr Alloy (EV31A) in Basic Solution. *Acta Metallurgica Sinica (English Letters)*, 30 (4) (2017) 352 – 366.

Abstract

Mg-Zn-Gd-Nd-Zr alloy (EV31A) is a heat-treatable magnesium (Mg) cast alloy that can be used up to 200 °C for automobile and aerospace applications. This alloy has excellent mechanical properties (ultimate tensile strength: 280 MPa at room temperature, and ~230 MPa at 200 °C) and improved corrosion resistance. Electrochemical corrosion studies were conducted on this alloy under different heat treatment conditions in 0.1 M NaOH solution with the addition of 0 – 1000 ppm of chloride. The alloy showed excellent passivity in the 0.1 M NaOH solution. The passive potential range typically extended to more than 1.2 $V_{Ag/AgCl}$. The transpassive potential was observed to be dependent on heat treatment condition of the alloy. More than 80 ppm of chloride was required to induce passivity breakdown in any heat treatment condition. Peak aging at 200 °C for 16 h imparted better resistance for localized corrosion than other heat-treated conditions. The alloy in the as-received condition showed the highest passivation kinetics due to its smaller grain size that possibly increased the diffusion of reactive elements to form protective oxide. The passive film of the EV31A alloy showed *n*-type semiconductivity with a charge carrier density of $\sim 2 \times 10^{21}$ cm^{-3} with no chloride addition. The charge carrier density increased with chloride addition in the electrolyte which could be correlated with the susceptibility to localized corrosion.

Keywords: Magnesium alloy; Corrosion; Passivation; Chloride

2.1 Introduction

Magnesium-based alloys have excellent strength-to-weight ratio, because of which they find applications in automobile, aerospace and biomedical devices and components. However, Mg alloys are limited by poor formability, texturing effect and creep resistance. Alloying with rare earth elements helps overcome some of these limitations. Microalloying with RE has been observed to improve the ductility and weaken the texturing effect [1, 2]. Zr is added as alloying element in Al-free Mg alloys to mitigate the detrimental behavior of impurities such as Fe, Ni and Co which otherwise will form cathodic intermetallic compounds and increase the corrosion attack. Zr also improves the mechanical properties by refining the grains [3, 4]. Alloying with RE also improves the high-temperature tensile strength and creep resistance [5]. Alloy EV31A (also known as Elektron 21 from Magnesium Elektron N.A. Inc.) was recently introduced as an alternate to the widely known WE43 alloy owing to its low cost, easy castability due to the absence of yttrium, and enhanced corrosion resistance [6]. The corrosion rate of the EV31A alloy has been reported to be 10 – 30 m/y based on the ASTM B117 salt spray test [7].

EV31A nominally has (in wt%) 0.2% - 0.5% Zn, 2.6% - 3.1% Nd, 1.0% - 1.7% Gd and saturated amount of Zr as alloying additions. Zr has a calculated solubility of about 0.76 at.% in liquid Mg and about 0.2 at.% at 400 °C [8]. The maximum solid solubility of Zn at eutectic temperature is 2.4 at.% and decreases to about 0.1 at.% at room temperature. The identified secondary phases in the Mg-Zn-Zr system are MgZn, Mg_7Zn_3, Zn_2Zr_3, ZnZr, $(Zn, Mg)_2Zr$ and $Zn_2(Mg, Zr)$ [9]. Out of these, Zn_2Zr_3 phase is most likely present in the EV31A alloy [10].

The terminal solid solution of Nd in Mg is considered to be 0.7 at.% at its eutectic temperature (822 K), and the secondary phases that are in equilibrium with the solid solution are $Mg_{41}Nd_5$, Mg_3Nd, Mg_2Nd, MgNd and $Mg_{12}Nd$ [11]. The Mg_2Nd phase is considered to be metastable since only the quenched sample contained this phase and not the annealed ones [12]. The terminal solid solubility of Gd in Mg is reported to be 23.49 wt% at 548 °C (eutectic temperature), and the secondary phases of the Mg-Gd binary system are Mg_5Gd, Mg_3Gd, Mg_2Gd and MgGd. Addition of Nd and Gd together helps improve the age hardening response as the solubility of Gd is reduced with the incorporation of Nd [13]. Zinc is also considered to enhance the age hardening response and creep strength of Mg-Gd alloys [14]. In a Mg-Nd-Gd system, addition of Zn can delay the overaging process at 250 °C and increase the hardness [13].

Addition of Zn to Mg-Nd-Gd-Zr system was observed to increase the corrosion resistance when the Zn content was around 0.2% exfoliation-type corrosion attack observed and with 0.75% Zn the corrosion occurred by preferential dissolution of zinc zirconide-type coarse precipitates [13]. Good corrosion resistance was observed when the Zn content was in the range of 0.2% - 0.55% and Gd was <1.75%.

The EV31A alloy can be solution-heat-treated at 525 °C for 8 h followed by quenching in warm water at 60 – 80 °C. After quenching, the alloy can be artificially aged in the temperature range of 150 – 300 °C for different time periods to achieve desired results. The precipitation reactions occurring during the aging process are reported to follow the sequence of α-Mg $\rightarrow \beta'' \rightarrow \beta' \rightarrow \beta$ (Mg_3RE) $\rightarrow Mg_{41}RE_5$ [15]. The β'' phase has a platelet morphology of 8 nm long and 2 nm thick coherent with the matrix under peak hardening condition [16]. The β' phase is metastable and semicoherent with matrix with spherical morphology. The lattice structure of the β' phase is body-centered orthogonal. The stable β phase (Mg_3RE) has an FCC structure [16].

The composition of β'' in EV31A has not been clearly reported due to its nanoscale size and limitations in imaging of Mg under ion field [17]. Using 3-D atom probe, Nie and coworkers [17] reported that the composition of ordered G.P. zone precipitates in a Mg-RE-Zn-Zr alloy was 3.2 at.% Nd, 1 at.% Ce and 1.2 at.% Zn. The composition of β' phase of Mg-Nd-Gd alloys was reported to follow the stoichiometry of Mg_6Nd [18]. Increasing the Nd:Zn ratio increased the Nd content of the β' phase precipitates. When the Nd:Zn ratio was 2:1, the precipitates were of Mg_5Nd type and when Nd:Zn ratio was 1:1, the β' phase was of Mg_9Nd type. This composition is different from that reported by Kielbus et al. [15].

Most of the corrosion studies of Mg-RE alloys have been carried out in chloride-containing solutions that are mimicking either marine or biological environment [19, 20]. Scully and coworkers compiled open-circuit potentials (OCPs) or corrosion potentials (E_{corr}) of different Mg alloys exposed to different concentrations of NaCl solutions (0.01 – 5 M) in near neutral pH conditions and observed that Mg-RE alloys showed the most negative corrosion potentials or similar to the potentials of pure Mg, when the total RE content was < 2.75 wt% [21]. Increasing the chloride concentration shifts the OCP to a more cathodic potential. The alloy WE43 shows a more negative OCP (between – 1.75 and – 1.85 V_{SCE}) than that of pure

Mg (– 1.6 to – 1.72 V_{SCE}) in the neutral chloride solutions. The Mg_3Nd intermetallic has a relatively less cathodic OCP (- 1.55 V_{SCE}) in 0.1 M NaCl [22]. Increasing the pH increases the OCP. The more active corrosion potentials observed in Mg-RE alloys than those of pure Mg are counter-institutive to the well-documented "reactive element effect" of rare earth elements that enhances the protective characteristics of the surface oxide [23]. Most of the available reports on corrosion of Mg-RE alloys pertain to cast structures. Recently Birbilis and coworkers investigated the influence of low levels of Zn, Gd, and Zr in Mg for wrought applications [24]. They observed that addition of Zr and Gd generally resulted in enhanced kinetics of cathodic reaction in Mg-0.4Zn-0.8Ca alloy, and reduced the anodic reaction kinetics. Overall, the investigated Mg alloys showed higher corrosion rates than pure Mg, because of higher cathodic kinetics, and ennobled corrosion potentials.

Passivation of Mg alloys has been observed in high alkaline solutions. Ismail and Virtanen [25] observed large fluctuations in OCP (between – 1.6 and – 0.55 V_{SCE}) of AZ31 alloy in 0.5 M KOH. The potential shifts were cyclic in nature and were attributed to the formation of passive film and subsequent dissolution. Similar type of OCP fluctuations was observed in pure Mg exposed to 1 M NaOH solution by Taheri and Kish [26]. These authors proposed that hydration of the initially formed crystalline MgO layer caused stress induced localized breakdown of the surface film on Mg. During the film formation process, the OCP shifted to less negative values. The breakdown of the film caused the OCP to move back to its original values, and subsequent repair of the film caused ennoblement of the OCP. Li et al. [27] investigated passivation behavior of AZ31B die cast Mg-Al-Zn-Mn alloy in alkaline (NaOH) solutions with pH 10 – 14. These authors found that the thickness of the surface layer was different on different phases of the specimen when exposed to pH ≥ 13 solutions, whereas uniform thickness of the film was noticed on all phases in the entire surface when tested in pH 12 solution. The reduction in pH to 11 caused galvanic corrosion between different phases.

Song and Unocic [28] investigated anodic surface films formed on Mg in $Mg(OH)_2$-saturated solution. They observed intensive hydrogen evolution even at the potentials more positive than the equilibrium hydrogen evolution potential due to formation of univalent Mg ions and subsequent reaction with water. The surface film became more porous due to intensified anodic H_2 evolution. Cao et al. [29] critically reviewed the literature on the passivation of Mg alloys and recommended future research directions. The review discussed

different scenarios of rendering passivity in Mg, such as kinetically induced passivation by alloying with Cr, Ti, Al, Ni, Zr, etc., passivation in special environments, design of heat treatments for passivation and microstructural modifications by processing conditions. Recently, Song et al. [30] prepared Mg-Ti alloy thin films by magnetron sputtering and studied their passivation behavior in 0.1 wt% NaCl solution saturated with $Mg(OH)_2$. They observed that about 51 at.% of Ti was required to induce passivity on the Mg-Ti alloys. At a lower addition of Ti, the passivation was not effective.

Yao et al. [31] investigated the passivation behavior of Mg-Y alloys in alkaline chloride solutions and observed incorporation of Y_2O_3 in the passive film which enhanced passivity. Pinto et al. [32, 33] studied passive behavior of Mg-Zr-RE alloys, such as ZK31, EZ33 and WE54, in alkaline media with and without chloride addition and in borate buffer solution. The passive film in alkaline solution consisted of an outer $Mg(OH)_2$-type layer and an inner MgO layer without the presence of alloying elements. On the other hand, in borate buffer solution (pH 9.2), an amorphous yttrium oxide/hydroxide thick layer was observed that imparted higher corrosion resistance to the WE54 alloy. Alloying with RE was observed to improve the corrosion resistance when the RE was in the solution. When RE segregated along grain boundaries as a secondary phase, microgalvanic effect was noticed.

The foregoing discussion on the corrosion literature of Mg-RE alloys mostly pertains to cast structures in the neutral chloride solutions. The effect of wrought microstructures (that will have much smaller and uniformly distributed secondary phase particles) on the corrosion behavior has not been investigated in detail. The typically used 0.1 M NaCl that mimicks the marine atmosphere may be too aggressive to understand the effect of microstructures on the corrosion behavior of Mg-RE alloys. Furthermore, the passivation behavior of EV31A has not been investigated in detail to the best of the authors' knowledge. In this study, the electrochemical passivation behavior of EV31A under different heat-treated conditions was evaluated to understand the effect of aging microstructure and chloride concentration in 0.1 M NaOH solution (pH 13.5) on the passivity breakdown at room temperature. The strong alkaline solution was employed because Mg can form a stable surface film at pH > 11 according to the potential pH equilibrium diagram of Mg-H_2O [34]. Therefore, this work is fundamental in nature.

2.2 Experimental

The material used in this investigation was Mg-Zn-Gd-Nd-Zr alloy (EV31A), a 16-mm-thick plate provided by Magnesium Elektron N.A. Inc. It was cut into 1.5 cm × 2.5 cm × 0.3 cm coupons. The as-received coupons were solution heat-treated at 525 °C for 8 h and quenched in water. Aging treatments were carried out at 200 °C for 16 and 100 h and then cooled in air. The specimens were ground with SiC paper up to 600 grit and cleaned with methanol and dried in air just before corrosion test. For microstructural observation and microhardness test, the specimens were ground with SiC paper up to 1200 grit and 1-micron diamond suspension and then cleaned with methanol and dried. Etching was carried out to reveal the grain boundaries of tested specimens with glycol etchant containing 10 ml HNO_3, 24 ml water, 75 ml ethylene glycol. The optical microscopy on the etched specimens was conducted using an OLYMPUS PMG3 optical microscope. Vickers hardness was measured using a microhardness tester (Leco, LM100 from Leco) and a load of 10 g. The reported values are average of at least ten readings in each specimen.

The electrochemical measurements were conducted by using 3-electrode flat PTFE electrochemical cell with a Pt wire spiral (2.5 cm^2 surface area) as counter electrode and KCl-saturated Ag/AgCl (199 mV vs SHE) as reference electrode and a potentiostat (VersaSTAT MC, and VersaStudio software version 2.42.3 from Princeton Applied Research). The exposed surface area of specimen was 1 cm^2. The electrolytes were 0.1 M NaOH (pH 13.5) with different chloride concentrations (0, 80, 100, 200, 500 and 1000 ppm Cl^- in the form of NaCl). The cyclic polarization was performed at 0 – 2.5 V vs OCP at a scan rate of 1 mV/s. It should be noted that the apex potential is much higher than the equilibrium potential of oxygen evolution (water stability limit), and may not be very relevant to practical service conditions. However, such a high potential was found to be necessary for evaluating the passivity breakdown under different heat treatment conditions. No correction was carried out to account for the iR drop in the system, and thus, the effect of solution conductivity was unknown. The potential scans were reversed at 2.5 $V_{Ag/AgCl}$, or when the transpassive current density was reached 1 mA/cm^2. The potentiostatic tests were conducted for 3600 s at the middle of the passivation range. Electrochemical impedance spectroscopy (EIS) measurements were carried out under potentiostatic condition by applying the passivating potential and superimposing an AC signal of 10 mV, and scanning the frequency from 100 kHz down to 10 mHz. Mott-

Schottky measurements were carried out at a frequency of 316 Hz by scanning the potential of the specimens from the middle of the passivation range to OCP at 50 mV steps.

2.3 Results and Discussion

2.3.1 Microstructural Characterization

Figure 2.1(a) – (d) illustrates the optical microstructure of the specimens in different heat treatment conditions. Figure 2.1(a) shows the as-received microstructure of the T-S (transverse-short transverse) orientation. Banding and texturing across the thickness of the plate with fine grain size can be observed. The X-ray diffraction (XRD) pattern of the as-received specimen has several minor peaks associated with secondary phases such as $Mg_{12}Nd$, Mg_3RE and $Mg_{41}Nd_5$, as shown in Fig. 2.2(a). Solution treatment considerably reduced the banding and texturing and resulted in grain growth with an average grain size of about 30 μm. The presence of intermetallic phases within grains and along grain boundaries can be observed as shown in Fig. 2.1(b). The undissolved secondary phase particles have been identified as $Mg_{12}Nd$ by other investigators [35]. The XRD results shown in Fig. 2.2(a) support the presence of Mg_xRE phase in the solution-treated alloy. The microstructure of the peak-aged specimen is illustrated in Fig. 2.1(c).

Since the peak aging can result in precipitation of nanoscale β'' phase that is coherent with the matrix, the optical microstructure of the peak-aged sample cannot be significantly different from that of the solution heat-treated (ST) specimen. The XRD pattern of the peak-aged (PA) specimen is more or less similar to that of the ST. Figure 2.1(d) shows the microstructure of the overaged (OA) specimen. Cellular-type precipitates nucleate at the grain boundaries. Some grains that were etched dark are considered to have a high volume fraction of the cellular-type β phase (Mg_3RE) precipitation within the grains. The dark-etched bands running across grains suggest preferential precipitation of β phase on these highly strained locations that contained a high density of dislocations. The XRD pattern indicates the presence of Mg_3RE-type β phase in the OA sample.

Figure 2.2(b) illustrates the Vickers hardness of the specimens. Almost similar hardness was observed for the specimens in the as-received (AR) and solution heat-treated (ST) conditions. Heating at 200 °C for 16 h (T6 condition) is considered to be peak aging as the hardness reached the highest value 84 VHN (kgf/mm^2). Aging at 200 °C for 100 h resulted in

hardness of 80 VHN. The peak-aging and overaging conditions are categorized based on their microstructures and hardness values. Similar results have been reported by other investigators [15].

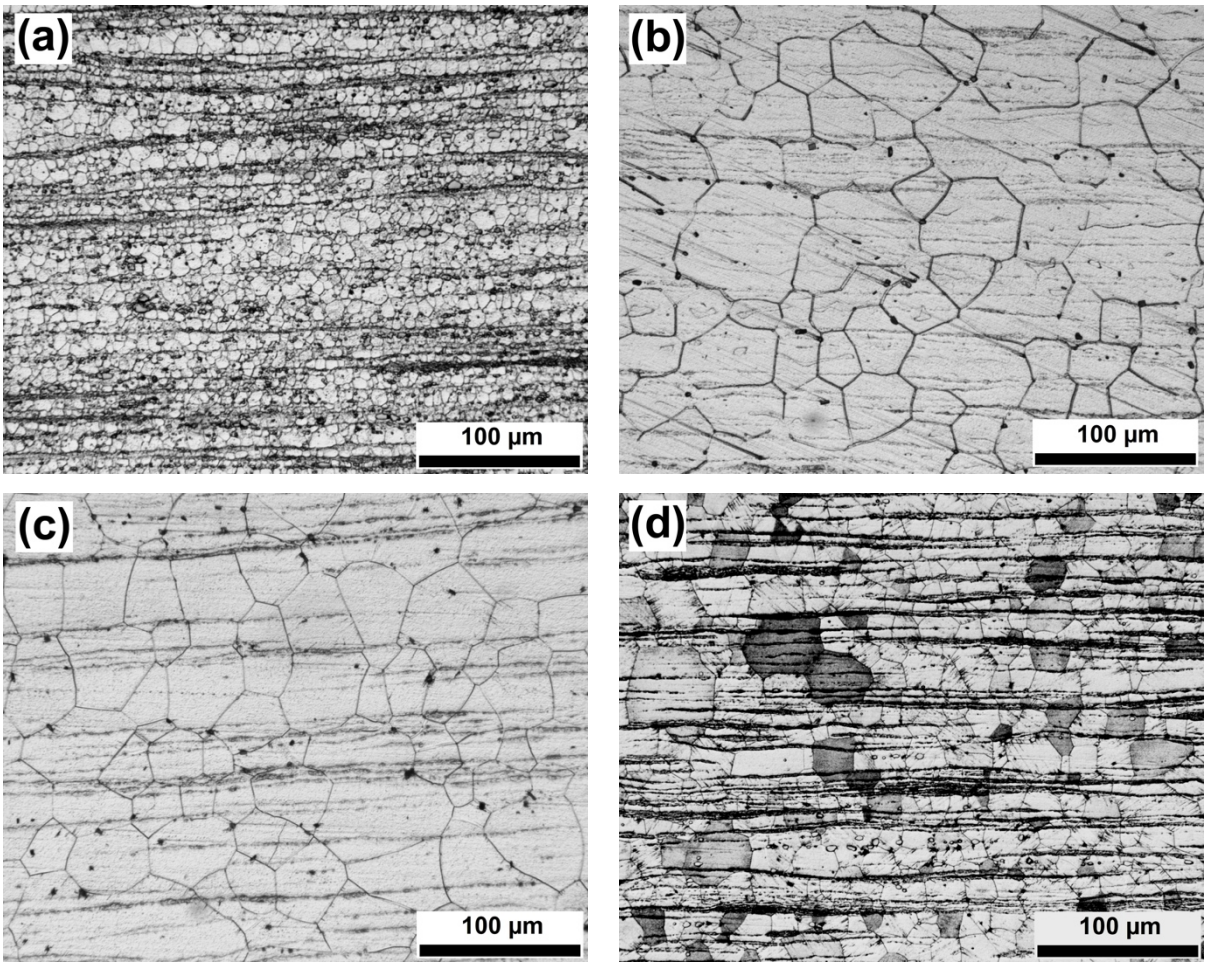

Fig. 2.1 Optical microstructures of EV31A in different heat treatment conditions: **(a)** as-received, **(b)** solution heat-treated, **(c)** peak-aged (200 °C, 16 h), **(d)** overaged (200 °C, 100 h).

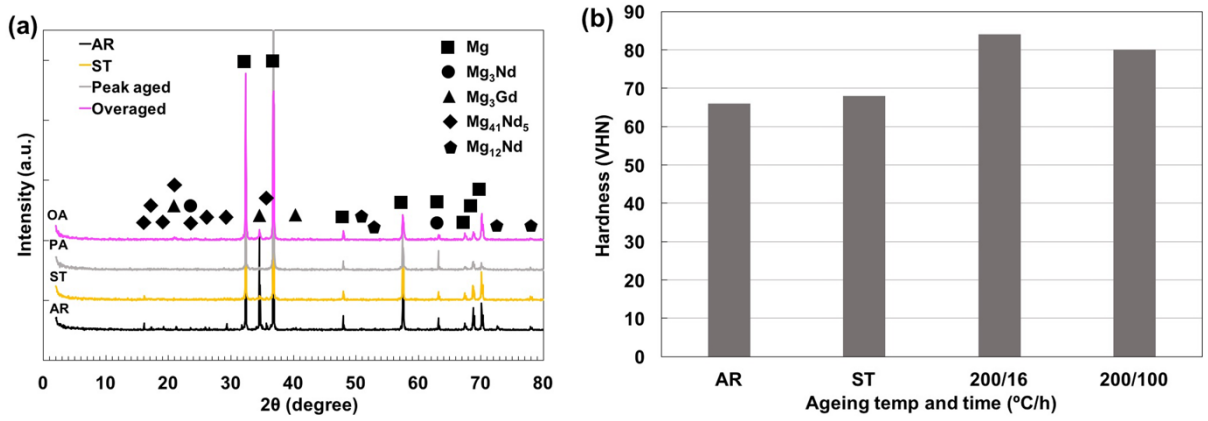

Fig. 2.2 (a) XRD patterns of EV31A in different heat treatment conditions, **(b)** Vickers hardness of EV31A in different heat treatment conditions. AR as-received, ST solution heat-treated, 200/16 peak-aged (PA) at 200 °C for 16 h, 200/100 overaged (OA) at 200 °C for 100 h.

2.3.2 Cyclic Polarization Behavior

Figure 2.3(a) illustrates the cyclic polarization plots of the EV31A specimens in 0.1 M NaOH solution without chloride addition. The ST specimen showed the most active corrosion potential, and the AR specimen showed the least active corrosion potential. The variations in the OCP could be due to the differences in the microstructures that show different cathodic and anodic reaction kinetics. Based on the mixed potential theory [36], more active OCP values can be anticipated when the exchange current density for cathodic reaction is lower or the cathodic Tafel slope is steeper for a given anodic reaction kinetics. Alternately, for a given cathodic reaction kinetics, lower corrosion potential will be observed when the exchange current density for the anodic reaction is higher or the Tafel slope of the anodic reaction is shallower. Since better passivation behavior is expected when the RE and other alloying elements are in solid solution, steeper Tafel slope of anodic reaction is expected. Chu and Marquis reported steeper cathodic Tafel slope and lower exchange current density for the solution-treated WE43 alloy than that of peak-aged condition [37]. Based on the foregoing discussion, it should be noted that lower activity for the cathodic reaction could be the reason for the more negative OCP of the solution-treated specimens. Both PA and OA specimens showed almost similar OCP values between the OCPs of the ST and AR specimens. It is interesting to note that ST, PA and OA specimens showed almost similar passive current densities in the range of 2.67 – 4.1 $\mu A/cm^2$.

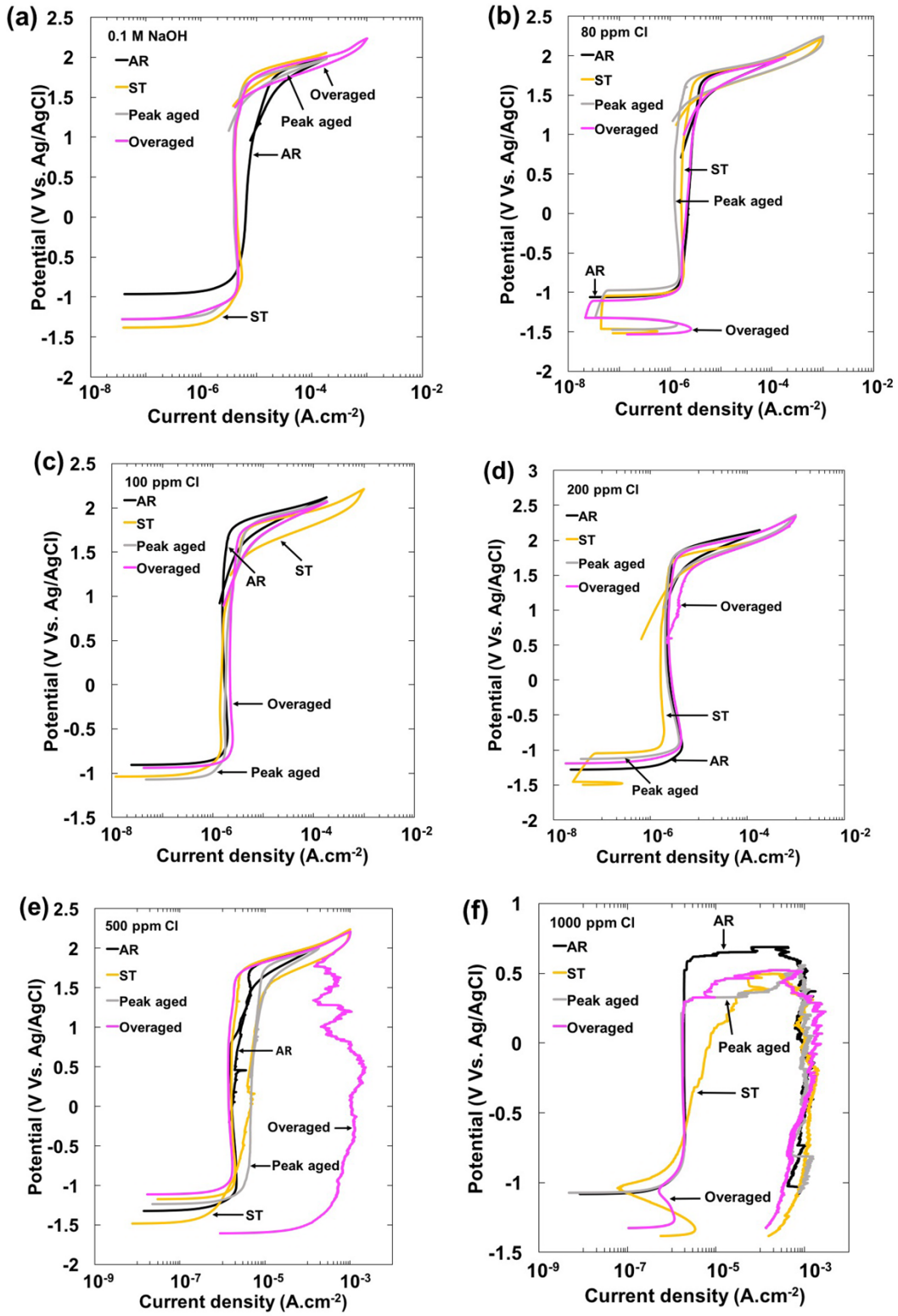

Fig. 2.3 Cyclic polarization results of EV31A specimens in different heat-treated conditions in 0.1 M NaOH with different chloride additions: **(a)** 0 ppm Cl^-, **(b)** 80 ppm Cl^-, **(c)** 100 ppm Cl^-, **(d)** 200 ppm Cl^-, **(e)** 500 ppm Cl^-, **(f)** 1000 ppm Cl^-.

The passive current density was the lowest for the ST condition at 2.67 $\mu A/cm^2$, and it increased for the aging condition, while the OA specimen showed 4.11 $\mu A/cm^2$. The AR specimen showed an even higher current density (7 – 10 $\mu A/cm^2$) which increased with anodic polarization indicating possible presence of a highly disordered or defective passivation layer. Passivation of the specimens was observed between -1 $V_{Ag/AgCl}$ and +1.6 $V_{Ag/AgCl}$. The transpassive potentials were not significantly different among the different heat treatment conditions. When the potential scan was reversed after reaching the transpassive condition, a small hysteresis was observed as the reverse scan did not exactly trace the forward current profile. The cross-over potential of the reverse scan on the forward scan curve is considered generally as pitting protection potential. However, in the 0.1 M NaOH without any chloride addition no pitting is expected to occur. All the other specimens in chloride-containing solutions showed hysteresis and breakdown of passivity. In stainless alloys, such as Ni-Cr-Mo alloys, the transpassive current could be associated with oxygen evolution reaction as given in reaction (1) and not the metal dissolution [38].

$$4OH^- \rightarrow O_2 + 2H_2O + 4e^-. \quad (1)$$

In addition to the oxygen evolution, the other possible transpassive reactions of Mg in alkaline solution without chloride are given as follows:

$$2Mg + 8OH^- \rightarrow 2MgO + O_2 + 4H_2O + 8e^-, \quad (2a)$$

$$MgO + H_2O \rightarrow Mg(OH)_2, \quad (2b)$$

$$Nd(OH)_3 + OH^- \rightarrow NdO_2 + 2H_2O + 2e^-, \quad (3a)$$

$$2NdO_2 + 3H_2O \rightarrow 2Nd(OH)_3 + \frac{1}{2} O_2, \quad (3b)$$

$$Zn + 4OH^- \rightarrow ZnO_2^{2-} + 2H_2O + 2e^-, \quad (4)$$

$$Zr + 5OH^- \rightarrow HZrO_3^- + 2H_2O + 4e^-. \quad (5)$$

It is documented that the passivity of Mg-RE alloys is attributed to the formation of MgO and $Mg(OH)_2$ layers on the surface with incorporation of RE oxide/hydroxide [32]. No surface analysis of the passive film was carried out in this work to support the incorporation of rare earth oxide in the surface layer. It is simply a hypothesis based on the data presented in [32]. At the transpassive conditions (when the polarization potential is sufficiently high for oxygen evolution), chemical dissolution of the cations from the passive layer could occur aided

by oxygen evolution reaction. This dissolution weakens the passive layer, and a series of reactions given in (2a) – (5) are postulated to take place.

The reactions (2a) and (2b) are the regular passive film formation reactions, and those also occur in the transpassive condition at the sites disrupted by the oxygen evolution reaction. Reaction (3a) is oxidation of Nd^{3+} to Nd^{4+} which is not stable in aqueous electrolyte and therefore can revert back to Nd^{3+} by evolving oxygen [39]. The oxidation reactions of the alloying elements proposed through reactions (2a) – (5) in combination with oxygen evolution reaction could result in hysteresis. During the reverse scan, less potential was required to induce the same current as compared to the forward scan. This could be due to decrease in resistivity of the passive layer. The resistivity is influenced by the charge carrier densities of the passive layer. Introduction of Schottky- or Frenkel-type defects in the passive layer affects the electronic conductivity during polarization and therefore causes hysteresis in the cyclic polarization. Alternately, the increase in surface area due to transpassive dissolution of Mg and other alloying elements could also be attributed to the minor hysteresis observed in the cyclic polarization plot.

Table 2.1 summarizes the cyclic polarization results in 0.1 M NaOH. The cross-over potentials of ST, PA and OA specimens are 1.52, 1.31 and 1.47 $V_{Ag/AgCl}$, respectively. Below the cross-over potential, the passive current density of the reverse scan is much lower than that of the forward scan. The AR specimen shows a cross-over potential of 1.07 $V_{Ag/AgCl}$. This result indicates that anodic polarization in the transpassive range introduced a high density of defects in the passive layer of the as-received specimen, and it took a long time to recover or anneal out the defects during the reverse scan. In other words, the passive layer of the AR condition was less stable perhaps due to the banded and the textured microstructures of the substrate.

Table 2.1 Cyclic polarization results of EV31A specimens in different heat-treated conditions in 0.1 M NaOH.

Sample	OCP (V vs Ag/AgCl)	$E_{Transpassive}$ (V vs Ag/AgCl)	$E_{Cross\text{-}over}$ (V vs Ag/AgCl)	Passive current density ($\mu A/cm^2$)
AR	-1.03	1.67	1.07	7.00
ST	-1.50	1.73	1.52	2.67
Peak-aged	-1.20	1.52	1.31	3.90
Overaged	-1.21	1.58	1.47	4.11

Figure 2.3(b) shows the cyclic polarization of the specimens in 80 ppm Cl^- containing 0.1 M NaOH solution. The AR specimen has a higher OCP than other specimens. The polarization curves of PA and OA specimens indicate two different anodic processes in the potential window from -1.6 to -0.8 $V_{Ag/AgCl}$.

Polarization curves with an inflection point or a two-step process have been reported for ZK31 alloy [33] and Mg [40]. Natta attributed the current peak at the lower potential to the formation of univalent Mg

$$Mg \rightarrow Mg^+ + e^- \qquad E^0 = -2.28\ V_{Ag/AgCl}\ , \qquad (6)$$

and the second oxidation shoulder at the slightly higher potential to the reaction of forming divalent Mg ions:

$$Mg \rightarrow Mg^{2+} + 2e^- \qquad E^0 = -1.36\ V_{Ag/AgCl}. \qquad (7)$$

It should be noted that no direct evidence of the formation of Mg^+ has been reported although the involvement of Mg^+ in the anodic dissolution in film broken areas has successfully explained numerous electrochemical corrosion phenomena of Mg alloys. In case of the AR specimen, the oxidation shoulder of formation of monovalent Mg was not revealed because the OCP was more positive than the Flade potential. Addition of 80 ppm Cl^- did not affect the passive current density and the transpassive potentials as summarized in Table 2.2. The pitting protection potentials recorded for the specimens in 80 ppm Cl^- were similar to their counterparts in the 0.1 M NaOH solution without chloride addition. These results indicated that the EV31A alloy can be safely used in 80 ppm Cl^--containing environment of pH 13. It should be noted that the high pH environment may not represent a real service condition. However such a study presented here helps fundamentally understand the passivity nature of Mg-RE alloys.

Table 2.2 Cyclic polarization results of EV31A specimens in different heat-treated conditions in 80 ppm Cl^- solution.

Sample	OCP (V vs Ag/AgCl)	$E_{Transpassive}$ (V vs Ag/AgCl)	$E_{Cross\text{-}over}$ (V vs Ag/AgCl)	Passive current density ($\mu A/cm^2$)
AR	-1.66	1.64	1.27	2.50
ST	-1.57	1.61	1.37	1.66
Peak-aged	-1.55	1.58	1.29	1.21
Overaged	-1.57	1.62	1.38	2.20

Figure 2.3(c) – (f) shows the cyclic polarization results in 0.1 M NaOH with the addition of 100, 200, 500 and 1000 ppm chloride. Increasing the chloride additions did not increase the

passive current density. The maximum passive current density recorded was 4.75 $\mu A/cm^2$ for the peak-aged specimen in 500 ppm Cl^-. In other test conditions and specimens, the passive current densities were in the range of 1.5 – 2.8 $\mu A/cm^2$. However, the pitting protection potential was influenced by the chloride content and the aging condition.

As discussed earlier, addition of 80 ppm Cl^- did not affect the stability of the passivity of the EV31A specimens. Increasing the Cl^- level to 100 ppm shifted the pitting protection potentials to 1.06, 1.37, 1.16 and 1.2 $V_{Ag/AgCl}$ for the AR, ST, PA and OA specimens, respectively. Increasing Cl^- concentration to 200 ppm did not affect the stability of the passive films of AR, ST and PA specimens significantly as observed in Fig. 2.3(d). However, the pitting protection potential of OA specimen decreased to 0.64 $V_{Ag/AgCl}$ upon the addition of 200 ppm Cl^-. Further increasing the chloride level to 500 ppm decreased the pitting protection potential of the AR, ST and PA specimens to -0.02, -0.87 and 0.59, respectively. The OA specimen did not repassivate during the reverse scan as observed in Fig. 2.3(e). Increasing the chloride concentration to 1000 ppm caused complete breakdown of the passive film of the specimens during the reverse scan and considerably decreased the transpassive potentials as compared to that of 500 ppm Cl^-. The transpassive potentials in 1000 ppm Cl^- solution were 0.48, -0.37, 0.18 and 0.22 $V_{Ag/AgCl}$ for the AR, ST, PA and OA specimens, respectively.

Figure 2.4(a) – (d) shows the cathodic polarization plots of EV31A alloy in different heat treatment conditions in 0.1 M NaOH solution with different chloride (NaCl) additions. Table 2.3 summarizes the cathodic polarization results. The cathodic reaction is considered to be hydrogen evolution reaction. The equilibrium potential for hydrogen evolution in pH 13.5 solution is about -1.0 $V_{Ag/AgCl}$. Even though there is not a clear dependence of the hydrogen evolution reaction (HER) kinetics on different heat treatments and different chloride concentrations from Table 2.3, the following observations can be summarized. (1) The as-received specimens show lower cathodic reaction kinetics than the other heat treatment conditions in low chloride concentrations. (2) The peak-aged specimens show slower cathodic reaction kinetics in 0 and 100 ppm chloride additions. (3) The Tafel slopes vary from 0.13 to 0.21 V/decade in general, which indicates that the HER was controlled by Volmer reaction: $M + H_2O + e^- \rightarrow MH + OH^-$ [41], followed by Tafel reaction: $MH + MH \rightarrow 2M + H_2\uparrow$, where M denotes metal active site for hydrogen adsorption. The polarization plots indicate that the exchange current density for hydrogen evolution is very low in the range of pA/cm^2 to nA/cm^2.

Song et al. [42] reported an exchange current density in the range of 5 – 7 pA/cm^2 for Mg in pH 13 Na_2SO_4 solution and a Tafel slope of 260 mV/decade. On the other hand, Frankel et al. [43] reported a very high Tafel slope of 0.75 V/decade and an exchange current density of 4 μA/cm^2 for Mg in neutral NaCl solution. The high exchange current density of Mg in chloride solution could possibly be attributed to enhanced surface area due to dissolution of Mg. In high pH solutions, not only passivation is induced on Mg alloys but also the rate of cathodic hydrogen evolution reaction is lower. Birbilis and coworkers [44] reported enhanced hydrogen evolution on $Mg(OH)_2$-covered Mg surfaces. The rate of HER on the $Mg(OH)_2$ was 4 – 6 times faster than that of the pristine Mg surface at -1.9 V_{SCE} in pH 11 solution. The higher activity of HER on the hydroxide-covered surface was attributed to the enhanced self-dissociation of the water. On the other hand, Song and Unocic [28] argued that the presence of an oxide/hydroxide film which is electronically insulating would slow down the HER kinetics due to increased electrical resistivity of the surface films as compared to the bare Mg surface. In the absence of any surface analysis data, it is not possible to discuss how the surface film of the EV31A alloy affected the HER kinetics.

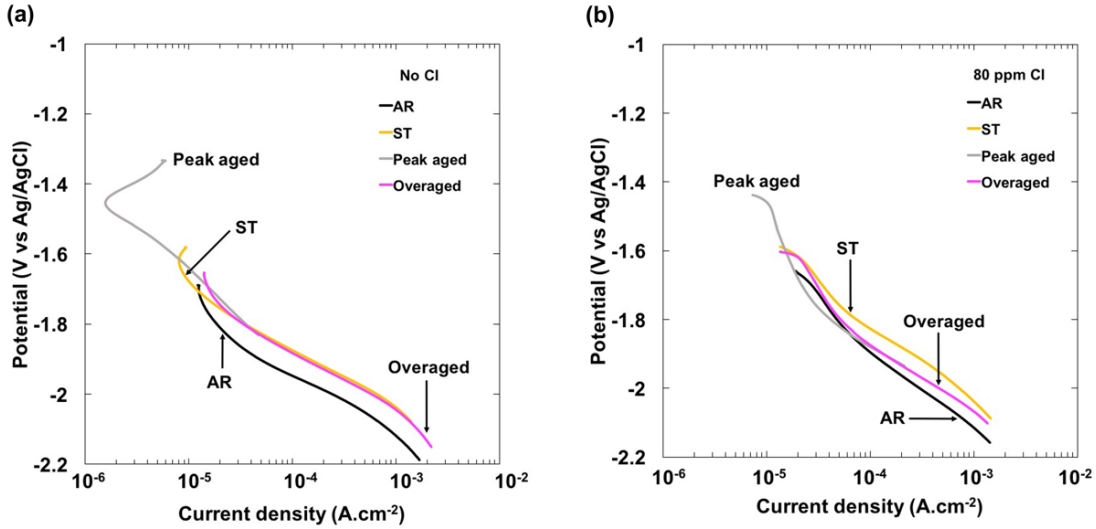

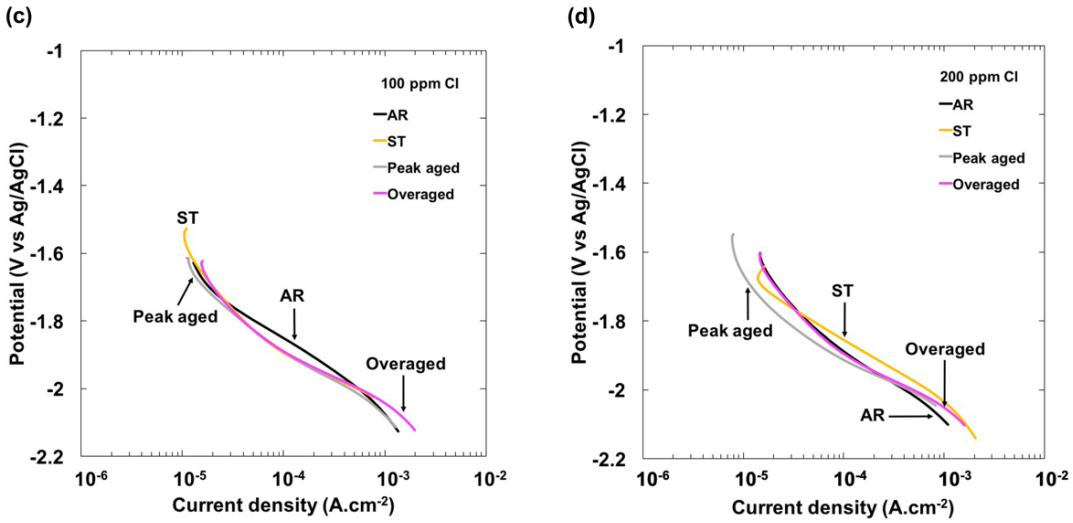

Fig. 2.4 Cathodic polarization plots of EV31A alloy in different heat-treated conditions in 0.1 M NaOH solution with different chloride (NaCl) additions: **(a)** no chloride addition, **(b)** 80 ppm chloride, **(c)** 100 ppm chloride, **(d)** 200 ppm chloride.

Table 2.3 Summary of the cathodic polarization results of EV31A alloy in different heat-treated conditions in 0.1 M NaOH with addition of different chloride concentrations.

Sample	Cl^- concentration	Tafel slope (V/dec)	Exchange current density for hydrogen evolution, i_0 (A/cm^2)	Over potential for 1 mA/cm^2 (V)
AR	No Cl^-	-0.14	1.3×10^{-11}	-1.11
	80 ppm	-0.21	4.0×10^{-9}	-1.11
	100 ppm	-0.18	1.8×10^{-9}	-1.07
	200 ppm	-0.18	9.0×10^{-10}	-1.08
ST	No Cl^-	-0.16	2.9×10^{-10}	-1.03
	80 ppm	-0.18	2.4×10^{-9}	-1.03
	100 ppm	-0.14	1.3×10^{-10}	-1.04
	200 ppm	-0.18	7.0×10^{-10}	-1.03
Peak-aged	No Cl^-	-0.19	4.0×10^{-9}	-1.25
	80 ppm	-0.18	3.8×10^{-10}	-1.05
	100 ppm	-0.16	1.5×10^{-10}	-1.07
	200 ppm	-0.13	1.2×10^{-11}	-1.05
Overaged	No Cl^-	-0.17	5.5×10^{-10}	-1.04
	80 ppm	-0.18	7.7×10^{-10}	-1.07
	100 ppm	-0.14	1.0×10^{-10}	-1.04
	200 ppm	-0.14	9.5×10^{-12}	-1.05

2.3.3 Potentiostatic Passivation

Figure 2.5(a) – (e) shows the *I-t* plots in log-log scale of the specimens in different chloride-containing solutions under potentiostatic conditions. The applied potential is in the middle of the passivation range of individual specimens based on their polarization curves shown in Fig. 2.3. Typically, this potential is around 0.5 $V_{Ag/AgCl}$. The anodic current density decayed almost linearly in the log-log scale. The passive current decay could be represented using the equation:

$$I = I_0 t^{-\alpha},$$

where I is passivation current at time t, I_0 is initial current density of the fresh specimen surface in the test environment, α is passivation kinetic exponent [45]. The value of α gives an idea about how quickly the surface can be passivated in a given environment. Higher the value of the α, faster is the passivation kinetics and better the microstructural condition. Negative values of α indicate that the current increases with time and there is passivity breakdown. Using this approach, different heat treatment conditions of the EV31A can be evaluated in 0.1 M NaOH solution with different chloride concentrations. The passivation kinetic exponent values are summarized in Table 2.4.

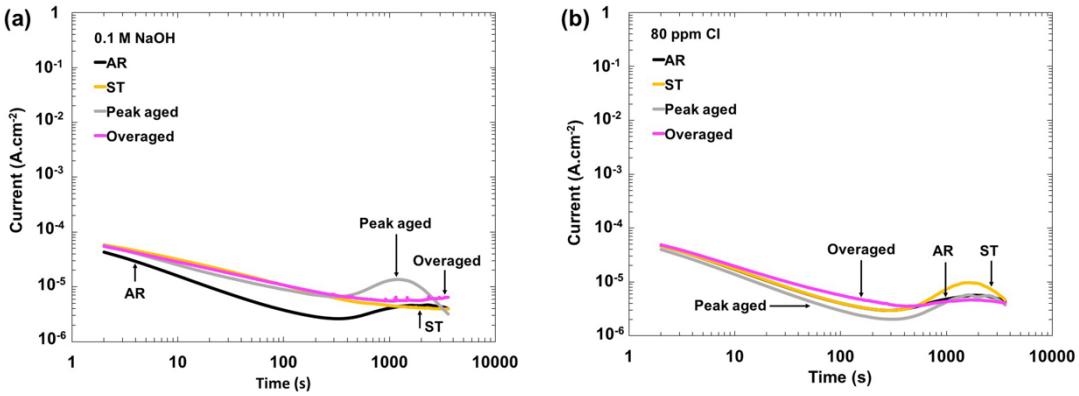

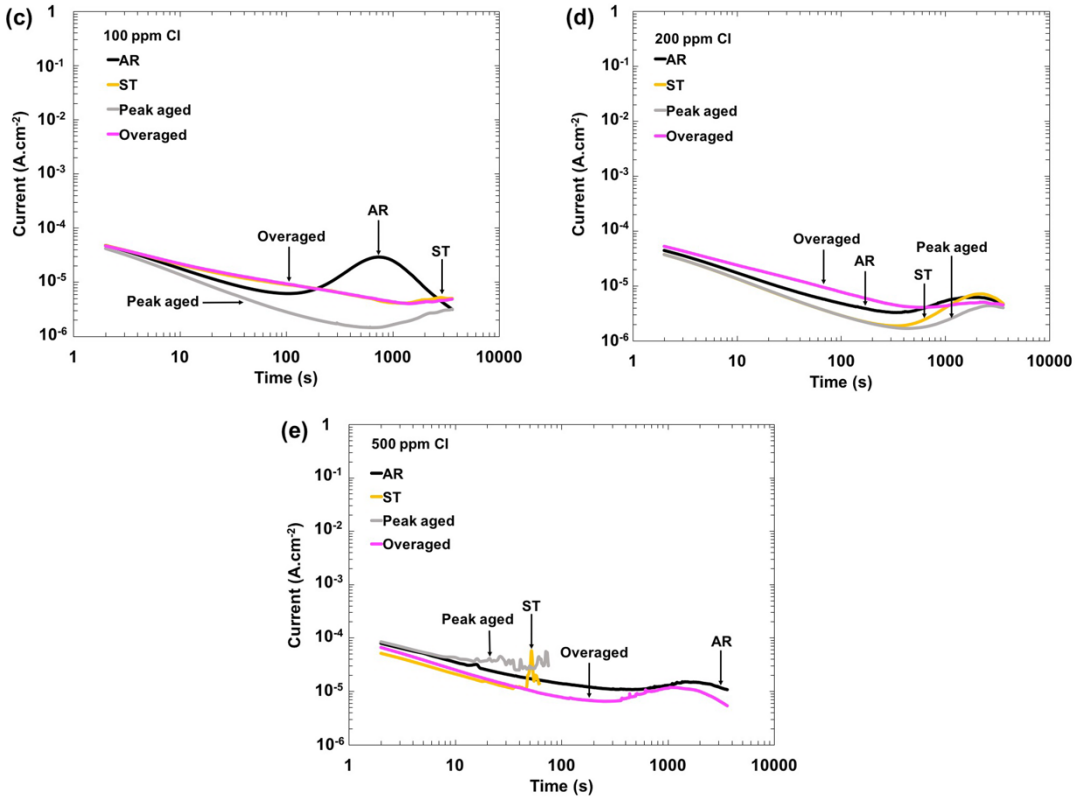

Fig. 2.5 *I-t* plots of EV31A specimens with different heat treatment conditions under potentiostatic control in 0.1 M NaOH solution with different chloride additions: **(a)** no chloride, **(b)** 80 ppm Cl^-, **(c)** 100 ppm Cl^-, **(d)** 200 ppm Cl^-, **(e)** 500 ppm Cl^-. The applied potential (typically 0.5 $V_{Ag/AgCl}$) was in the middle of the passivation range of the corresponding heat-treated condition as shown in Fig. 2.3.

Table 2.4 Passivation kinetic exponent and charge carrier density of EV31A specimens in different heat-treated conditions in different concentrations of chloride.

Sample	Cl^- concentration	Passivation kinetic exponent, α	Charge carrier density, N_D ($1/cm^3$)
AR	No Cl^-	0.684	2.08×10^{21}
	80 ppm	0.687	2.46×10^{21}
	500 ppm	0.55	5.42×10^{21}
ST	No Cl^-	0.46	1.29×10^{21}
	80 ppm	0.68	3.54×10^{21}
	500 ppm	0.57	N/A
Peak-aged	No Cl^-	0.48	3.50×10^{21}
	80 ppm	0.72	2.30×10^{21}
	500 ppm	0.47	N/A
Overaged	No Cl^-	0.42	1.87×10^{21}
	80 ppm	0.59	2.50×10^{21}
	500 ppm	0.55	5.49×10^{21}

In the absence of chloride, from Fig. 2.5(a) it can be seen that the AR specimen showed the fastest passivation kinetics during the first 100 s of passivation. This fast kinetics could be attributed to the textured microstructure, finer grain size and possibly high dislocation density of the AR specimen that promote fast diffusion of reactive elements through the short circuits of grain boundaries and dislocation channels. After reaching the lowest current density of about 2 $\mu A/cm^2$, the current starts to increase which could be due to dissolution of secondary phases or regions adjacent to the secondary phases.

The ST, PA and OA specimens exhibited more or less a similar passivation kinetics behavior in 0.1 M NaOH. Interestingly, the peak-aged specimen showed an increase in the current after 300 s of passivation and decay in current density after 1000 s. With the addition of chloride, it can be observed that the peak-aged specimen showed faster repassivation kinetics than any other heat-treated specimens, and the overaged specimen exhibited slower passivation kinetics.

Figure 2.6(a) – (d) illustrates the location of pit initiation in the specimens exposed to 500 ppm Cl^- + 0.1 M NaOH under potentiostatic control at 1.1 $V_{Ag/AgCl}$. The pit initiation predominantly occurred within the secondary phase particles in all the heat treatment conditions, as shown in Fig. 2.6(a) – (d). Particles with spherical morphology were more susceptible to localized dissolution than other morphologies. Dissolution is observed to start at

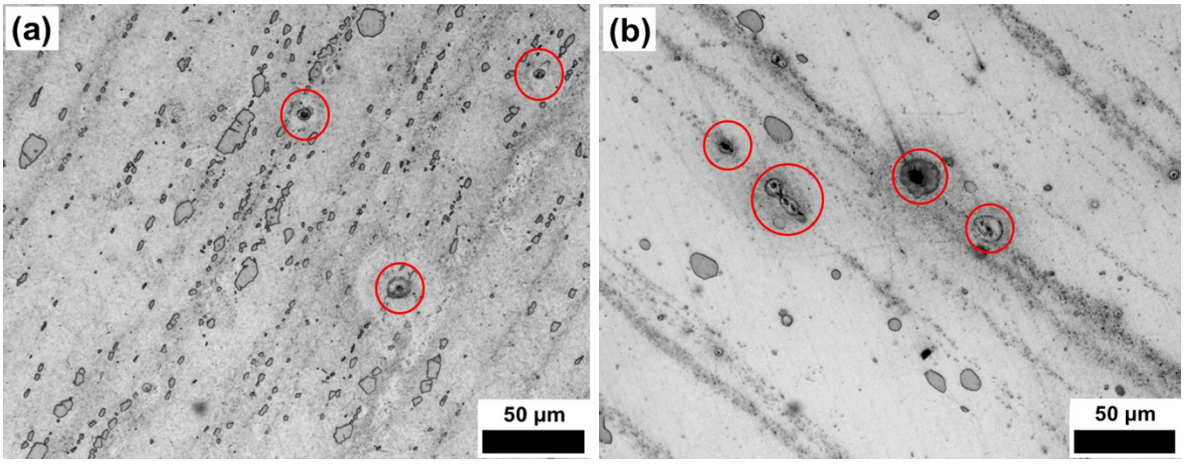

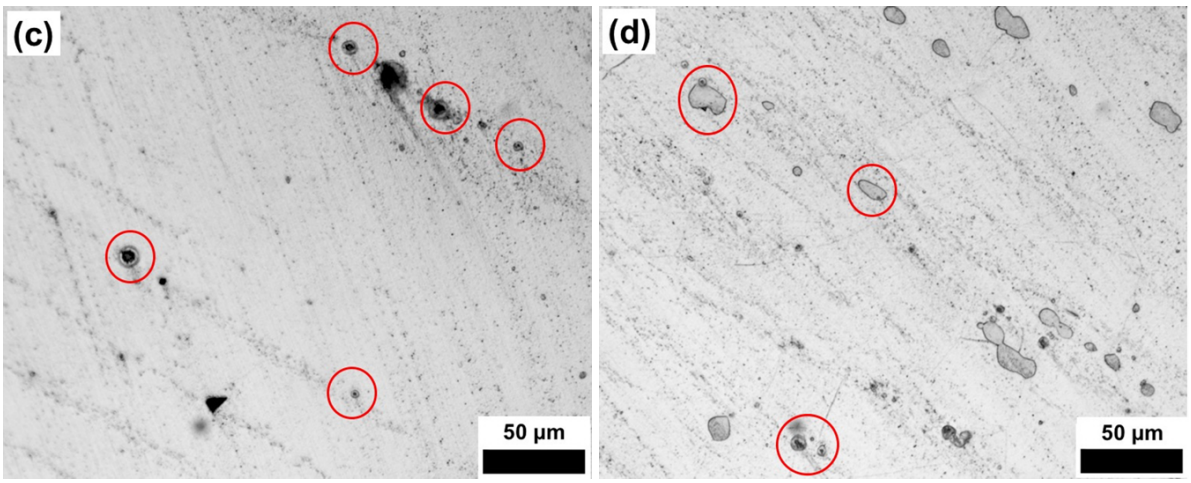

Fig. 2.6 Optical microstructures of the specimens under potentiostatic condition (1.1 $V_{Ag/AgCl}$) until pit initiation in 500 ppm Cl^- + 0.1 M NaOH: **(a)** as-received, **(b)** solution heat-treated, **(c)** peak-aged (200 °C, 16 h), **(d)** overaged (200 °C, 100 h).

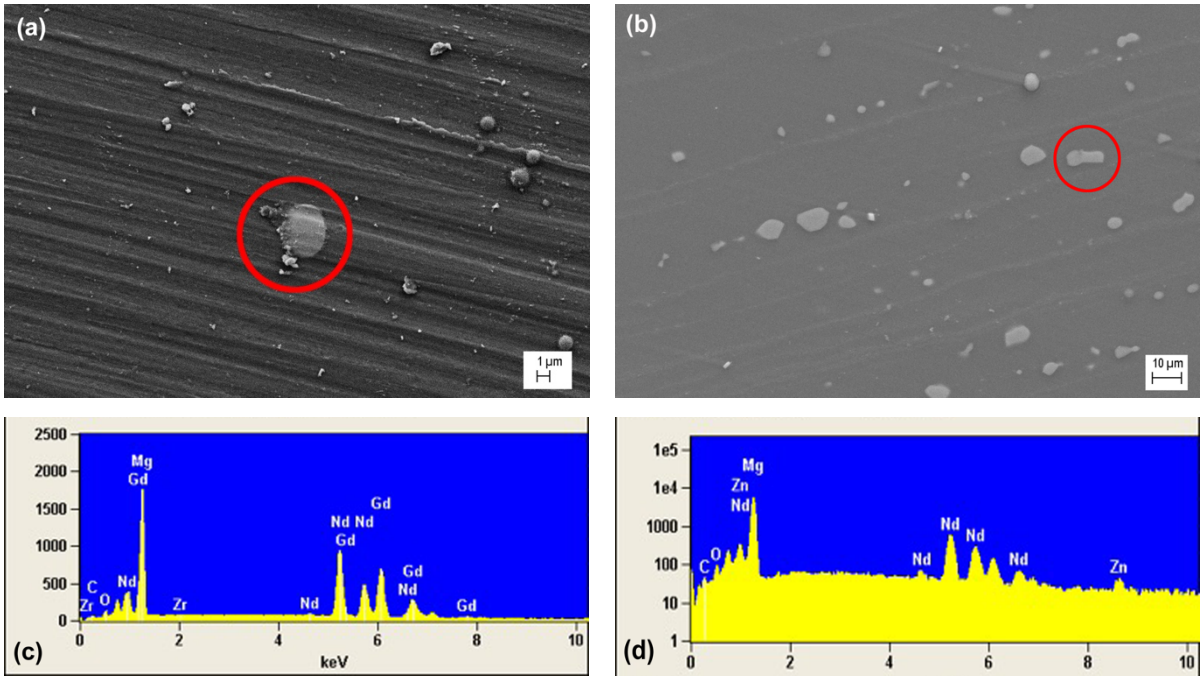

Fig. 2.7 SEM images of the solution heat-treated specimen before and after 1 h potentiostatic passivation at 0.5 $V_{Ag/AgCl}$ in 0.1 M NaOH solution: **(a)** before the test, **(b)** after the test, **(c)** EDX spectrum of elemental analysis of the circled particle in (a), **(d)** EDX spectrum of the circled particle shown in (b). Noted that the specimen in Fig. 2.7(a) was ground with SiC paper up to 600 grit, and specimen in Fig. 2.7(b) was ground up to 1-µm diamond suspension. The images do not show the exact same area.

the center of the spherical particle. The overaged specimen showed pit initiation at the interface between the secondary phase and the solid solution matrix as shown in Fig. 2.6(d). In this case, the particle had an irregular shape. In all the specimens, the spherical particles were observed to be enriched in Zr and Fe based on the scanning electron microscopy/energy-dispersive X-ray

(SEM/EDX) analyses. The selective attack could be attributed to dissolution of Zr in strong alkaline solutions. The particles that were not attacked represented a composition of Mg_3RE. The irregular-shaped particles in the OA specimen that exhibited attack at the interface are enriched in Nd and Zn. Figure 2.7(a) – (b) shows typical SEM images of the surface before and after corrosion testing. The typical energy-dispersive X-ray analyses of the secondary phase particles are shown in Fig. 2.7(c), (d). The particle circled in Fig. 2.7(a) could be identified as Mg_3RE phase, and the elongated particle circled in Fig. 2.7(b) could possibly be labeled as a mixture of Mg_7Zn_3 and Mg_5Nd.

The results of AC impedance spectroscopy are illustrated in Fig. 2.8(a) – (d) as Nyquist plots. The EIS measurements were carried out after passivating the specimens by applying a constant potential that was in the middle of the passivation range of the anodic polarization curve. The specimens were passivated for 1 h before running the EIS, and thus, the specimens might have only reached their quasi-steady states. Since the EIS data do not represent the steady-state conditions, the following analyses of the different heat treatment conditions are simply for comparative purpose.

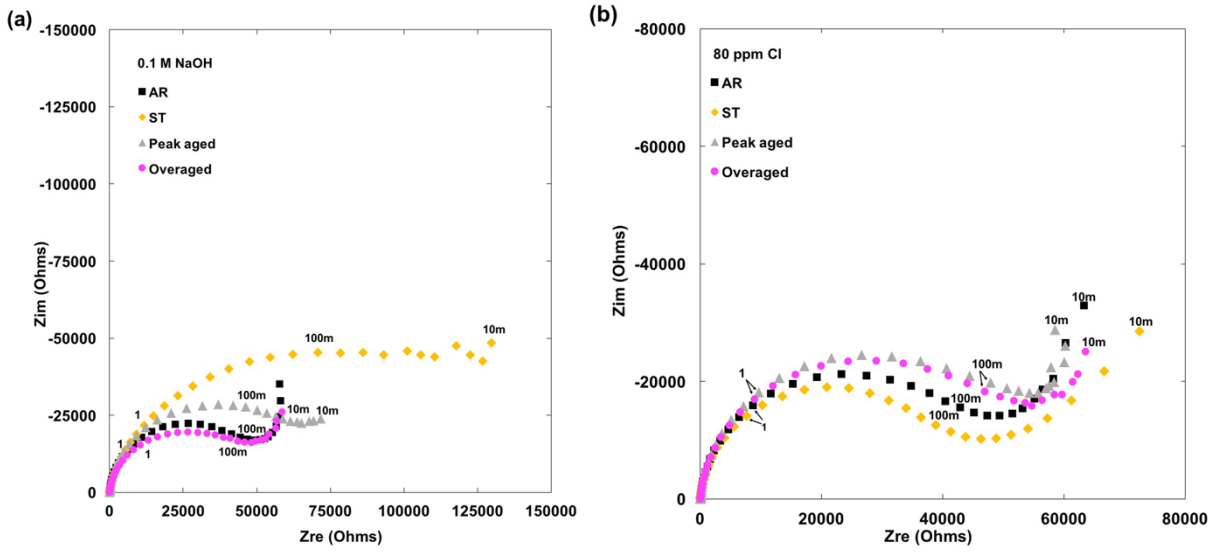

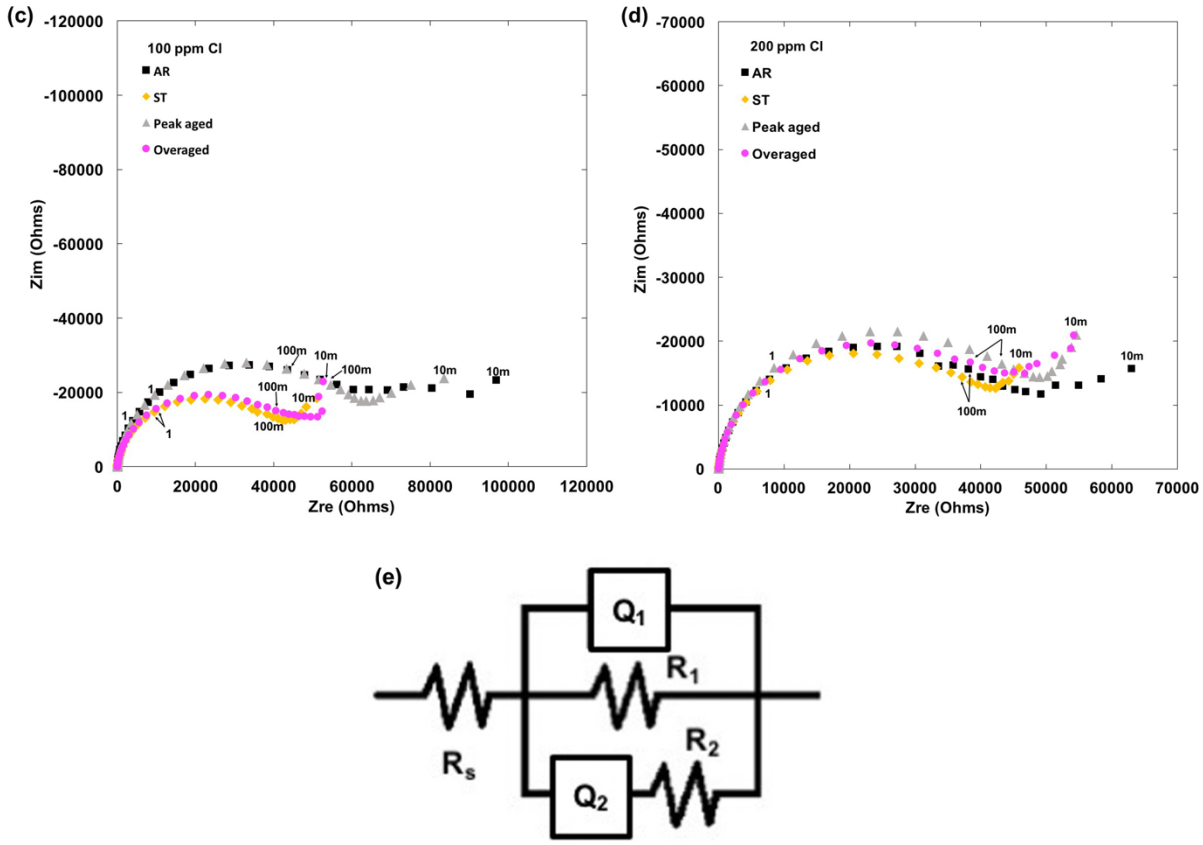

Fig. 2.8 Nyquist plots of EV31A specimens passivated at mid-potential of their passivation ranges for 1 h in 0.1 M NaOH solution with different chloride additions: **(a)** no chloride, **(b)** 80 ppm Cl^-, **(c)** 100 ppm Cl^-, **(d)** 200 ppm Cl^-, **(e)** electrical equivalent circuit fitted the data of Nyquist plots with $\chi^2 < 10^{-4}$.

In the 0.1 M NaOH without chloride addition, the overaged specimens showed the lowest magnitude of impedance spectrum among the investigated conditions, and the ST specimen showed the highest impedance spectrum. This trend more or less reversed with the addition of 80 ppm chloride. The impedance results could be correlated with the recorded passivation current densities of the respective specimens but not with the pitting protection potentials. The peak-aged specimens showed higher impedance spectra in 80, 100 and 200 ppm Cl^--containing solutions than the other heat-treated specimens.

The impedance data were initially fitted with different combinations of equivalent circuit elements to select a right model that gave the best fit with a low Chi-square value. Pinto et al. [32] fitted the EIS data of Mg-Zr alloys in pH 13 using Voigt circuit that contained 2-parallel RC loops connected in series with another resistor. When the same alloys were passivated in borated buffer solution, Pinto et al. [33] used 3-RC loops connected in series with one RC loop containing an inductor to account for the relaxation phenomena on the electrode

surface. Such relaxation occurred at low frequencies and was related to the adsorbed Mg^{+} reacting to $Mg2^{+}$ or $MgOH^{+}$ species as proposed by Baril et al. [46] and Anik and Celikten [47]. The presence of Mg^{+} ions has been disputed by other researchers [48], and Song et al. [49] attributed the inductive loop to the corrosion attack of the substrate. It should be noted that no inductive loops were recorded on any of the specimens in 0.1 M NaOH with or without chloride additions in this investigation.

Among different electrical equivalent circuits tried, the one illustrated in Fig. 2.8(e) fitted the data with $\chi^2 < 10^{-4}$. This equivalent circuit is more or less similar to the one proposed by Song [50] for concrete structures. In this equivalent circuit, R_s represents the electrolyte resistance, R_1 is associated with the charge transfer resistance, Q_1 (a constant phase element) is related to the electrode/electrolyte interfacial capacitance, R_2 is the resistance introduced by RE oxide/hydroxide incorporated in the $MgO/Mg(OH)_2$ surface layer, and Q_2 is the capacitance due to the surface layer space charge. The Q_1 and Q_2 are leaky capacitors with distributed time constants due to surface heterogeneity.

Table 2.5 summarizes the equivalent circuit values of the specimens in different chloride concentrations. The solution resistance values do not change significantly with the heat treatment condition and chloride addition. The values of Q_1 also are more or less similar among the test conditions. Significant variations are the Q_2 values that represented the passive layer conditions. A higher value of Q_2 indicates a more defective film that is less protective. The admittance values increase in general with increasing chloride concentration. The R_1 values associated with charge transfer resistance are large for the peak-aged and overaged specimens as summarized in Table 2.5. However, the R_1 value decreases significantly for the overaged specimen in 500 ppm Cl^{-} solution. Most of the values of R_2 do not change considerably with heat treatment or chloride additions. These results indicate that the passivation behavior is determined more by the capacitance values than by the resistance values of the passive layer. The semiconducting behavior of the passive layer is illustrated by Mott-Schottky plots. Figure 2.9 shows the Mott-Schottky plots of the overaged specimen in different chloride concentrations. Other heat-treated specimens also show a similar trend of Mott-Schottky behavior. The positive slopes of the $1/C^2$ vs potential plots indicate the *n*-type semiconducting nature of the passive layers. The charge carrier density values are summarized in Table 2.4. The charge carriers can be ascribed as ionic point defects such as oxygen vacancies or cation

Table 2.5 Equivalent circuit values of the specimens in different chloride concentrations.

Sample	Cl^- concentration (ppm)	R_s (Ohm)	Q_1 ($S \cdot s^{\alpha}$)	α	Q_2 ($S \cdot s^{\beta}$)	β	R_1 (Ohm)	R_2 (Ohm)
AR	0	51.59	9.063×10^{-6}	0.8	2.084×10^{-4}	0.8	5.642×10^{11}	4.956×10^{4}
	80	53.31	8.449×10^{-6}	0.9441	1.616×10^{-4}	0.5918	8.461×10^{16}	4.509×10^{4}
	500	55.41	9.759×10^{-6}	0.9475	2.536×10^{-5}	0.7867	4.933×10^{4}	1.011×10^{5}
ST	0	58.7	5.65×10^{-6}	0.9218	8.943×10^{-6}	0.2355	4.511×10^{5}	9.939×10^{-4}
	80	50.77	9.583×10^{-6}	0.9475	5.216×10^{-5}	0.8719	8.237×10^{4}	9.312×10^{4}
	500	-	-	-	-	-	-	-
Peak-aged	0	5.84×10^{-16}	1.393×10^{-5}	2.96×10^{-10}	1.313×10^{-5}	0.9162	2.274×10^{12}	56.36
	80	63.1	7.567×10^{-6}	0.9459	2.414×10^{-4}	0.7426	6.31×10^{13}	5.434×10^{4}
	500	-	-	-	-	-	-	-
Overaged	0	48.64	7.823×10^{-6}	0.9255	8.999×10^{-7}	0.4205	5.732×10^{13}	3.668×10^{4}
	80	51.18	8.189×10^{-6}	0.9384	1.664×10^{-4}	0.5575	1.353×10^{18}	4.977×10^{4}
	500	49.46	1.055×10^{-5}	0.9494	3.477×10^{-5}	0.6005	8.024×10^{4}	1.009×10^{5}

(such as Mg^{2+}, Nd^{3+}, Gd^{3+}, Zn^{2+}) interstitials. The defect density increases with increasing chloride content of the electrolyte for a given heat treatment condition except for the peak-aged condition. The ST and OA specimens show passive layers with lower charge carrier densities in 0.1 M NaOH without chloride condition. The increase in defect density with increasing chloride concentration of electrolyte could be correlated with the susceptibility of the OA specimen to localized corrosion.

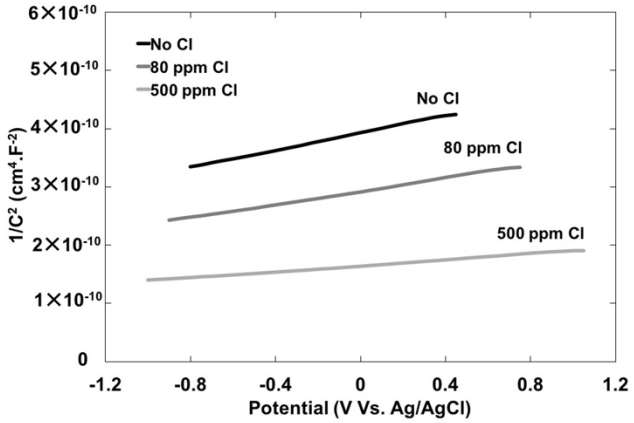

Fig. 2.9 Mott-Schottky plots of overaged (200 °C for 100 h) specimen in solution with different chloride concentrations.

2.4 Conclusions

1) Polarization of the specimens to transpassive potentials (> 1.6 $V_{Ag/AgCl}$) introduced defects in the passive layers and possibly changed the surface area by dissolution of active elements. Therefore, a small hysteresis could be observed even in the absence of chloride during the reverse scan of the cyclic polarization.

2) No passivity breakdown was observed up to 80 ppm chloride addition for specimens with any heat treatments.

3) The pitting protection potentials of the solution heat-treated and peak-aged specimens remained high at about 1.1 $V_{Ag/AgCl}$ in the basic solution 0.1 M NaOH containing up to 200 ppm chloride addition.

4) Significant reduction in pitting protection potentials was observed with 500 ppm chloride addition and a 1000 ppm chloride addition caused complete passivity breakdown for all the specimens with different heat treatments.

5) Overall, the peak-aged (200 °C, 16 h) specimen showed better corrosion resistance than specimens with any other heat treatments.

Acknowledgements

The support provided by the US Nuclear Regulatory Commission through a faculty development grant NRC-HQ-84-15-G-0025 is gratefully acknowledged. J. Ninlachart acknowledges the support by Royal Thai Navy.

References

[1] Y. Huang, W. Gan, K.U. Kainer, N. Hort, J. Magnes. Alloys **2**, 1 (2014)

[2] N. Stanford, D. Atwell, A. Beer, C. Davies, M.R. Barnett, Scripta Mater. **59**, 772 (2008)

[3] G.L. Markar, J. Kruger, Int. Met. Rev. **38**, 138 (1993)

[4] L.L. Rokhlin, *Mg Alloys Containing RE Metals* (Taylor and Francis, London, 2003)

[5] Z.L. Ning, H. Wang, H.H. Liu, F.Y. Cao, S.T. Wang, J.F. Sun, Mater. Des. **31**, 4438 (2010)

[6] G. Riontino, D. Lussana, M. Massazza, G. Barucca, P. Mengucci, R. Ferragut, J. Alloys Compd. **463**, 200 (2008)

[7] Elektron 21 Data sheet: 455, Magnesium Elektron UK (2006)

[8] R. Arroyave, D. Shin, Z.K. Liu, Calphad **29**, 230 (2005)

[9] S. Bhan, A. Lal, J. Phase Equilib. **14**, 634 (1993)

[10] P.H. Fu, L.M. Peng, H.Y. Jiang, C.Q. Zhai, X. Gao, J.F. Nie, Mater. Sci. Forum **97**, 546 (2007)

[11] A.A. Nayeb – Hashemi, J.B. Clark, The Mg-Nd system. Bull. Alloy Phase Diagrams **9**, 618 (1988)

[12] S. Delfino, A. Saccone, R. Ferro, Metal. Trans. A **21**, 2109 (1990)

[13] P. Lyon, T. Wilks, I. Syed, ed. by N.R. Neelameggham, H.I. Kaplan, B.R. Powell, Magnes. Technol. 2005. TMS 303 (2005)

[14] J.F. Nie, X. Gao, S.M. Zhu, Scripta Mater. **53**, 1049 (2005)

[15] A. Kielbus, T. Rzychon, R. Przeliorz, Mater. Sci. Forum **638 – 642**, 1447 (2010)

[16] A. Kielbus, T. Rzychon, L. Litynska-Dobrzynska, G. Dercz, Solid State Phenom. **163**, 106 (2010)

[17] D.H. Ping, K. Hono, J.F. Nie, Scripta Mater. **48**, 1017 (2003)

[18] L.R. Gill, G.W. Lorimer, P. Lyon, Adv. Eng. Mater. **9**, 784 (2007)

[19] G. Williams, K. Gusieva, N. Birbilis, Corros. (NACE) **68**, 489 (2012)

[20] P. Maier, R. Peters, C.L. Mendis, S. Muller, N. Hort, JOM **68**, 1183 (2016)

[21] T. Cain, L.G. Bland, N. Birbilis, J.R. Scully, Corros. (NACE) **70**, 1043 (2014)

[22] A.D. Sudholz, N.T. Kirkland, R.G. Buchheit, N. Birbilis, Electrochem. Solid-State Lett. **14**, C5 (2011)

[23] F. Czerwinski, Int. Mater. Rev. **60**, 264 (2015)

[24] X. Xia, J.F. Nie, C.H.J. Davies, W.N. Tang, S.W. Xu, N. Birbilis, Corros. (NACE) **71**, 1370 (2015)

[25] K.M. Ismail, S. Virtanen, Electrochem. Solid-State Lett. **10**, C9 (2007)

[26] M. Taheri, J.R. Kish, J. Electrochem. Soc. **160**, C36 (2013)

[27] S. Li, A.C. Bacco, N. Birbilis, H. Cong, Corros. Sci. **112**, 596 (2016)

[28] G.L. Song, K.A. Unocic, Corros. Sci. **98**, 758 (2015)

[29] F. Cao, G.L. Song, A. Atrens, Corros. Sci. **111**, 835 (2016)

[30] G.L. Song, K.A. Unocic, M. Harry III, E. Cakmak, M.P. Brady, P.E. Gannon, P. Himmer, Q. Andrews, Corros. Sci. **104**, 36 (2016)

[31] H.B. Yao, Y. Li, A.T.S. Wee, Electrochim. Acta **48**, 4197 (2003)

[32] R. Pinto, M.G.S. Ferreira, M.J. Carmezim, M.F. Montemor, Electrochim. Acta **55**, 2482 (2010)

[33] R. Pinto, M.G.S. Ferreira, M.J. Carmezim, M.F. Montemor, Electrochim. Acta **56**, 1535 (2011)

[34] M. Pourbaix, *Atlas of Electrochemical Equilibria in Aqueous Solutions* (NACE International, CEBELCOR, Houston Texas, Brussels, 1974), pp.139 – 145

[35] D. Wu, Y.Q. Ma, R.S. Chen, W. Ke, J. Magnes. Alloys **2**, 20 (2014)

[36] D.A. Jones, *Principles and Prevention of Corrosion*, 2nd edn. (Prentice-Hall, New Jersey, 1996)

[37] P.W. Chu, E.A. Marquis, Corros. Sci. **101**, 94 (2015)

[38] K.S. Raja, D.A. Jones, Corros. Sci. **48**, 1623 (2005)

[39] M. Pourbaix, *Atlas of Electrochemical Equilibria in Aqueous Solutions* (NACE International, CEBELCOR, Houston Texas, Brussels, 1974), pp. 197

[40] M.G. L-B Natta, Corrosion **57**, 714 (2001)

[41] E. Gileadi, *Physical Electrochemistry* (Wiley-VCH, Weinheim, 2011), pp. 98 – 99

[42] G. Song, A. Atrens, D. St. John, X. Wu, J. Nairn, Corros. Sci. **39**, 1981 (1997)

[43] G.S. Frankel, A. Samaniego, N. Birbilis , Corros. Sci. **70**, 104 (2013)

[44] S.H. Salleh, S. Thomas, J.A. Yuwono, K. Venkatesan, N. Birbilis, Electrochim. Acta **161**, 144 (2015)

[45] G.T. Burstein, D.H. Davies, J. Electrochem. Soc. **128**, 33 (1981)

[46] G. Baril, G. Galicia, C. Deslouis, N. Pebere, B. Tribollet, V. Vivier, J. Electrochem. Soc. **154**, C108 (2007)

[47] M. Anik, G. Celikten, Corros. Sci. **49**, 1878 (2007)

[48] S. Thomas, N.V. Madhekar, G.S. Frankel, N. Birbilis, Curr. Opin. Solid State Mater. Sci. **19**, 85 (2015)

[49] Y. Song, E.H. Han, K. Dong, D. Shan, C.D. Yim, B.S. You, Corros. Sci. **88**, 215 (2014)

[50] G.L. Song, Cem. Concr. Res. **30,** 1723 (2000)

CHAPTER 3

Effect of Heat Treatment Conditions on the Passivation Behavior of WE43C Mg-Y-Nd Alloy in Chloride Containing Alkaline Environments

Jakraphan Ninlachart [a], Zachary Karmiol [b], Dev Chidambaram [b], Krishnan S. Raja [a]

[a] Chemical and Materials Engineering, University of Idaho, Moscow, ID 83844-1021, USA

[b] Chemical and Materials Engineering, University of Nevada, Reno, NV 89557-0388, USA

Effect of Heat Treatment Conditions on the Passivation Behavior of WE43C Mg-Y-Nd Alloy in Chloride Containing Alkaline Environments. *Journal of Magnesium and Alloys*, (2017) doi: 10.1016/j.jma.2017.03.003.

Abstract

Mg-Y-Nd alloy (WE43C or Elektron 43) is a heat treatable magnesium wrought alloy that can be used up to 250 °C for aerospace application. This alloy has excellent mechanical properties (UTS: up to 345 MPa at room temperature) and improved corrosion resistance. Electrochemical passivation studies were conducted on this alloy under different heat treatment conditions in 0.1 M NaOH solution with the addition of chloride from 0 to 1000 ppm. The passive potential range typically extended to more than 1.5 $V_{Ag/AgCl}$. The transpassive potential was not dependent on the heat treatment condition when the chloride concentration increased up to 500 ppm. However, pitting protection potential varied with the heat treatment condition when the chloride addition was 500 ppm or more. The specimen surface was analyzed using scanning electron microscopy (SEM), X-ray diffraction (XRD), X-ray photoelectron spectroscopy (XPS), and Raman spectroscopy to understand the passivation behavior of this alloy. The passivated surface of the WE43C specimens indicated that the surface layer consisted of MgO, $Mg(OH)_2$, and rare earth oxide phases, and the heat treatment conditions did not significantly affect the composition of the surface film.

Keywords: Elektron 43; Magnesium alloy; Corrosion; Passivation; Chloride

3.1 Introduction

Yttrium containing Mg alloys are used in biomedical and creep resistant applications [1, 2]. Yttrium has a similar standard electrochemical potential as that of magnesium, and forms intermetallic secondary phases, such as MgY, Mg_2Y, and $Mg_{24}Y_5$ with magnesium. Increase in the volume fraction of $Mg_{24}Y_5$ was found to accelerate the corrosion by microgalvanic effect [3]. WE43 contains 4 wt% Y and about 3 wt% Nd. The alloy is typically solution treated at 525 °C for 8 h and water quenched. Aging is carried out in the temperature range of 150 – 280 °C in air [4]. Unlike Mg-Nd alloys (such as EV31A), formation of Guinier-Preston zone was not reported for Mg-Y-Nd alloys during early stages of precipitation hardening [5]. The precipitation reaction sequence is reported as follows: supersaturated solid solution → β'' ($Mg_3Y_{0.85}Nd_{0.15}$) with hexagonal $D0_{19}$ super lattice → β′ ($Mg_{12}YNd$) with body centered orthorhombic structure → β_1 ($Mg_{14}YNd_2$) with FCC structure (a = 0.74 nm) → β ($Mg_{14}YNd_2$) with FCC structure (a = 2.223 nm) [6]. Two different chemistries of β_1 phase have been reported such as $Mg_{14}Nd_2Y$ [6] and Mg_3RE [7]. Low temperature aging treatment at 150 °C promoted the formation of coherent β″ precipitates that resulted in a peak hardness of 85 VHN after 500 minutes of aging. Increasing the aging temperature to 210 °C led to formation of predominantly β′ phase and a maximum hardness of about 100 VHN after 1000 minutes of aging [4]. Conventional T6 aging treatment at 250 °C gave rise to precipitation of β′, β_1, and traces of β phases. This temperature is above the solvus temperature of β″ phase. Further increase in the aging temperature to 280 °C caused formation of the equilibrium β phase and overaging [4, 7, 8].

Chang et al. studied the electrochemical behavior of NZ30K alloy containing 3 wt% Nd and 0.4 wt% Zr in 5% NaCl solution at different heat treated conditions and observed better corrosion resistance in solution treated condition due to dissolution of cathodic secondary phases in the solid solution [9]. Atrens and coworkers [2] investigated binary Mg-Y alloys with Y contents ranging from 2 to 7 wt% in 0.1 M NaCl and 0.1 M Na_2SO_4 solutions. In chloride containing solution, presence of Y-rich secondary phases detrimentally affected the corrosion resistance. On the other hand, in Na_2SO_4 solution, the corrosion resistance increased because of the incorporation of Y in the surface layer that improved the protectiveness. The microgalvanic effect induced by the Y-rich surface film in the mild Na_2SO_4 electrolyte. Birbilis

and coworkers also investigated the corrosion behavior of Mg-Y binary alloys with up to 18 wt% Y addition in 0.1 M NaCl solution [3]. The corrosion rate was observed to increase with increase in the Y content. The increased corrosion was attributed to the enhanced cathodic activity of the Y-rich phases such as $Mg_{24}Y_5$, Mg_2Y, and MgY. Incorporation of Y in the oxide layer was not considered to be beneficial at pH lower than 10 due to the solubility of the Y-oxide at low pH conditions.

Atrens and coworkers [10] investigated high purity Mg-RE binary cast alloys in solution treated conditions by removing Fe-impurity by Zr addition. The Fe content of Mg-5Y alloy specimens was in the range of 48 – 59 ppm and Zr was in the range of 141 – 149 ppm. The solution treated Mg-5Y alloy specimens showed cathodic and anodic Tafel slope of – 268 and 90 mV/decade, respectively. The corrosion current density was about 20 times as that of high purity magnesium samples. The high corrosion rate of Mg-RE alloys was attributed to the galvanic effect due to the presence of intermetallic particles in spite of the solution treatment. Zhang et al. [11] studied the corrosion behavior of extruded Mg-Y alloys in NaCl solution. They observed that increase in the Y content of the specimens from 5.23 wt% to 13.78 wt% decreased the grain size but the corrosion rate increased even though the corrosion potential become nobler with the addition of Y.

WE43 alloy has been investigated widely as a potential bioimplant material by several investigators [12 – 15]. Ascencio et al. [12] characterized the corrosion behavior of WE43 in modified simulated body fluid using electrochemical impedance spectroscopy and proposed a dual layer surface film for the observed corrosion protection during the initial immersion period up to 96 h. Jamesh et al. compared the corrosion behavior of WE43 and ZK60 alloys in Ringer's solution and simulated body fluid. These authors observed that WE43 showed better corrosion resistance than ZK60 due to smaller potential difference between the matrix and intermetallic phases of the WE43 alloy [13]. The corrosion resistance of WE43 for biomedical applications was reportedly improved by Nd-ion implantation on the surface [14] and Hf-ion implantation [15]. Formation of hydrophobic surface layer predominantly consisting of Nd_2O_3-MgO was attributed to the improved corrosion resistance of the Nd-implanted material.

Taylor and coworkers [16] reported fresh surface film formed on molten Mg-Nd alloy in different atmospheres. They found that the oxidation rate of Mg-Nd alloys at high temperature in dry air atmosphere decreased because of the duplex structure of MgO and Nd_2O_3

film formed during solidification of the casting. Marcus and coworkers [17] reported the corrosion behavior of WE43 alloy in Na_2SO_4 electrolyte. The corrosion current density of WE43 was observed to be about 11 times smaller than that of pure Mg (581 $\mu A/cm^2$ vs 6442 $\mu A/cm^2$). The improved corrosion film that consisted of a $Mg(OH)_2$ outer layer and a mixed oxide inner layer enriched with the oxides/hydroxides of the alloying elements such as Y, Nd, and Zr.

Zhang and coworkers [18] reported the surface chemistry on AZ31 and AZ91 by using the X-ray photoelectron spectroscopy (XPS). The results showed that the outer layer was composed of $Mg(OH)_2$ and $MgCO_3$, and the inner layer was composed of $Mg(OH)_2$, MgO, and $MgCO_3$. These layers formed both in corrosion zone and passivation zone. However, $Mg(OH)_2$ predominated in corrosion zone and caused corrosion on metallic surface, whereas MgO was dominant in the passivation zone that improved the corrosion resistance. When Mg alloys were stored in humid air a naturally formed surface layer containing $MgCO_3$, $Mg(OH)_2$, and MgO was reported [19].

The literature search indicated that most of the corrosion studies of Mg-RE alloys have been carried out in chloride containing solutions that are mimicking either marine or biological environment. Furthermore, most of the investigations pertained to cast Mg-RE alloys and not much has been reported on the wrought Mg-RE alloys. This present work focuses on the passivation behavior of the wrought WE43 alloy in dilute alkaline solution containing different chloride concentrations. Such an alkaline pH condition may not represent a real life service condition, but this study will be of fundamental in nature and might help understand the passivation behavior of the WE43 alloy and its breakdown in the presence of chloride.

3.2 Experimental Methods

3.2.1 Material and Characterization

Mg-Y-Nd alloy (Elektron 43 or WE43C) plate having a thickness of 16 mm was supplied by Magnesium Elektron N.A. Inc. The nominal composition of the alloy based on the energy dispersive X-ray analysis was: 3.6 wt% Y, 2.6 wt% Nd, 0.93 wt% Gd, 0.6 wt% Zr, 0.2 wt% Si and balance Mg. The plate was sliced into 3 mm thick and 16×25 mm^2 size coupons. The samples were investigated for their passivation behavior in four different heat treatment conditions such as 1) as-received (AR), 2) solution treated (ST), 3) solution-treated and peak

aged (PA), and 4) solution treated and overaged (OA). The as-received (AR) samples were not given any additional heat treatment. The solution treated specimens were solution annealed at 525 °C for 8 h and quenched in room temperature water. The peak aged (PA) samples underwent solution treatment followed by aging at 200 °C for 168 h. Overaging treatment was carried out by aging the solution treated samples at 300 °C for 2 h. The specimens for the electrochemical testing were metallographically polished with SiC paper down to 600 grit, rinsed with ethanol, and dried in air for doing the corrosion tests. The specimens for the hardness test and microstructure evaluations were ground with SiC paper down to 1200 grit and polished with 1-μm diamond suspension, rinsed with ethanol, and dried in air. The etchant was a mixture of 10 ml of HNO_3, 24 ml of DI water, and 75 ml of ethylene glycol. Microstructural evaluations were carried out using a metallographic microscope (OLYMPUS PMG3) and an electron microscope (FESEM: LEO SUPRA 35VP). Microhardness measurements were carried out using LECO LM100 with a load of 10 grams. The reported values are average of minimum ten readings in each specimen.

3.2.2 Electrochemical Environments

The test solutions for the electrochemical experiments were 0.1 M NaOH solution (pH: ~13) and 0.1 M NaOH with the addition of chloride in the concentrations of 80 ppm (2.25×10^{-3} mol/l), 100 ppm (2.82×10^{-3} mol/l), 200 ppm (5.64×10^{-3} mol/l), 500 ppm (14.1×10^{-3} mol/l) and 1000 ppm (28.2×10^{-3} mol/l). The chloride was in the form of NaCl. High purity water (resistivity 18.2×10^{6} Ω·cm) was used for preparing the test solutions using a water purifier (MilliPore Medel: Milli-QPF Plus). All chemicals were regent grade.

3.2.3 Electrochemical Tests

The electrochemical tests were conducted by using a 3-electrode configuration. A platinum spiral wire was the counter electrode, AgCl coated Ag wire (1 mm diameter) immersed in saturated KCl was the reference electrode, and the sample was the working electrode. The potential employed was VersaSTAT MC with VersaStudio software version 2.42.3, and ZSimpWin 3.60 software from Princeton Applied Research. The exposed surface area of the samples to the solution was 1 cm^2. The cyclic polarization was carried out by scanning the potential from 0 V vs open circuit potential (OCP) to 2.5 V vs reference (Ag/AgCl) at a scan

rate of 1 mV/s. After reaching either a potential of 2.5 $V_{Ag/AgCl}$ or 1 mA/cm^2 of transpassive current density (whichever occurred earlier), the scan direction was reversed and scanned back to OCP. The potentiostatic tests were conducted at the middle potential of the passivation range (typically at 0.5 $V_{Ag/AgCl}$) for 3600 s. Electrochemical impedance spectroscopy (EIS) was measured under potentiostatic condition by applying the passivating potential and superimposing an AC signal of 10 mV, and scanning from the frequency of 100 kHz to 10 mHz. Mott-Schottky was measured at 316 Hz of frequency by scanning the potential from the middle of the passivation range to OCP at 50 mV steps.

3.2.4 Characterization of Passivated Surface

After potentiostatic passivation tests, the surfaces of select samples were analyzed using gracing angle XRD, XPS, and Raman spectroscopy. Gracing angle X-ray diffraction patterns were obtained using a Rigaku Smartlab 3 kW with Cu Kα X-ray tube operated to 40 kV and 44 mA, where the incident angle of the X-rays was 0.5° with respect to the sample surface. X-ray photoelectron spectroscopy (XPS) analysis was conducted using a PHI 5600 calibrated to the Ag 3d5/2 line at 368.3 ± 0.05 eV. Spectra were obtained with monochromatic Al Kα radiation source as well as a Mg Kα radiation source, both at an accelerating voltage of 14 kV and 300 W over an analysis area of 0.5 mm^2, and an angle of 60° to the detector. A Thermo-Scientific DXR dispersive Raman microscope was used to characterize the Raman vibrational modes of the surface films. Raman spectra were obtained for individual spots with a diameter of 0.7 μm with 4 exposures of 8 seconds at 100X magnification using a 532 nm laser operated at 10 mW.

3.3 Results and Discussion

3.3.1 Microstructural Characterization

The as-received material Mg-4Y-2.25Nd-0.5Zr WE43C was in the precipitation heat treated (T5) condition. The microstructure of the as-received (AR) material is shown in Fig. 3.1(a). The texture developed during the rolling process could be seen. The grain size is finer in the AR condition. The XRD pattern of the as-received specimen is given in Fig. 3.2(a). Minor peaks corresponding to secondary phases of $Mg_{12}Nd$, $Mg_{24}Y_5$, $Mg_{41}Nd_5$, and Mg_3Gd could be observed. The Vickers hardness of the as-received specimen was about 96 kgf/mm^2. Figure 3.3(a) shows the SEM image of the microstructure of the AR specimen after etching

with dilute nitric acid in ethylene glycol-water mixture. The grain boundaries were etched deeply. The grain boundaries were decorated with precipitation of secondary phase particles having irregular and cubic shapes. EDAX analysis identified the large cubic precipitates as Mg_2Y as shown in Fig. 3.3(b). Since etching caused removal of the precipitates, SEM images were taken on the as-polished surface without etching. A typical result is shown in Fig. 3.3(c). The EDAX analyses of the secondary phase particles indicated presence of different phases such as $Mg_{12}RE$ (where RE denotes Y, Nd, and Gd), Zr-rich phase, and Zr and Y rich phase.

When the alloy was solution treated, the hardness decreased to 70 kgf/mm^2, as seen in Fig. 3.2(b). Most of the minor peaks corresponding to secondary phases were not revealed in the XRD pattern of the solution treated (ST) specimen as seen in Fig. 3.2(a). However, a peak corresponding to $Mg_{12}Nd$ was still present. Significant grain growth after solution treatment could be observed as shown in Fig. 3.1(b). The grain size of the ST specimen was in the range of 25 – 46 μm. Figure 3.4(a) illustrates the SEM microstructure of the solution treated condition, where undissolved secondary phases are visible along the grain boundaries and inside the grains as well. The line scan of the EDAX indicated the large particle to have a chemistry matching Mg_3RE, as seen in Fig. 3.4(b). The smaller precipitates could be associated with the chemistry of $Mg_{12}RE$ phase which supported the XRD result.

Figure 3.1(c) shows the microstructure of the peak aged (PA) specimen at 200 °C for 168 h. The average hardness was 103 kgf/mm^2. The XRD pattern showed presence of $Mg_{41}Nd_5$, Mg_3Gd, $Mg_{24}Y_5$, and $Mg_{12}Nd$ phases along with α-Mg, as seen in Fig. 3.2(a). These results could be corroborated with the SEM microstructures and the EDAX analyses of the precipitates as shown in Fig. 3.5(a) and (b). Cuboid shaped precipitates identified from the elemental analysis as Mg_2Y phase were not revealed in the XRD pattern probably due their low volume fraction. It should be noted that the hardness value of this peak aging treatment was higher than that normally reported for the conventional T6 treatment (250 °C for 16 h aging that results in ~85 kgf/mm^2). The high hardness value could be attributed to the possible presence of coherent β″ precipitates of $Mg_3Y_{0.85}Nd_{0.15}$ or Mg_3RE type that were not revealed in the XRD [4]. SEM could not resolve the β″ phase due its nanostructure and dimension of less than 10 nm. The XRD peak corresponding to Mg_3Gd could indicate presence of β_1 phase that has FCC structure.

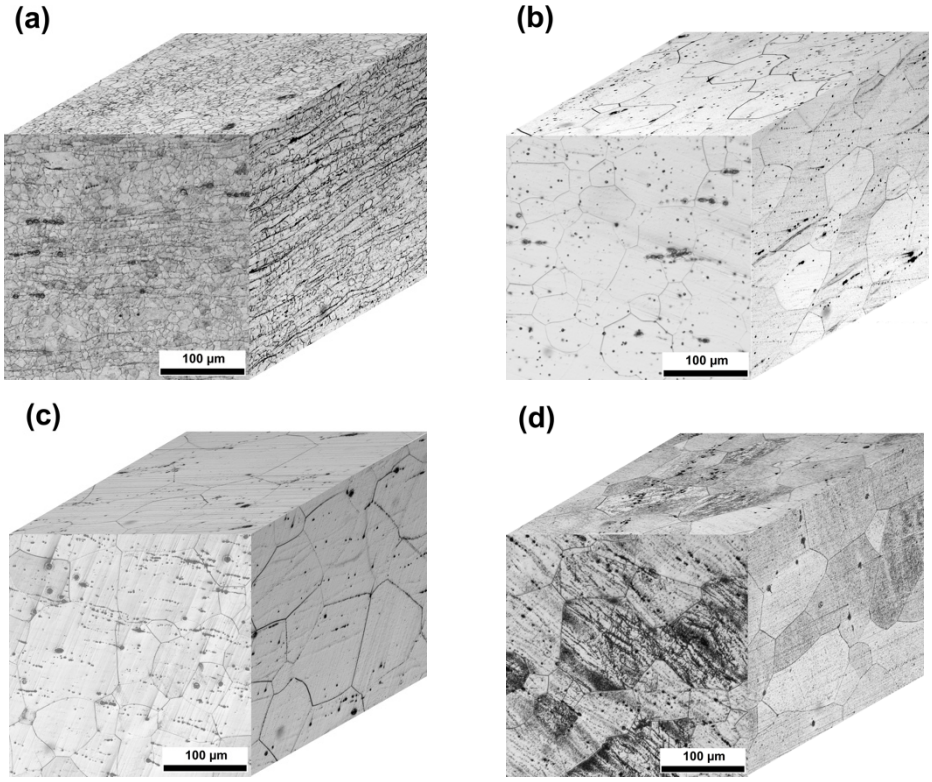

Fig. 3.1 Optical microstructures of WE43C in different heat treated conditions (3-D faces and rolling direction: *Top*: Longitudinal, *Front*: Short transverse, *Side*: Long transverse): **(a)** as-received, **(b)** solution treated, **(c)** peak aged (200 °C, 168 h), **(d)** overaged (300 °C, 2 h).

Aging the WE43C at 300 °C for 2 h after solution treatment showed marginal increase in the hardness value from 70 to 73 kgf/mm^2, as seen in Fig. 3.2(b). The XRD pattern of this aging condition was not very different from that of peak-aged condition. However, the sample was etched darker than other samples such as ST and PA as seen in Fig. 3.1(d). Based on the hardness and etching conditions, aging at 300 °C for 2 h was considered as overaged (OA) condition. Furthermore, the aging temperature was higher than the solvus temperature of the coherent β″ phase and therefore in the absence of β″ not much precipitation hardening could occur. The phases expected in this heat-treated condition are (in the decreasing order): β ($Mg_{14}Nd_2Y$, FCC), β_1 ($Mg_{14}Nd_2Y$, Mg_3RE, FCC), β′ ($Mg_{12}RE$, BCO), and $Mg_{41}Nd_5$. Another intermetallic phase, $Mg_{24}Y_5$ normally reported in the Mg-Y alloys, has also been identified in this study. Figure 3.6(a) and (b) shows the SEM microstructure and EDAX line scan analysis of the overaged material in etched condition. The etching removed the β-phase particles that showed plate-like morphology. The grain boundary precipitates contained Zr-rich particles.

The plate morphology of the β-phase with a chemistry of $Mg_{41}RE_3$ could be seen in the unetched condition as shown in Fig. 3.6(c).

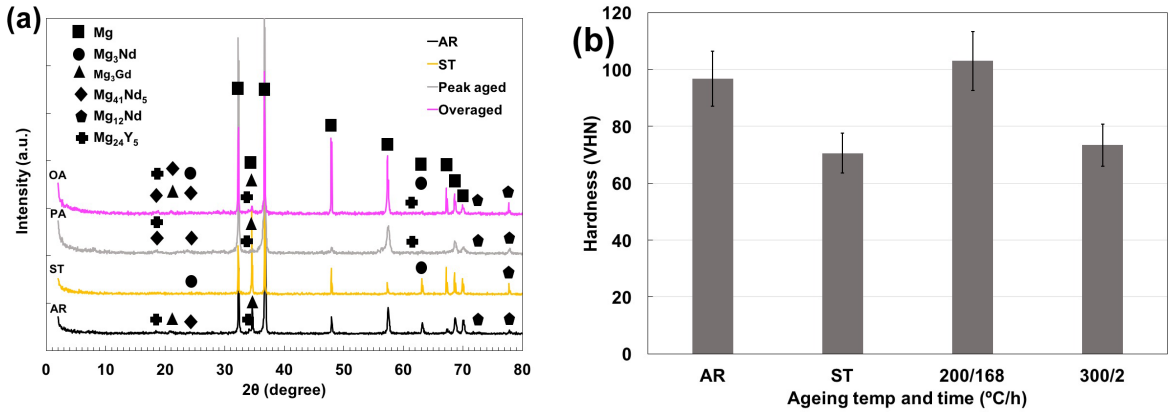

Fig. 3.2 (a) XRD pattern of WE43C in different heat treatment conditions, **(b)** Vickers hardness of WE43C in different heat treatment conditions. AR: as-received, ST: solution treated, 200/168: peak aged (PA), 300/2: overaged (OA).

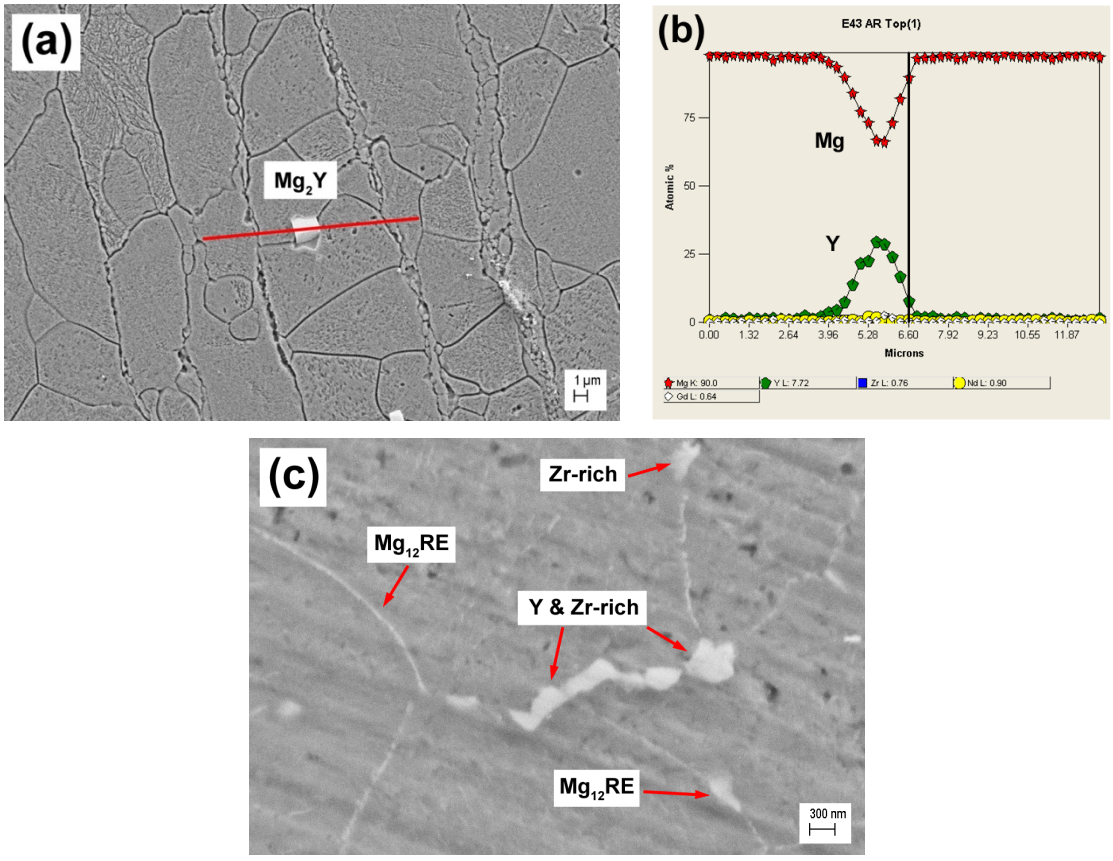

Fig. 3.3 SEM images of the microstructure and energy dispersive X-ray analyses (EDAX) of secondary phase particles by line-scan: **(a)** as-received (AR) sample microstructure after etching, **(b)** elemental concentration profile along the line shown in (a), **(c)** microstructure of AR specimen without etching.

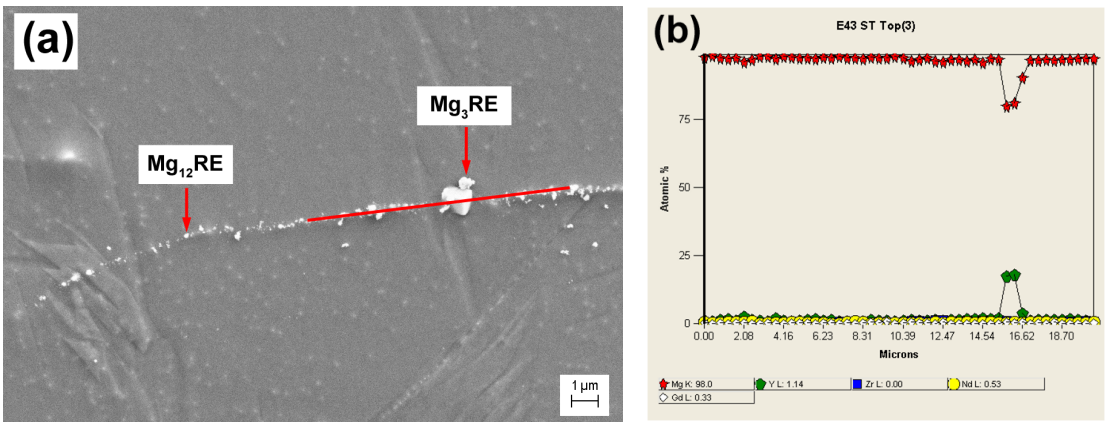

Fig. 3.4 SEM images of the microstructure and energy dispersive X-ray analyses (EDAX) of secondary phase particles by line-scan: **(a)** solution treated (ST) sample microstructure, **(b)** elemental concentration profile along the line shown in (a).

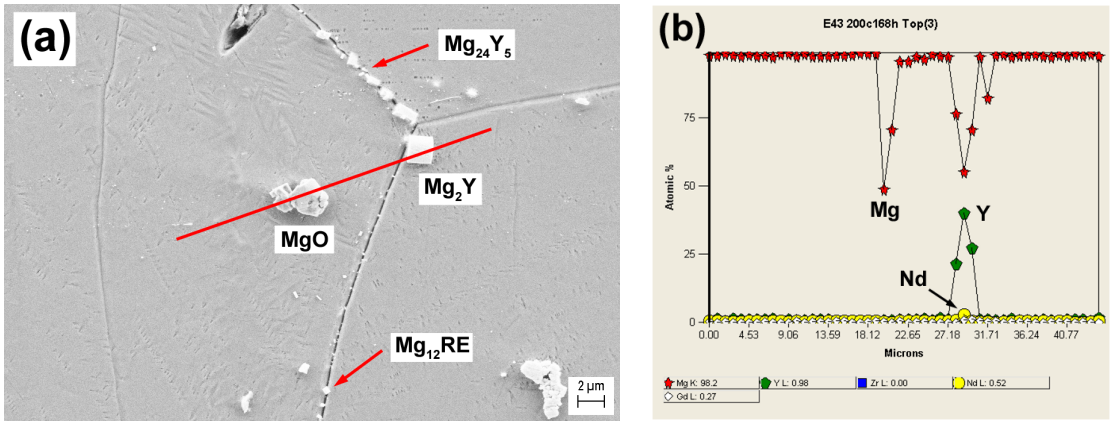

Fig. 3.5 SEM images of the microstructure and energy dispersive X-ray analyses (EDAX) of secondary phase particles by line-scan: **(a)** peak aged (PA) sample microstructure, **(b)** elemental concentration profile along the line shown in (a).

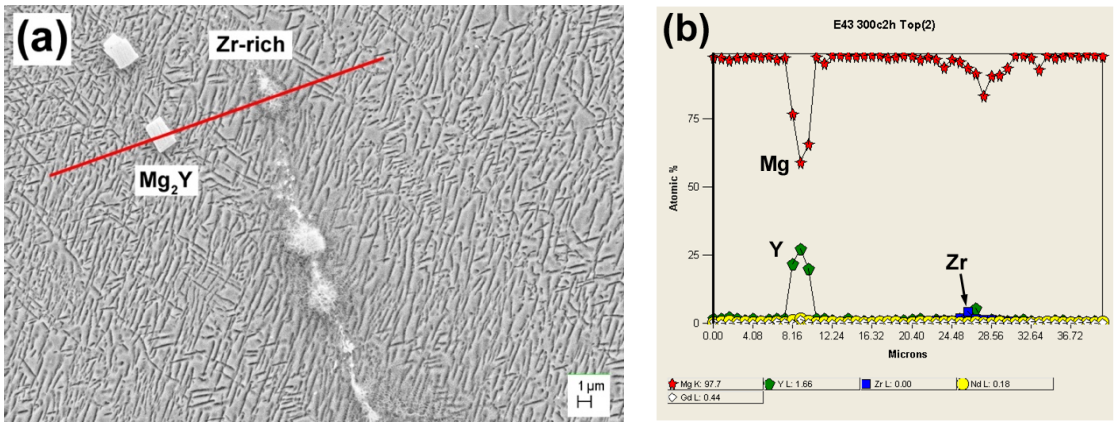

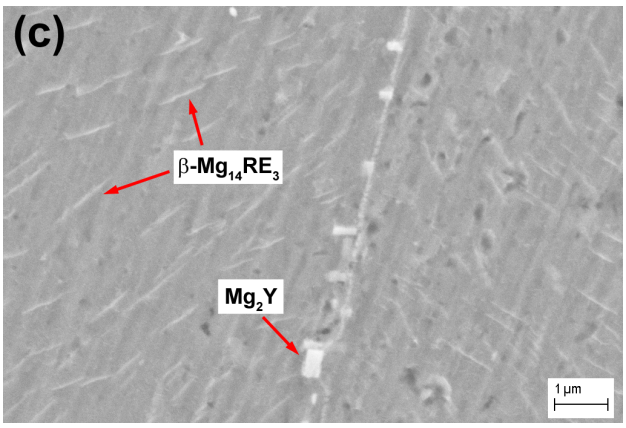

Fig. 3.6 SEM images of the microstructure and energy dispersive X-ray analyses (EDAX) of secondary phase particles by line-scan: **(a)** overaged (OA) sample microstructure after etching, **(b)** elemental concentration profile along the line shown in (a), **(c)** microstructure of OA specimen without etching.

3.3.2 Cyclic Polarization

3.3.2.1 Anodic Polarization

Figure 3.7(a) shows the anodic cyclic polarization plots of the WE43C specimens in four different heat treated conditions in 0.1 M NaOH electrolyte. All the samples showed passivity between OCP and about 1.5 $V_{Ag/AgCl}$ in the 0.1 M NaOH solution. The result of the polarization is summarized in Table 3.1. The overaged specimen showed relatively nobler OCP value and lower passive current density than other heat treated conditions. A transpassive behavior was observed in all the heat treated conditions when the potential increased beyond 1.5 $V_{Ag/AgCl}$. The increase in the current density above the transpassive potential could be attributed to two reactions such as i) breakdown of the corrosion product layer, and ii) oxygen evolution due to the reaction:

$$4OH^- \rightarrow 2H_2O + O_2 + 4e^- \qquad (1)$$

It was observed that the transpassive potential was not a function of heat treatment condition in the 0.1 M NaOH electrolyte. Passivation behavior of magnesium alloys in alkaline environments has been well documented by several investigators [20 – 22]. The passivation behavior of AZ31 alloy in NaOH electrolyte was attributed to the formation of crystalline MgO inner layer and hydrated $Mg(OH)_2$ type outer layer [23].

Periodic fluctuations in the OCP of AZ31 alloy have been reported in the alkaline solutions which was attributed to the breakdown of the protective layer due to stresses induced by hydration of MgO layer followed by repair of the layer. In this investigation, such periodic fluctuations of the OCP of WE43C alloy were not reproducibly observed. Figure 3.7(b) shows

Table 3.1 Cyclic polarization results of WE43C specimens in different heat treated conditions in 0.1 M NaOH.

Concentration of Cl^- in 0.1 M NaOH	Sample	OCP V vs Ag/AgCl	$E_{Transpassive}$ V vs Ag/AgCl	$E_{Cross\ over}$ V vs Ag/AgCl	Passive current density $\mu A/cm^2$
No Cl^-	AR	-1.56	1.57	1.46	7.86
	ST	-1.57	1.60	1.45	6.81
	Peak aged	-1.56	1.61	1.51	10.50
	Overaged	-1.45	1.60	1.52	6.56
80 ppm	AR	-1.54	1.59	1.33	2.67
	ST	-1.56	1.61	1.28	1.78
	Peak aged	-1.52	1.59	1.35	3.97
	Overaged	-1.56	1.57	1.30	2.39
200 ppm	AR	-1.46	1.63	1.32	2.45
	ST	-1.41	1.71	1.58	3.24
	Peak aged	-1.39	1.67	1.52	2.86
	Overaged	-1.42	1.71	1.62	4.11
500 ppm	AR	-1.56	1.52	-1.32	2.11
	ST	-1.49	1.60	1.43	3.49
	Peak aged	-1.55	1.60	1.28	2.19
	Overaged	-1.47	1.59	0.11	5.40
1000 ppm	AR	-1.40	-0.25	-	3.52
	ST	-1.35	0.07	-	2.90
	Peak aged	-1.23	0.11	-	2.69
	Overaged	-1.37	0.08	-	3.40

a typical OCP vs time plot of the overaged specimen in 0.1 M NaOH + 80 ppm Cl^-. The OCP values fluctuated initially (first one hour of exposure to the electrolyte) and stabilized thereafter. The OCP values continued to increase to more positive values and almost reached a plateau value of about -0.5 $V_{Ag/AgCl}$. The nobler OCP value could be associated with thickening of the surface layer. The absence of fluctuations in the OCP profile indicated presence of a more protective layer that could withstand the oxide or hydroxide growth stresses in WE43C. Incorporation of oxides/hydroxides of the rare-earth elements in the MgO layer possibly rendered the surface layer more ductile or healed the cracked surface film faster so that the fluctuations were not noticed. However, this is a speculation only based on the results given in Ref. [17] since there is no direct analytical result based on the current work available to support this hypothesis.

When the potential scan was reversed after a pre-determined transpassive current density (typically 1 mA/cm^2), a hysteresis was observed in all the heat treated conditions even without addition of chloride in the 0.1 M NaOH electrolyte. Such hysteresis could be attributed to the breakdown of the protective layer. No pitting type corrosion is anticipated in the absence of chloride. Dissolution of intermetallic precipitates at the transpassive potentials could have caused the hysteresis. The cross over potential of the reverse scan plot is normally referred to as the pitting protection potential (E_{pp}) and the more positive the E_{pp} value, the better the resistance to localized corrosion. It was observed that the E_{pp} values were similar for all the heat treated conditions.

Figure 3.7(c) shows the cyclic polarization results in 0.1 M NaOH with the addition of 80 ppm Cl^-. The OCP values were similar for all the specimens. The transpassive potentials were not affected by the heat treatment conditions. The peak aged specimen showed the highest passive current density with the addition of 80 ppm Cl^-. The trend is similar to that observed in 0.1 M NaOH without chloride addition. The solution treated specimen showed the lowest passive current density. The results are summarized in Table 3.1.

Figure 3.7(d) shows the anodic portion of the cyclic polarization in 0.1 M NaOH with the addition of 200 ppm Cl^-. Table 3.1 summarizes the polarization results. Comparison of the polarization plots with and without addition of chloride to 0.1 M NaOH indicated that either the transpassive potential or the E_{pp} (cross over potential) did not change significantly. The as-received specimen showed the lowest transpassive and cross over potentials. It was interesting to note that the passive current decreased from about 7 $\mu A/cm^2$ to about 3 $\mu A/cm^2$ upon the addition of up to 200 ppm Cl^- to 0.1 M NaOH. Overall, the passivation behavior of the WE43C alloy specimens was not affected by the addition of up to 200 ppm Cl^- in the 0.1 M NaOH electrolyte.

Figure 3.7(e) shows the polarization behavior in the 0.1 M NaOH electrolyte with the addition of 500 ppm Cl^-. The results are summarized in Table 3.1. The parameters such as OCP, transpassive potential and the passivation current density were found not to be affected by the chloride concentration of 500 ppm for any heat treatment conditions. The overaged specimen showed marginally higher passivation current density than the other specimens. However, the pitting protection potentials were different for the different heat treated conditions as seen in Table 3.1. Both the solution-treated specimen and peak-aged specimen showed much

higher pitting protection potentials of 1.43 and 1.28 $V_{Ag/AgCl}$, respectively. The solution treated specimen did not lose its protectiveness to localized corrosion in 500 ppm Cl^- as compared to its behavior in 0.1 M NaOH without any chloride addition. The E_{pp} value of the peak aged specimen decreased by about 23 mV as compared to that observed in 0.1 M NaOH without Cl^- addition. On the other hand, the as-received and overaged specimens showed considerably lower pitting protection potentials of -1.32 and 0.11 $V_{Ag/AgCl}$ in 500 ppm Cl^- containing 0.1 M NaOH electrolyte.

Figure 3.7(f) shows cyclic polarization of WE43C in 0.1 M NaOH with the addition of 1000 ppm Cl^-. The values are shown in Table 3.1. The OCP of all samples moved up to positive direction compared to those in 500 ppm Cl^-. However, the transpassive potential decreased considerably as compared to the values observed in 500 ppm Cl^- solution. The transpassivity occurred closer to 0 $V_{Ag/AgCl}$. Moreover, there were no measurable pitting protection potentials in all heat treatment conditions, as the reverse scan cross over potential was more cathodic than the OCP. These results imply that the passive film of WE43C cannot repassivate in 1000 ppm Cl^- when the pits initiate.

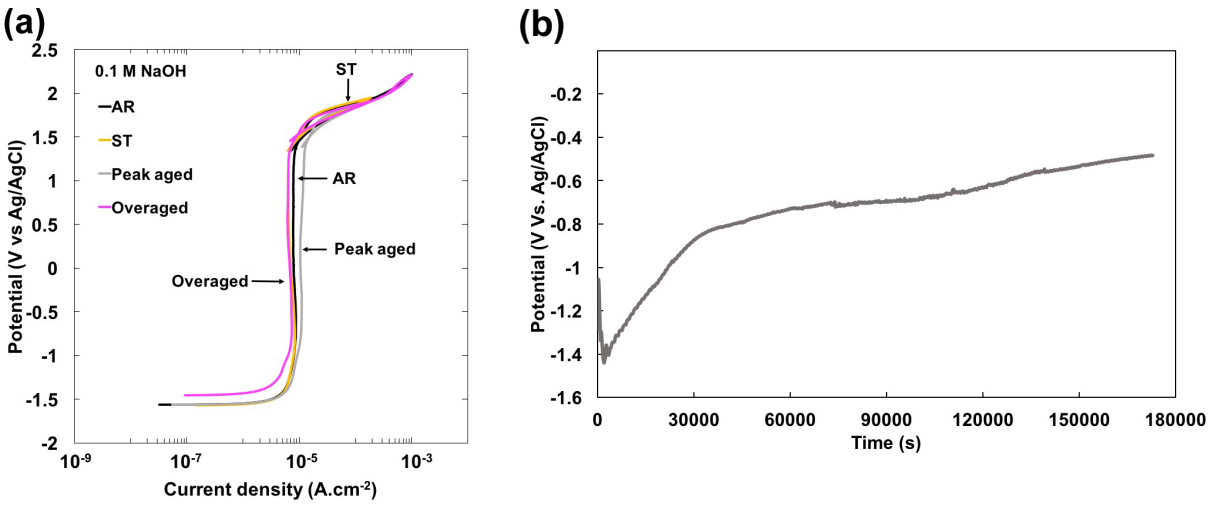

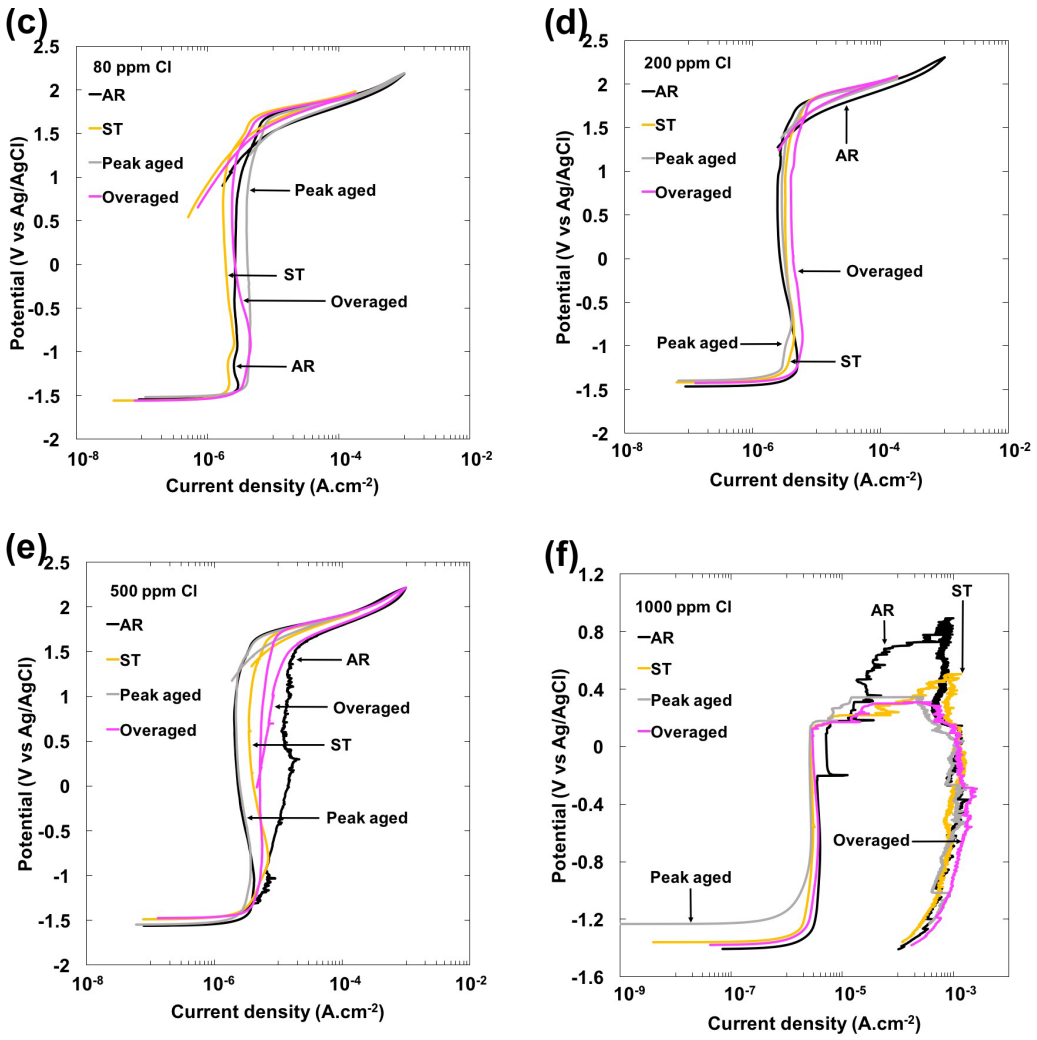

Fig. 3.7 Cyclic polarization results of WE43C in different heat treated conditions in 0.1 M NaOH with additional chloride concentrations: **(a)** no Cl^-, **(b)** OCP of overaged specimen in 80 ppm Cl^-, **(c)** 80 ppm Cl^-, **(d)** 200 ppm Cl^-, **(e)** 500 ppm Cl^-, **(f)** 1000 ppm Cl^-.

3.3.2.2 Cathodic Polarization

Figure 3.8(a) – (d) shows the cathodic polarization of the WE43C specimens in 0.1 M NaOH electrolyte with 0 – 200 ppm Cl^- additions. The results are summarized in Table 3.2 in terms of Tafel slope (β), exchange current density for hydrogen evolution reaction (i_0), and overpotential (η) at 1 mA/cm^2. A quick examination of the cathodic polarization plots in different chloride concentrations indicated that the as-received specimens showed the lowest activity and the overaged specimens showed the highest activity for cathodic reactions. The cathodic Tafel slopes were in the range of -0.18 to -0.26 V/decade. The slopes were relatively shallower than reported for WE43 or Mg-Y binary alloys in lower pH electrolytes. For

example, Marcus and coworkers [17] reported a value of 341 mV/decade in 0.1 M Na_2SO_4 electrolyte for the WE43 alloy (heat treatment condition was not specified). Atrens and coworkers [2] reported a cathodic Tafel slope in the range of 0.429 – 0.517 V/decade for the Mg-Y binary alloys in 0.1 M NaCl. On the other hand, Chu and Marquis [24] reported a Tafel slope of -256 mV for the solution treated WE43 and -232 mV for the T5 aged WE43 alloy in $Mg(OH)_2$ saturated 3.5 wt% NaCl solution (pH 10.5). Therefore, the lower Tafel slope of the WE43 specimens could be associated with higher pH electrolytes. The hydrogen evolution reaction (HER) on the WE43C alloy surface could occur in successive steps of adsorption and desorption of hydrogen atom given by the Volmer-Heyrovsky-Tafel mechanism [25]:

$$M + H_2O + e^- \rightarrow MH + OH^- \quad \text{(Volmer)} \quad (2)$$

$$MH + H_2O + e^- \rightarrow M + OH^- + H_2 \uparrow \quad \text{(Heyrovsky)} \quad (3)$$

$$MH + MH \rightarrow 2M + H_2 \uparrow \quad \text{(Tafel)} \quad (4)$$

Here M represents the metal adsorption site for hydrogen. The Tafel slopes of the Volmer, Heyrovsky, and Tafel reactions are generally established as 118, 39, and 29.5 mV/decade, respectively [26]. The Tafel slope is given as [26]

$$\beta = (2.303RT)/(\alpha nF) \quad (5)$$

where R = universal gas constant, T = temperature, α = transfer co-efficient, n = No. of electrons involved in the reaction, and F = Faraday's constant.

The Tafel slope depends on the rate determining step of the HER, the potential dependent surface coverage of the adsorbed intermediates, surface roughness, and catalytic activity of the surface atoms. Since the calculated Tafel slopes of this investigation were in the range of -0.18 to -0.26 V/decade, the rate determining step of the HER could be the Volmer reaction (2) and given as

$$2H_2O + 2e^- \rightarrow H_2 \uparrow + 2OH^- \quad (6)$$

The hydroxyl ions will be adsorbed on the specimen surface leading to formation of $Mg(OH)_2$ and $RE(OH)_3$ type layers. Recently Salleh et al. [27] reported enhanced hydrogen evolution on $Mg(OH)_2$ covered Mg surface, and Dai et al. [28] prepared nano $Mg(OH)_2$ supported on a graphene layer as hydrogen evolution catalyst for microbial electrolysis cell. Fajardo and Frankel [29] reported Tafel slopes for cathodic reaction on high purity Mg and ultra high purity Mg to be -0.28 and -0.23 V/decade in 0.1 M NaCl (pH ~6.0).

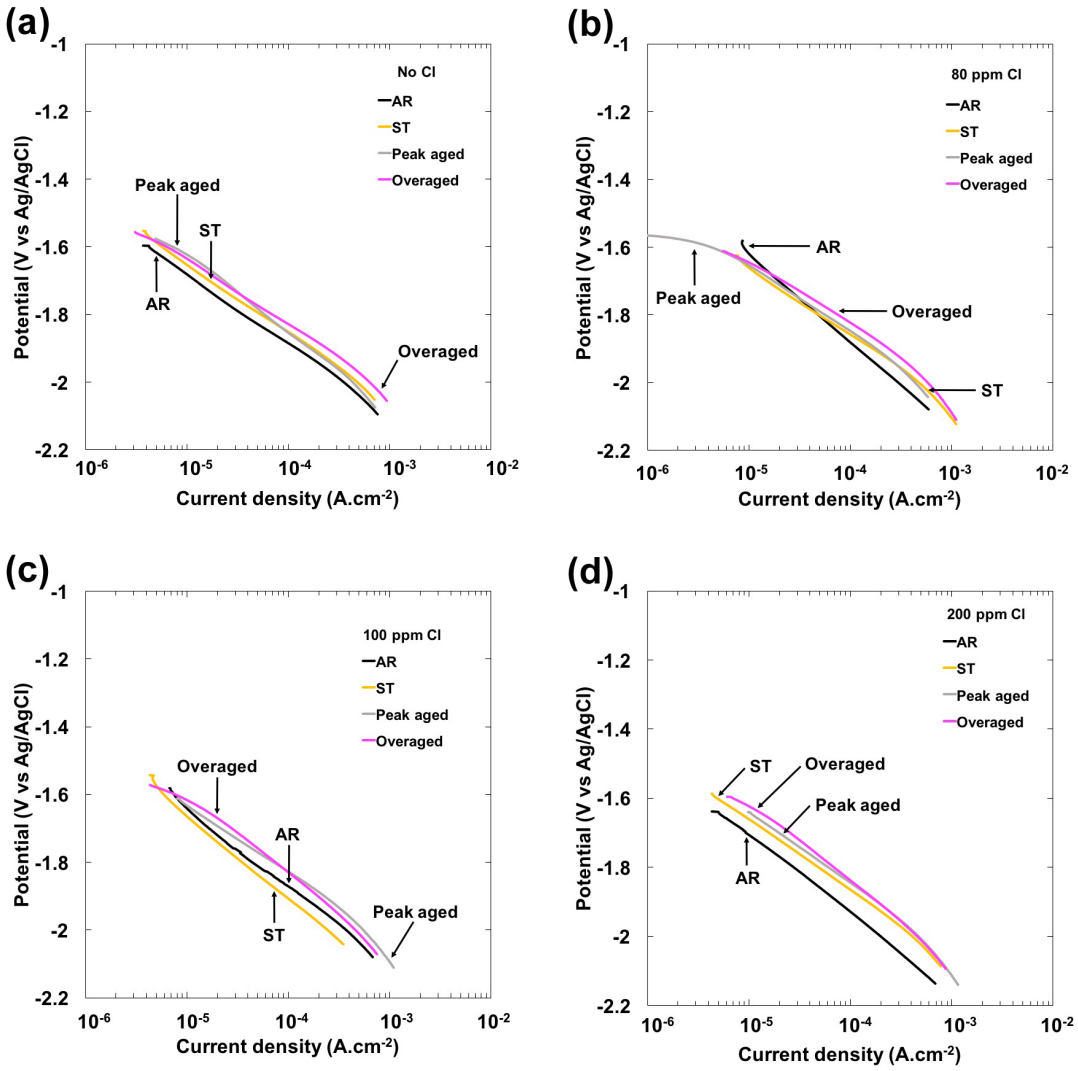

Fig. 3.8 Cathodic polarization of WE43C in different heat treatment conditions in 0.1 M NaOH with different chloride concentrations: **(a)** no Cl^-, **(b)** 80 ppm Cl^-, **(c)** 100 ppm Cl^-, **(d)** 200 ppm Cl^-.

The reported exchange current densities (i_0) for the HER were 4×10^{-8} A/cm^2 and 8×10^{-9} A/cm^2 for the high purity Mg (Fe: 40 ppm) and ultra high purity Mg (Fe: 0.1 ppm), respectively. The exchange current densities of WE43C alloy specimens also fall within the range reported for pure magnesium. Overall, the as-received specimen showed relatively steeper cathodic Tafel slopes and the overaged specimen showed shallower cathodic Tafel slopes than other heat-treated conditions. The as-received specimen had a finer grain size and possibly high dislocation density. If the grain boundaries and dislocations were short circuit paths for the diffusion of atoms, the adsorbed hydrogen could easily diffuse through these routes inside the material and therefore hydrogen evolution reaction would be slowed down resulting

in a steeper Tafel slope. Such grain boundary diffusion of hydrogen may result in the formation of hydride (MgH_2) phase. The binding energy of [H] or hydrogen chemisorption energy (ΔE_H) plays an important role in determining the formation of hydride phase vs hydrogen evolution. Too negative a ΔE_H will lead to lower i_0 due to lack of less number of available sites for [H] + [H] recombination and stronger *M*-H bonds. Too positive values of ΔE_H also will decrease the i_0 because [H] becomes unstable on the electrode surface [30]. The *M*-H bond strength depends on the phases present on the specimens. The overaged specimen had incoherent intermetallic precipitates that were reportedly cathodic to the matrix [3]. The lower cathodic Tafel slopes could be attributed to the distribution of such cathodic intermetallic phases. The relatively higher exchange current density observed on the overaged specimen could also be attributed to the presence of incoherent precipitates that were cathodic in nature.

Table 3.2 Summary of the cathodic polarization results of WE43C specimens in different heat treated conditions in 0.1 M NaOH with addition of different chloride concentrations.

Sample	Cl^- concentration	Tafel slope V/dec	Exchange current density for hydrogen evolution, i_0 A/cm^2	Over potential for 1 mA/cm^2
AR	No Cl^-	-0.22	4.5×10^{-9}	-1.10
	80 ppm	-0.26	3.0×10^{-8}	-1.15
	100 ppm	-0.21	2.0×10^{-9}	-1.15
	200 ppm	-0.23	7.5×10^{-9}	-1.18
ST	No Cl^-	-0.21	6.0×10^{-9}	-1.15
	80 ppm	-0.19	3.2×10^{-9}	-1.10
	100 ppm	-0.24	1.3×10^{-8}	-1.18
	200 ppm	-0.21	4.0×10^{-9}	-1.15
Peak aged	No Cl^-	-0.24	2.3×10^{-8}	-1.15
	80 ppm	-0.19	3.2×10^{-9}	-1.20
	100 ppm	-0.19	2.8×10^{-9}	-1.09
	200 ppm	-0.21	5.5×10^{-9}	-1.11
Overaged	No Cl^-	-0.18	2.0×10^{-9}	-1.05
	80 ppm	-0.19	2.1×10^{-9}	-1.08
	100 ppm	-0.23	2.8×10^{-8}	-1.10
	200 ppm	-0.23	1.8×10^{-8}	-1.10

3.3.3 Potentiostatic Passivation

Figure 3.9(a) – (d) shows the *I-t* (current-time) plots in log-log scale recorded during potentiostatic passivation of the specimens in different chloride concentrations (0, 100, 200, and 1000 ppm) in 0.1 M NaOH electrolyte. The applied potential was in the middle of the passivation range of the potential window. The samples in different heat treated conditions essentially showed a current decay behavior in the NaOH solution without addition of chloride. After initial current decay, an increase in the current density was observed in the solutions containing chloride. The length of current decay behavior was a function of chloride concentration. The current decay was observed, in general, for more than 700 s for 100 ppm Cl^- which decreased to about 400 s for 200 ppm Cl^-, and less than 200 s for 1000 ppm Cl^-. The current decay behavior can be expressed using an empirical relation

$$I = I_0 t^{-\alpha} \qquad (7)$$

where I = passive current density at time "t"; I_0 = initial current density recorded on a "bare" alloy surface; t = time; and α = passivation kinetic exponent.

The steeper the slope of the log I-log t plot, the faster is the passivation kinetics. Therefore, the magnitude of the passivation kinetic exponent, α is an indication of the ability of the material to passivate. The values of α derived from Fig. 3.9(a) – (d) are summarized in Table 3.3. As seen, the as-received (AR) specimens showed larger values of passivation kinetic exponent than other heat-treated conditions. Furthermore, the exponent value decreased as the chloride concentration increased in case of the AR specimen. However, no such trend could be observed for other heat treated conditions. In fact, the exponent value increased with chloride concentration for the solution treated specimen until 200 ppm and decreased when the concentration was 1000 ppm. The current decay during initial period followed by increase in the current and decay at the end of 1-h passivation could be ascribed as passivation-breakdown-and-repair behavior of the passive layer. As observed from the log I-log t plots, the initial current decay duration could be considered as the incubation time for passivity breakdown. Localized rupture of passive film could increase in the current density. However, the passive film healed quickly and the current density decayed by continuous application of potential.

The specimens appeared to start re-passivating when the current density reached a "threshold" value in the range of 5 – 15 $\mu A/cm^2$, depending on the chloride concentration and the heat treatment condition. The increase in the current density in the 0.1 M NaOH solution

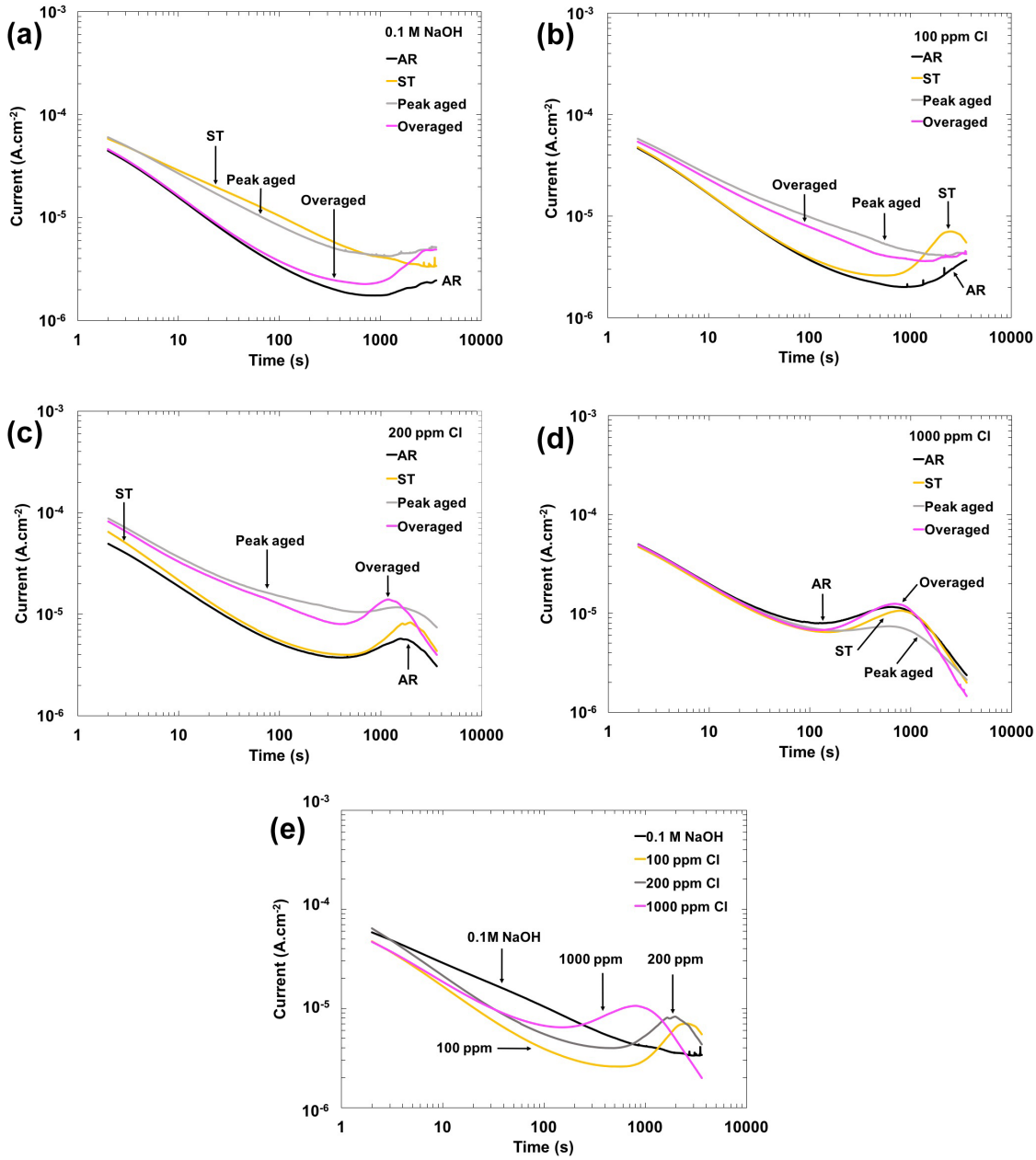

Fig. 3.9 *I-t* plots of WE43C in different heat treatment conditions under potentiostatic control in 0.1 M NaOH solution with different concentrations of chloride: **(a)** no Cl^-, **(b)** 100 ppm Cl^-, **(c)** 200 ppm Cl^-, **(d)** 1000 ppm Cl^-, **(e)** solution treated specimen in different chloride concentrations. The applied potential was in the middle range of passivation region from cyclic polarization results in Fig. 3.7.

without chloride addition could be associated with the growth stresses of thicker oxide layer that caused breakdown possibly due to conversion of MgO and RE_2O_3 to $Mg(OH)_2$ and $RE(OH)_3$, as proposed by Taheri and Kish [23]. In this case, current decay behavior at the end was not observed within 1 h of passivation because the "critical" current density for initiating the re-passivation was not reached or the test ended before reaching the critical current density.

The critical current density for re-passivation was observed to be a function of heat treated condition and the chloride concentration as well from Fig. 3.9(a) – (d). It could be a function of applied potential as well, but experiments were not carried out at different potentials to show such effect.

The overaged specimen required higher critical density for re-passivation, in general. The AR specimen required lower critical current density in low chloride concentrations. When the chloride concentration was 1000 ppm, the critical current density for inducing re-passivation was independent of the heat treatment condition as seen in Fig. 3.9(d), even though the peak aged specimen showed the lowest critical current density.

Figure 3.9(e) shows the *I-t* plots in log scale of solution treated specimen in different chloride concentrations. From this figure, it could be insisted that the influence of chloride affected both incubation time for passivity breakdown and critical current density for re-passivation. The lower chloride concentration, the longer was the incubation time and the lower was the critical current density for re-passivation.

Table 3.3 Passivation kinetic exponent and charge carrier density of WE43C specimens in 0.1 M NaOH with addition of different chloride concentrations.

Sample	Cl^- concentration	Passivation kinetic exponent, α	Charge carrier density, N_D ($1/cm^3$)
AR	No Cl^-	0.727	2.45×10^{21}
	80 ppm	0.668	5.96×10^{21}
	200 ppm	0.647	3.37×10^{21}
	1000 ppm	0.526	2.91×10^{21}
ST	No Cl^-	0.450	2.09×10^{21}
	80 ppm	0.621	4.67×10^{21}
	200 ppm	0.704	5.43×10^{21}
	1000 ppm	0.588	2.78×10^{21}
Peak aged	No Cl^-	0.516	3.91×10^{21}
	80 ppm	0.588	5.09×10^{21}
	200 ppm	0.426	7.10×10^{21}
	1000 ppm	0.500	3.16×10^{21}
Overaged	No Cl^-	0.678	3.65×10^{21}
	80 ppm	0.416	6.01×10^{21}
	200 ppm	0.434	5.33×10^{21}
	1000 ppm	0.525	2.59×10^{21}

3.3.4 Electrochemical Impedance Spectroscopy

Figure 3.10(a) – (d) shows the Nyquist plots recorded at the passivation potentials after 1 h of potentiostatic passivation in different chloride concentrations that was described in the previous section. The impedance behaviors in 0.1 M NaOH indicated that the solution treated specimen showed the highest impedance profile and the overaged specimen had the lowest impedance profile as seen in Fig. 3.10(a). In the 100 ppm Cl^- containing solution, the solution treated specimen showed the lowest impedance profile and other heat treated conditions revealed similar impedance behaviors, as seen in Fig. 3.10(b). The passive film formed on the peak aged specimen in 200 ppm Cl^- solution showed the lowest impedance profile as seen in Fig. 3.10(c).

The passive film formed on the AR specimen in 200 ppm Cl^- had the highest impedance profile among all the heat treated conditions. Whereas in 1000 ppm Cl^-, the trend completely reversed as the lowest impedance profile was observed for the AR specimen. The EIS behavior could be modeled using an equivalent electrical circuit. The EIS data collected after potentiostatic passivation of the specimens were fitted with different combinations of electrical equivalent circuits that could model the dual layered surface layer of the magnesium alloys proposed by other investigators [31, 32]. Based on the goodness of fitting, the best fitting equivalent circuit was determined to be the one given in Fig. 3.10(i) that consisted of 2-parallel RC loops connected in series. The resistor R_s represents the solution resistance, R_1 and Q_1 are associated with resistance and capacitance behavior of the inner layer. Table 3.4 summarizes the values of the equivalent circuit elements. Here Q_1 and Q_2 are leaky capacitors with distributed time constants due to surface heterogeneity. Figure 3.10(e) – (h) shows some examples of the calculated Nyquist plots using the equivalent circuit model values (given in Table 3.4) in comparison with the experimentally measured impedance plots.

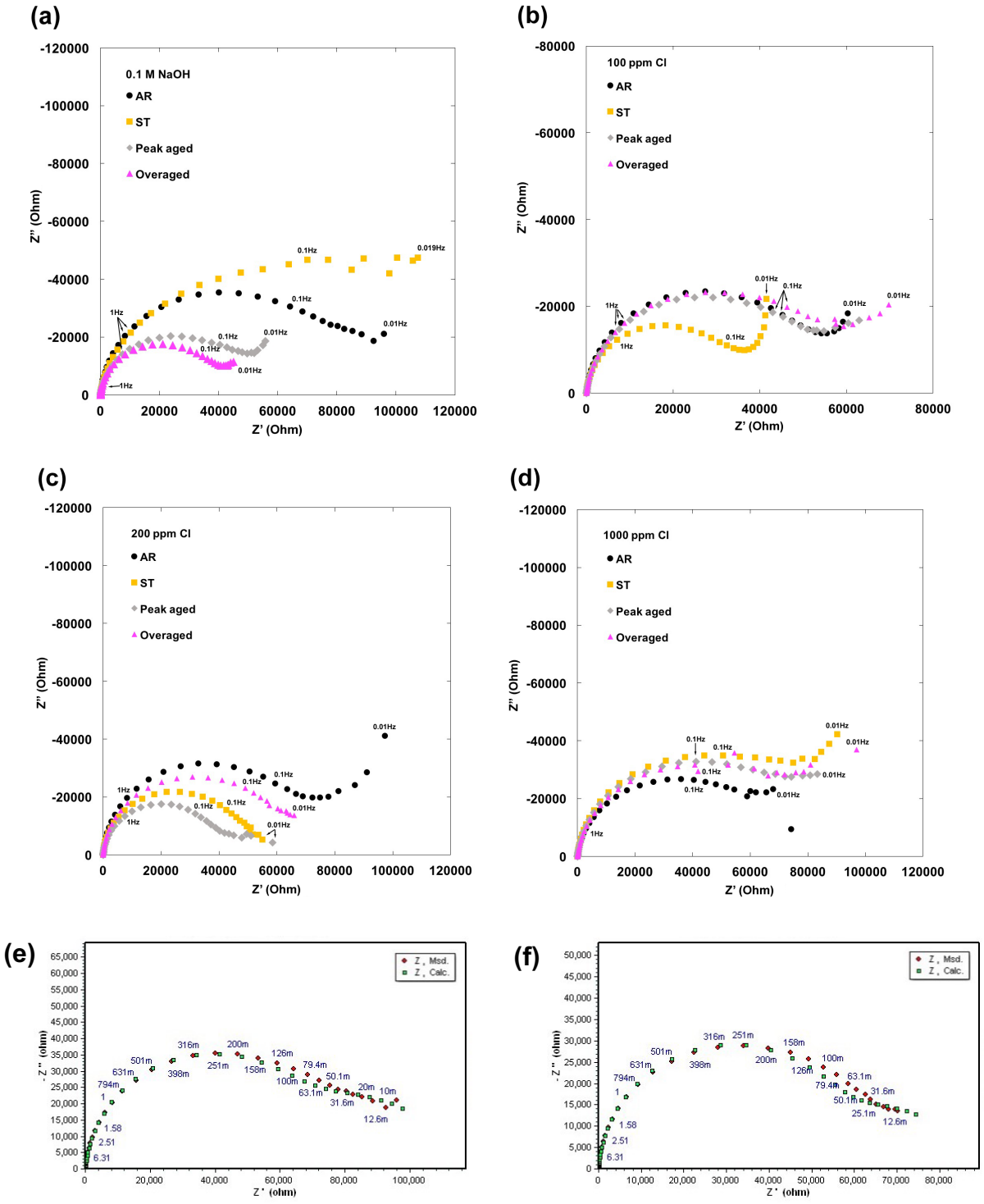
(a)
0.1 M NaOH
AR
ST
Peak aged
Overaged
Z'' (Ohm)
Z' (Ohm)
(b)
100 ppm Cl
AR
ST
Peak aged
Overaged
Z'' (Ohm)
Z' (Ohm)
(c)
200 ppm Cl
AR
ST
Peak aged
Overaged
Z'' (Ohm)
Z' (Ohm)
(d)
1000 ppm Cl
AR
ST
Peak aged
Overaged
Z'' (Ohm)
Z' (Ohm)
(e)
Z , Msd.
Z , Calc.
- Z'' (ohm)
Z' (ohm)
(f)
Z , Msd.
Z , Calc.
- Z'' (ohm)
Z' (ohm)

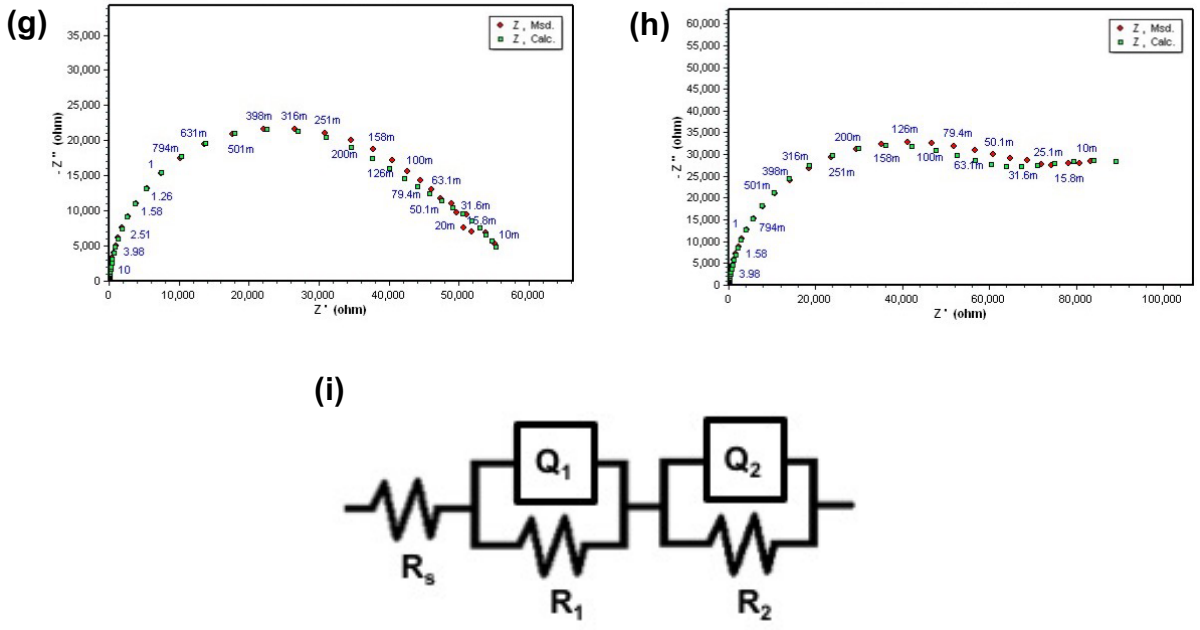

Fig. 3.10 Nyquist plots of WE43C passivated in the middle range of passivation region for 1 h in 0.1 M NaOH solution with different concentrations of chloride: **(a)** no Cl^-, **(b)** 100 ppm Cl^-, **(c)** 200 ppm Cl^-, **(d)** 1000 ppm Cl^-. Comparison of the measured Nyquist plots with the calculated ones using the equivalent circuit shown in (i) are shown in (e) – (h): **(e)** Nyquist plot of as-received in 0.1 M NaOH, **(f)** Nyquist plot of solution treated in 100 ppm Cl^-, **(g)** Nyquist plot of solution treated in 200 ppm Cl^-, **(h)** Nyquist plot of peak aged in 1000 ppm Cl^-. Note: Msd denotes measured data points and Calc. denoted calculated data points with the equivalent circuit model. **(i)** Electrical equivalent circuit fitted the data of Nyquist plots.

The R_s values remained almost a constant in spite of different chloride concentrations. The capacitance behavior of the surface layer was represented as constant phase elements, whose impedance can be expressed as

$$Z = 1/(j\cdot\omega)^{\alpha}Q_1 \qquad (8)$$

where Z = impedance, ω = angle frequency, $j = \sqrt{-1}$, Q_1 = admittance due to the capacitor behavior, α = parameter describing the leaky capacitor behavior, $\alpha = 1$ for an ideal capacitor with single time constant, and $\alpha < 1$ when the system behaves like a leaky capacitor with distributed time constants.

The better passivation behavior could be associated with high charge transfer resistance or high impedance. Therefore, higher resistance values of R_1 and R_2 would render the passive films more protective. Based on the relation (8), lower values of admittance for Q_1 and Q_2 would make the surface layers more protective.

Table 3.4 The equivalent circuit values of the specimens in different chloride concentrations.

Sample	Cl^- concentration (ppm)	R_s (Ohm)	Q_1 ($S \cdot s^{\alpha}$)	α	Q_2 ($S \cdot s^{\beta}$)	β	R_1 (Ohm)	R_2 (Ohm)	Goodness of Fitting
AR	0	60.32	8.023×10^{-6}	0.955	1.215×10^{-4}	0.7983	6.612×10^{4}	4.786×10^{4}	4×10^{-4}
	80	57.08	2.243×10^{-4}	0.8211	1.099×10^{-5}	0.9607	7.544×10^{4}	5.227×10^{4}	5×10^{-4}
	200	60.11	1.759×10^{-4}	0.8437	7.859×10^{-6}	0.9581	6.964×10^{4}	6.384×10^{4}	8×10^{-4}
	1000	45.44	1.099×10^{-5}	0.7965	1.667×10^{-5}	0.9442	4.619×10^{4}	4.218×10^{4}	9×10^{-4}
ST	0	44.7	7.076×10^{-6}	0.926	7.872×10^{-6}	0.9098	12.8×10^{4}	7.512×10^{4}	4.8×10^{-3}
	80	49.74	2.082×10^{-4}	0.8402	9.534×10^{-6}	0.9563	3.747×10^{4}	3.923×10^{4}	1.7×10^{-3}
	200	52.76	9.554×10^{-6}	0.9658	1.82×10^{-4}	0.8379	4.094×10^{4}	1.65×10^{4}	2×10^{-4}
	1000	47.57	1.385×10^{-5}	0.8	1.56×10^{-4}	0.8	65.6×10^{4}	1.205×10^{5}	5×10^{-4}
Peak aged	0	55.96	2.766×10^{-4}	0.8	1.053×10^{-5}	0.8	40.29×10^{4}	4.235×10^{4}	8×10^{-4}
	80	57.58	2.647×10^{-4}	0.8	9.321×10^{-6}	0.8	29.25×10^{4}	5.739×10^{4}	3×10^{-4}
	200	57.21	1.035×10^{-5}	0.9608	1.845×10^{-4}	0.8563	3.383×10^{4}	1.889×10^{4}	1.1×10^{-3}
	1000	50.2	1.739×10^{-4}	0.836	1.43×10^{-5}	0.9352	64.11×10^{4}	6.013×10^{4}	4×10^{-4}
Overaged	0	51.8	3.926×10^{-4}	0.7835	9.51×10^{-6}	0.9508	0.3273×10^{4}	3.677×10^{4}	6×10^{-4}
	80	51.82	1.035×10^{-5}	0.9637	1.864×10^{-4}	0.8165	3.081×10^{4}	1.399×10^{6}	3×10^{-4}
	200	52.22	2.729×10^{-4}	0.8023	1.04×10^{-5}	0.9552	32.45×10^{4}	5.384×10^{4}	4×10^{-4}
	1000	56.36	1.341×10^{-4}	0.8189	1.504×10^{-5}	0.9272	75.84×10^{4}	5.645×10^{4}	8×10^{-4}

From Table 3.4, it can be noticed that both the inner and outer layers of the surface film showed high resistance values in the order of 30 – 750 kΩ·cm^2. The as-received specimens showed almost similar R_1 and R_2 values, whereas the peak aged specimens showed higher R_1 values. This could possibly be attributed to the higher RE incorporation in the outer layer of the surface film because of distribution of finer coherent precipitates in the alloy matrix. Similarly, the overaged specimen also showed higher R_1 values. On the other hand, the Q_1 values of the peak aged and overaged specimens were higher than their Q_2 values, as well as the Q_1 values of AR and ST specimens, in general.

The results of the Mott-Schottky plots are summarized in Table 3.3. Typical Mott-Schottky plots of peak aged sample in different chloride concentration solutions are shown in Fig. 3.11. The positive slope of the Mott-Schottky profile indicated that the surface film behaved like an *n*-type semiconductor. Therefore, the predominant charge carriers in the film could be oxygen vacancies or metal cation interstitials. The charge carrier densities were determined from the slope and reported to be in the range of 2 – 7 × 10^{21} cm^{-3}, based on the exposed geometric area. There was no clear trend in the variations of the charge carrier density as a function of chloride concentrations or heat treatment conditions could be observed. Therefore, the role of secondary phase precipitates on the impedance behavior of the surface film could not be determined.

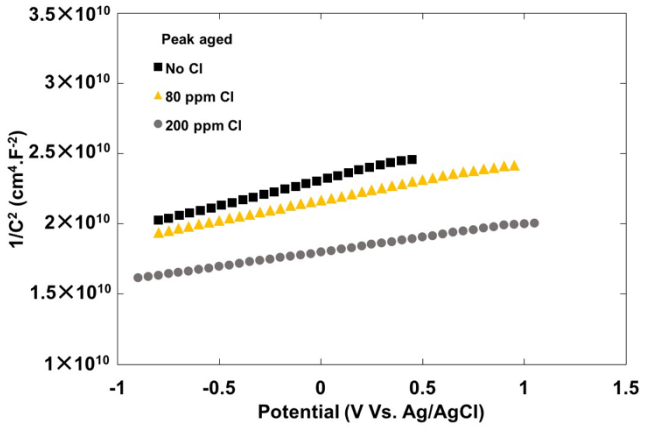

Fig. 3.11 Mott-Schottky plots of peak aged samples (200 °C, 168 h) in different chloride concentrations.

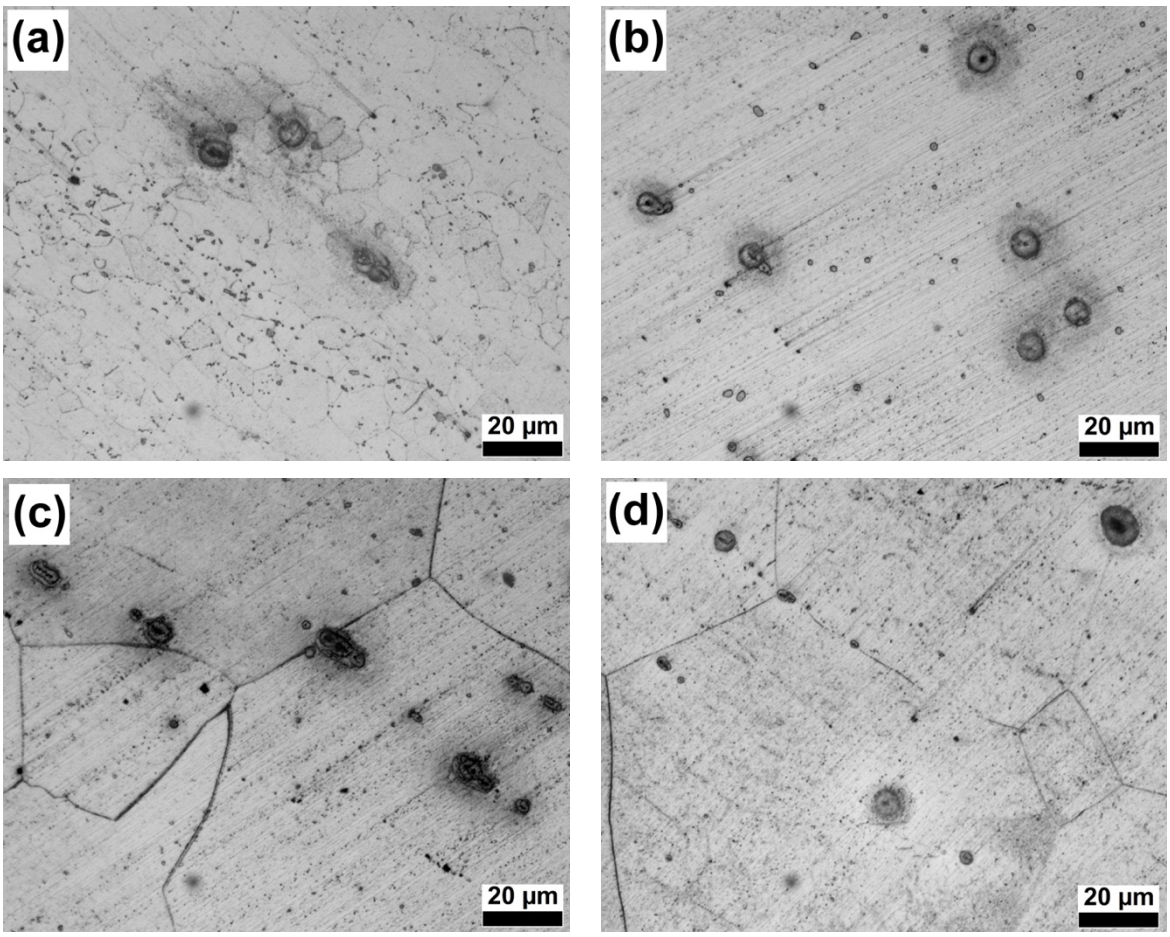

Fig. 3.12 Optical microstructures of WE43C specimens under potentiostatic condition (1.5 $V_{Ag/AgCl}$) until pit initiated in 0.1 M NaOH with 500 ppm Cl^-: **(a)** as-received, **(b)** solution treated, **(c)** peak aged (200 °C, 168 h), **(d)** overaged (300 °C, 2 h).

3.3.5 Pit Initiation

Figure 3.12 shows microstructure of the samples where the pit initiated under potentiostatic condition (1.5 $V_{Ag/AgCl}$) in 0.1 M NaOH with 500 ppm Cl^-. From Fig. 3.12(a) – (d), it can be observed that the pits predominantly initiated at the spherical particles which were identified to be enriched with Zr. Pits initiated at Zr-rich particles because they acted as the cathodic sites which has high volta potential difference with Mg matrix [33]. Figure 3.13(a) shows the microstructure of the sample before exposure to the electrochemical test environment, where the intermetallic particles are intact. The attack on the spherical Zr particles in the form of small pits could be observed from Fig. 3.13(b) after the potentiostatic testing. Figure 3.13(c) shows the EDAX results of the Zr-rich particles. However, the rectangular particles (which are Y-rich particles as identified by the EDAX results in Fig. 3.13(d)) were not susceptible to localized corrosion. The Y-rich particles were still in the same

condition after the experiment. The irregularly shaped secondary phase particles of the peak aged sample as seen in Fig. 3.12(c) and Fig. 3.13(e) were also subjected to localized corrosion. From the EDAX analysis, these particles were identified as Zr-rich phase, as seen in Fig. 3.13(f). The Zr-rich particles typically contain about 45 wt% Zr, 50 wt% Mg, and balance other alloying elements.

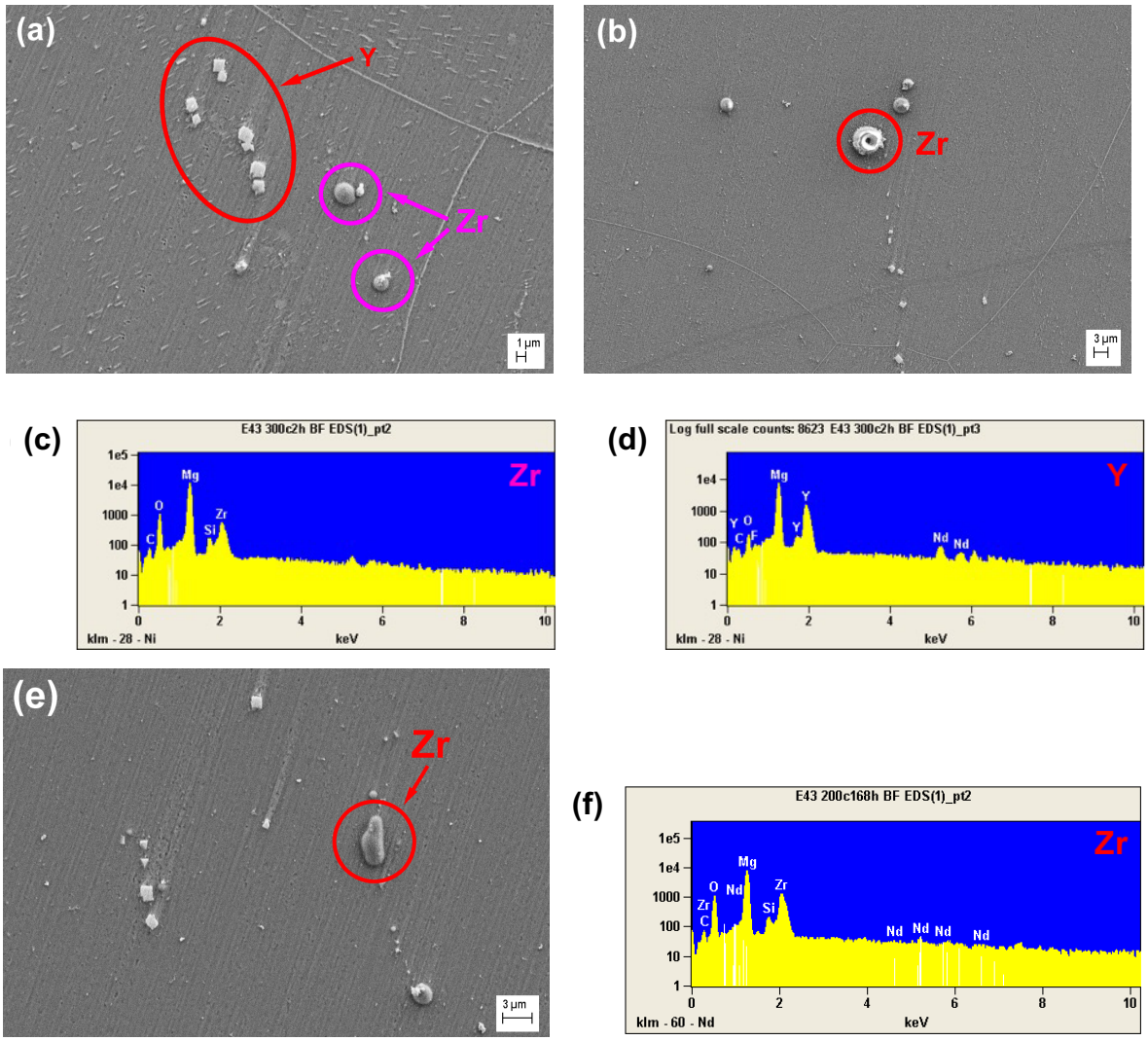

Fig. 3.13 SEM images of WE43C in overaged condition (a and b), and in peak aged condition (e) under potentiostatic condition (1.5 $V_{Ag/AgCl}$) until pit initiated in 0.1 M NaOH with 500 ppm Cl^-: **(a)** before the test, **(b)** after the test, **(c)** EDAX spectrum of spherical particles in (a), **(d)** EDAX spectrum of rectangular particles in (a), **(e)** before the test, **(f)** EDAX spectrum of particles in (e). It should be noted that the images do not show the exact same area.

From the morphology of attack as seen in Fig. 3.12(a) – (d) and 3.13(b), it is assumed that the Zr-rich particles show a core-shell type morphology with Mg core and Zr shell. Since the redox potential of Zr^{4+}/Zr is nobler than that of Mg^{2+}/Mg (-1.539 V_{SHE} vs -2.363 V_{SHE}), the

Zr shell acts as cathode to Mg core, and therefore the core is preferentially dissolved as seen in Fig. 3.13(b). In case of Y-rich particles, the difference between the redox potentials of Y^{3+}/Y and Mg^{2+}/Mg is not significant (-2.372 vs -2.363 V_{SHE}). Therefore, there is no galvanic induced dissolution.

3.3.6 Characterization of the Passivated Surface

Post-test analyses of the surface of the specimens after regular cyclic polarization or 1-h potentiostatic passivation did not yield meaningful results using Raman spectroscopy or glancing angle XRD. Therefore, the potentiostatic passivation was extended up to 36 hours to grow a thicker surface film. Figure 3.14(a) shows the glancing angle XRD result of the passivated surface of the WE43C as-received specimen. Similar results were obtained for other heat treated conditions. Peaks corresponding to $Mg(OH)_2$ could be observed along with the Mg solid solution peaks [34]. The XRD pattern did not reveal presence of either oxides or hydroxides of rare earth elements. The Raman spectrum of the as-received sample's surface did not show any definitive peaks as seen in Fig. 3.14(b). However, broader peaks at 130, 326, 649, and 975 cm^{-1} could be noticed. These peaks match with the Raman peaks of Y_2O_3 reported at 130 (F_g), 330 ($F_g + E_g$) by Yu et al. [35], and MgO peaks of 652 (ν_2) and 980 ($\nu_1 + \nu_8$) cm^{-1} as reported by Raman [36]. Figure 3.15(a) and (b) are the Raman spectra of the passivated surfaces of solution treated and peak aged specimens, respectively. Similar Raman spectra were obtained in both the heat treated conditions, indicating that the secondary phase precipitation did not significantly influence the structure of the surface layers. The Raman spectra suggested that the passive layer consisted of MgO and RE_2O_3, where RE represents Y, Nd, and Gd. Raman peaks corresponding to $Mg(OH)_2$ were not observed. The $Mg(OH)_2$ peaks reportedly occur at 280 (E_g), 443 (A_{1g}), 725 (E_g), and 3652 (A_{1g}) [37]. Among the RE_2O_3 possible in this surface layer, Nd_2O_3 has a lower force constant than that of Gd_2O_3 and Y_2O_3 has a higher force constant than that of Gd_2O_3, and therefore the Raman shift of the given vibration mode will be lower for the Nd_2O_3 than the other two oxides [38]. The strongest Raman intensity of the RE_2O_3 was considered to be $F_g + A_g$ mode that occur at 376 cm^{-1} for Y_2O_3, and 360 cm^{-1} for Gd_2O_3, and ~340 cm^{-1} for Nd_2O_3 [35, 38]. The broader peak recorded around 360 cm^{-1} in both the specimens could be attributed to the presence of RE_2O_3 in the surface layer. Incorporation of rare earth in the form of oxides within the surface layer can be further evidenced from the XPS

results as shown in Fig. 3.16(a) – (c). High resolution XPS spectra of Y *3d* of the passivated surface of the solution treated specimen are given before and after Ar-ion sputtering in Fig. 3.16(a) and (b). The sputtering process did not significantly affect the intensity of the *3d* spectrum which indicated that the concentration of yttrium did not vary significantly within the sputtered thickness of the surface layer. A doublet of Y *3d* signal, corresponding to $3d_{3/2}$ and $3d_{5/2}$, is generally reported to occur at about 160 ± 0.5 and 158.3 ± 0.5 eV, respectively that corresponds to Y_2O_3 and $Y(OH)_3$ species [17]. In this study, very clearly resolved Y *3d* doublet was not observed, but the broad peak observed at 158.0 eV and a shoulder at 159.75 eV with the as-received specimen after sputtering could be assigned to the presence of Y^{3+} species in the surface layer. Jamesh et al. also observed single peak of Y *3d* signal at 158.7 eV on the WE43 sample exposed to Ringer's solution, and assigned the peak to the presence of Y_2O_3 [13]. The RE elements were also present in the matrix of the WE43C alloy as solid solution and therefore the surface layer consisted of MgO, $Mg(OH)_2$, and RE_2O_3 phases. The XPS and Raman analyses of the passivated surface indicated that the heat treatment conditions did not significantly affect the composition of the surface film that was grown in 0.1 M NaOH solution.

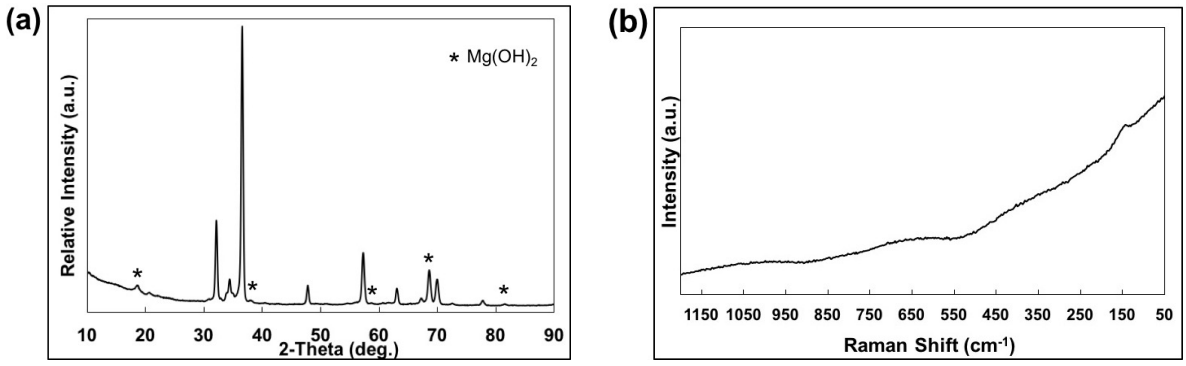

Fig. 3.14 (a) glancing angle XRD pattern of the as-received (AR) specimen after potentiostatic passivation in 0.1 M NaOH solution at 0.5 $V_{Ag/AgCl}$ for 36 h, **(b)** Raman spectrum of the passivated surface of the AR specimen.

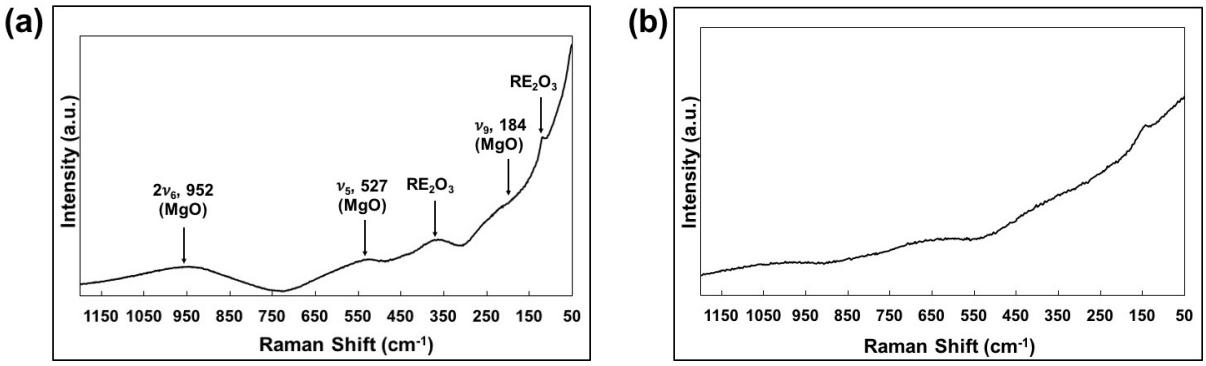

Fig. 3.15 Raman spectra of the potentiostatically passivated WE43C samples in 0.1 M NaOH: **(a)** solution treated sample, **(b)** peak aged sample.

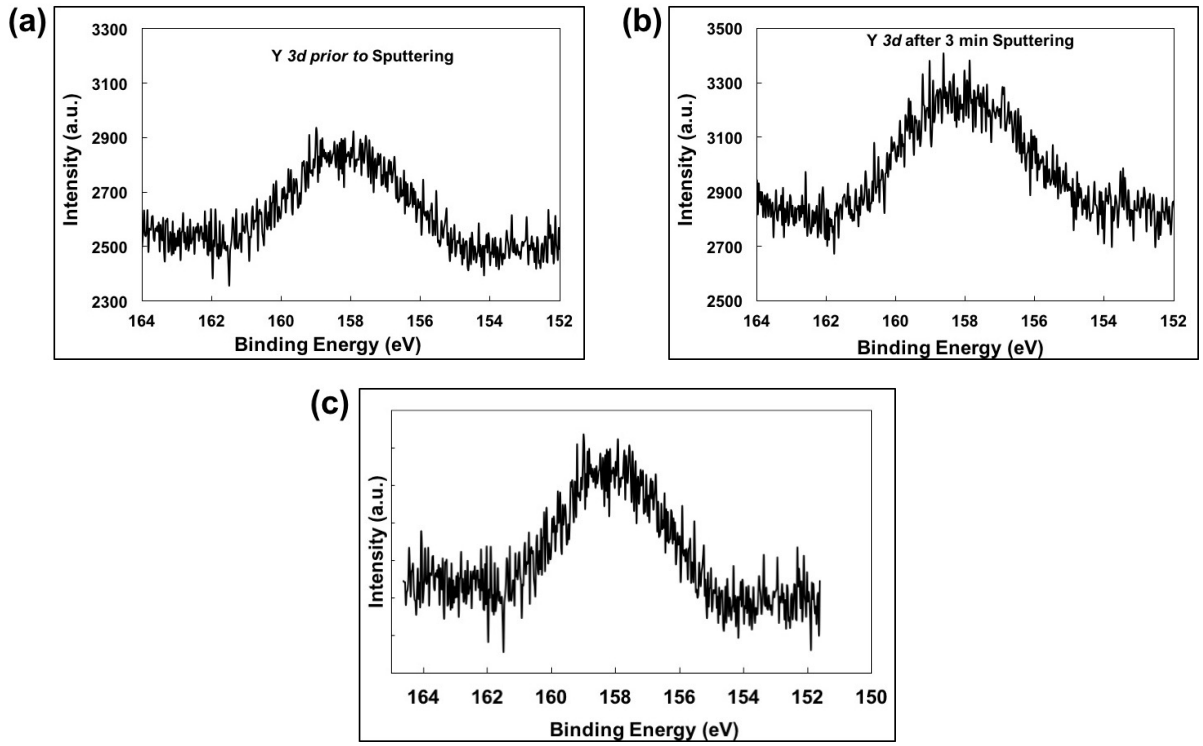

Fig. 3.16 XPS high resolution Y 3*d* spectra of the WE43C specimens potentiostatically passivated in 0.1 M NaOH at 0.5 $V_{Ag/AgCl}$ for 36 h: **(a)** solution treated specimen prior to Ar-ion sputtering (as passivated surface), **(b)** solution treated specimen after sputtering with Ar ion for 3 minutes, **(c)** peak aged specimen without sputtering.

Further analysis of the surface layer was performed using scanning electron microscopy. Figure 3.17(a) – (d) shows the surface morphologies of the passive layer formed on the specimens of four different heat treated conditions after potentiostatic passivation at 0.5 $V_{Ag/AgCl}$ in 0.1 M NaOH for 1 h. The acicular type flake-like structures present in the passive layer indicated that the plate-like morphology of the β′ ($Mg_{12}YNd$) and β ($Mg_{14}RE_3$) phases could have influenced the structure of the film. The solution treated specimen showed lower number

density of the oxide/hydroxide flakes than other heat treatment conditions. Figure 3.18(a) and (b) show the cross sectional view of the passive layer formed on the as-received (AR) and peak aged (PA) specimens, respectively. In order to view the thickness clearly, these specimens were passivated for 36 h in 0.1 M NaOH solution at 0.5 $V_{Ag/AgCl}$. As seen, the as-received condition showed a relatively thicker surface layer (thickness of AR ~1100 nm vs ~580 nm for PA sample) with a more compact bottom layer than that of peak aged condition. The better passivation behavior noted for the AR specimen could be attributed to the thicker and more compact passive layer.

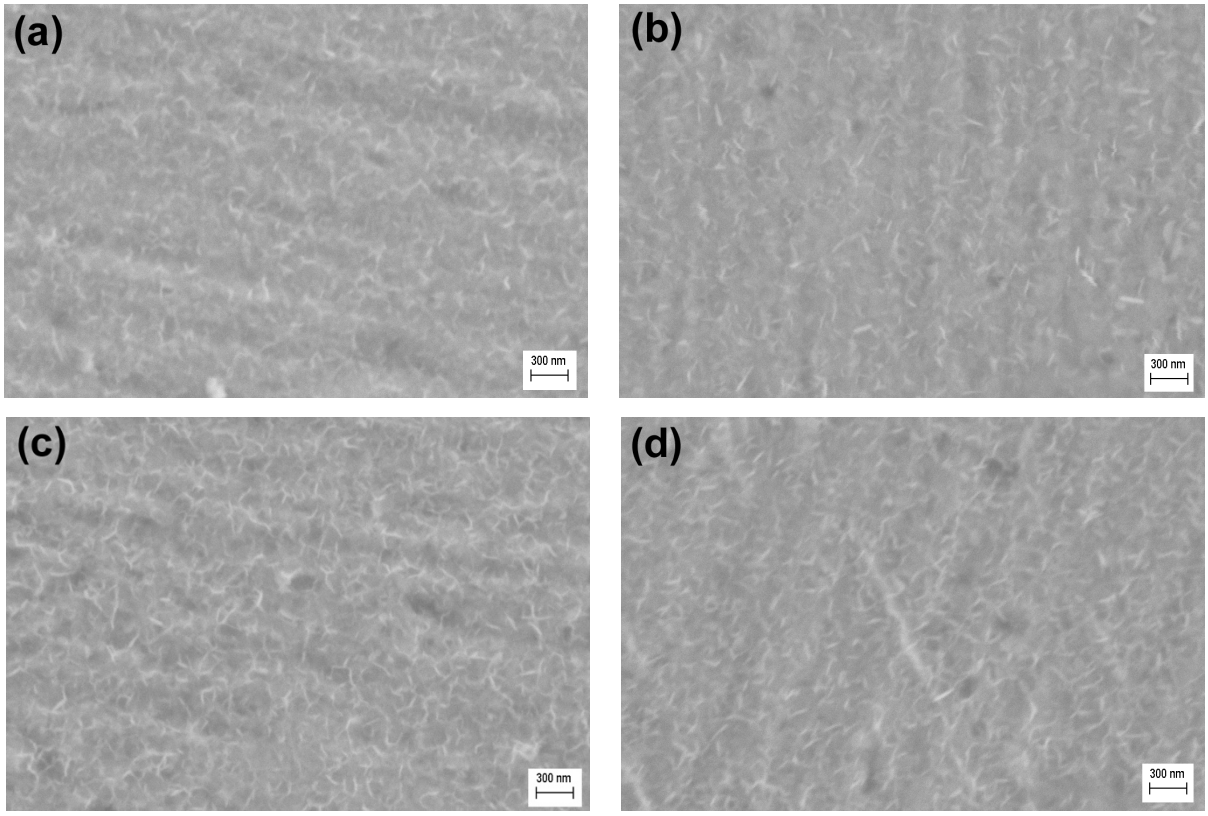

Fig. 3.17 SEM images of the surface of the passive layer formed on the different heat treated samples passivated at 0.5 $V_{Ag/AgCl}$ for 1 h in 0.1 M NaOH solution: **(a)** as-received (AR), **(b)** solution treated (ST), **(c)** peak aged (PA), **(d)** overaged (OA).

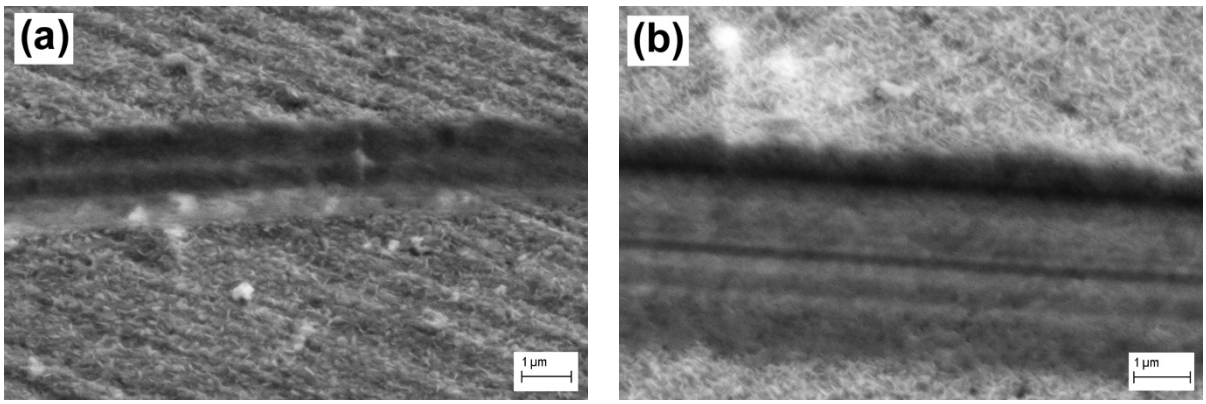

Fig. 3.18 SEM images of the surface of the passive layer formed on the different heat-treated samples passivated at 0.5 $V_{Ag/AgCl}$ for 36 h in 0.1 M NaOH solution: **(a)** as-received (AR), **(b)** peak aged (PA).

3.4 Conclusions

1. The highest chloride concentration that can be tolerated in 0.1 M NaOH without any corrosion of the WE43C in all heat treatment conditions was 200 ppm. The corrosion potential, transpassive potential, and the passivation current density were not significantly modified with the addition of up to 500 ppm Cl^- when compared to values in 0.1 M NaOH without chloride addition.

2. The as-received specimens showed the fastest kinetics of passivation and the highest impedance of passive film formation compared to other heat treatment conditions.

3. Localized corrosion was observed to be initiated on the secondary phases. The Zr-rich intermetallic particle having spherical morphology in all heat treated conditions and the irregular shape of peak aged condition were susceptible to localized corrosion.

4. The passive layer of the WE43C formed in 0.1 M NaOH solution under potentiostatic condition contained MgO, $Mg(OH)_2$, and RE_2O_3 phases, and the composition of the surface layer was independent of the heat treated condition.

Acknowledgements

The support provided by the US Nuclear Regulatory Commission through a faculty development grant NRC-HQ-84-15-G-0025 is gratefully acknowledged. J. Ninlachart acknowledges the support by Royal Thai Navy.

References

[1] A.C. Hanzi, I. Gerber, M. Schinhammer, J.F. Loffler, P.J. Uggowitzer, Acta Biomater. 6 (2010) 1824 – 1833

[2] M. Liu, P. Schmutz, P.J. Uggowitzer, G.L. Song, A. Atrens, Corros. Sci. 52 (2010) 3687 – 3701

[3] A.D. Sudholtz, K. Gusieva, X.B. Chen, B.C. Muddle, M.A. Gibson, N. Birbilis, Corros. Sci 53 (2011) 2277 – 2282

[4] P. Mengucci, G. Barucca, G. Riontino, D. Lussana, M. Massazza, R. Ferragut, E. Hassan Aly, Mater. Sci. Eng. A Struct. Mater. 479 (2008) 37 – 44

[5] I.J. Polmear, in: B.L. Mordike, F. Hehunann (Eds.), Mg Alloys and Their Applications, DGM Informations Gesellschaft, Oberursel, 1992, pp. 201

[6] Y.-H. Kang, H. Yan, R.-S. Chen, Mater. Sci. Eng. A Struct. Mater. 645 (2015) 361 – 368

[7] S. Kandalam, P. Agrawal, G.S. Avadhani, S. Kumar, S. Suwas, J. Alloys Compd. 623 (2015) 317 – 323

[8] S.K. Panigrahi, W. Yuan, R.S. Mishra, R. DeLorme, B. Davis, K. Cho, Mater. Sci. Eng. A Struct. Mater. 530 (2011) 28 – 35

[9] J.-W. Chang, X.-W. Guo, P.-H. Fu, L.-M. Peng, W.-J. Ding, Electrochim. Acta 52 (2007) 3160 – 3167

[10] Z. Shi, F. Cao, G.-L. Song, M. Liu, A. Atrens, Corros. Sci. 76 (2013) 98 – 118

[11] K. Zhang, X. Zhang, X. Deng, X. Li, M. Ma, J. Magnes. Alloys 1 (2013) 134 – 138

[12] M. Ascencio, M. Pekguleryuz, S. Omanovic, Corros. Sci. 91 (2015) 297 – 310

[13] M.I. Jamesh, G. Wu, Y. Zhao, D.R. McKenzie, M.M.M. Bilek, P.K. Chu, Corros. Sci. 91 (2015) 160 – 184

[14] W. Jin, G. Wu, H. Feng, W. Wang, X. Zhang, P.K. Chu, Corros. Sci. 94 (2015) 142 – 155

[15] W. Jin, G. Wu, A. Gao, H. Feng, X. Peng P.K. Chu, Surf. Coat. Technol. 306 (2016) 11 – 15

[16] A.R. Mirak, C.J. Davidson, J.A. Taylor, Appl. Surf. Sci. 301 (2014) 91 – 98

[17] H. Ardelean, A. Seyeux, S. Zanna, F. Prima, I. Frateur. P. Marcus, Corros. Sci. 73 (2013) 196 – 207

[18] L. Wang, T. Shinohara, B.-P. Zhang, Appl. Surf. Sci. 256 (2010) 5807 – 5812

[19] S. Feliu Jr., A. Pardo, M.C. Merino, A.E. Coy, F. Viejo, R. Arrabal, Appl. Surf. Sci. 255 (2009) 4102 – 4108

[20] K.M. Ismail, S. Virtanen, Electrochem. Solid-State Lett. 10 (3) (2007) c9 – c11

[21] F. Cao, G.L. Song, A. Atrens, Corros. Sci. 111 (2016) 835 – 845

[22] S. Li, A.C. Bacco, N. Birbilis, H. Cong, Corros. Sci. 112 (2016) 596 – 610

[23] M. Taheri, J.R. Kish, J. Electrochem. Soc. 160 (1) (2013) c36 – c41

[24] P.W. Chu, E.A. Marquis, Corros. Sci. 101 (2015) 94 – 104

[25] L. Chen, A. Lasia, J. Electrochem. Soc. 138 (1991) 3321 – 3328

[26] E. Gileadi, Physical Chemistry, first ed., Wiley – VCH, Weinheim, 2011 pp 98

[27] SH. Salleh, S. Thomas, J.A. Yuwono, K. Venkatesan, N. Birbilis, Electrochim. Acta 161 (2015) 144 – 152

[28] H. Dai, H. Yang, X. Liu, X. Jian, Z. Liang, Fuel 174 (2016) 251 – 256

[29] S. Fajardo, G.S. Frankel, Electrochim. Acta 165 (2015) 255 – 267

[30] J. K. Norskov, T. Bligaard, A. Logadottir, J.R. Kitchin, J.G. Chen, S. Pandelov, U. Stimming, J. Electrochem. Soc., 152 (2005) J23 – J26

[31] R. Pinto, M.G.S. Ferreira, M.J. Carmezim, M.F. Montemor, Electrochim. Acta 55 (2010) 2482 – 2489

[32] J. Chen, J. Wang, E.-H. Han, W. Ke, Corros. Sci. 51 (2009) 477 – 484

[33] H. Kalb, A. Rzany, B. Hensel, Corros. Sci. 57 (2012) 122 – 130

[34] M. Li, Y. Cheng, Y.F. Zheng, X. Zhang, T.F. Xi, S.C. Wei, Appl. Surf. Sci. 258 (2012) 3074 – 3081

[35] J. Yu, L. Cui, H. He, S. Yan, Y. Hu, H. Wu, J. Rare Earths, 32 (1) (2014) 1 – 4

[36] C.V. Raman, Proc. Ind. Acad. Sci. A26 (1947) 383 – 390

[37] H.D. Lutz, H. Müller, M. Schmidt, J. Mol. Struct. 328 (1994) 121 – 132

[38] A. Ubaldini, M. M. Carnasciali, J. Alloys Compd. 454 (2008) 374 – 378

CHAPTER 4

Passivation Kinetics of Mg-Nd-Gd-Zn-Zr (EV31A) and Mg-Y-Nd-Gd-Zr (WE43C) in NaOH Solutions

Jakraphan Ninlachart, Krishnan S. Raja
Chemical and Materials Engineering, University of Idaho, Moscow, ID 83844-1021, USA

Passivation Kinetics of Mg-Nd-Gd-Zn-Zr (EV31A) and Mg-Y-Nd-Gd-Zr (WE43C) in NaOH Solutions. Submitted to *Journal of Magnesium and Alloys.* Manuscript number JMA-D-17-00030.

Abstract

Passivation kinetics of two Mg-RE alloys, such as Mg-Nd-Gd-Zn-Zr (EV31A), and Mg-Y-Nd-Gd-Zr (WE43C) were investigated in two different heat treated conditions (solution treated and overaged) in 0.01 - 1.0 M NaOH solutions under potentiostatic conditions. Negative reaction order was observed in dilute NaOH which transitioned to positive values as the passivation time increased and in the 1 M NaOH as well. The passive layers showed platelet morphology and the size of the platelets decreased with increase in the NaOH concentration. The hydrogen evolution reaction (HER) kinetics was not improved on the passive layer covered surface of the Mg-RE alloys in contrast to the improvements reported on the hydroxide covered pure magnesium. The electrochemical impedance increased with increase in the NaOH concentration in the solution treated condition of both Mg-RE alloys, whereas the overaged EV31A alloy showed a reverse trend. The passive layer of EV31A showed almost 100% higher charge carrier density than the film formed on the WE43C in the overaged condition. A better passivation behavior was observed in the solution treated condition than that in the overaged condition which could be attributed to the uniform distribution of the RE elements in the solution treated specimens. The WE43C alloy revealed better corrosion resistance in the alkaline solution than the EV31A alloy.

Keywords: Magnesium rare earth alloy; Passivation; Alkaline solution; Hydrogen Evolution

4.1 Introduction

Corrosion and passivation behavior of pure magnesium in alkaline pH condition has been well documented [1 – 6]. When exposed to pH 10 solution, pure magnesium formed a surface layer consisting of $Mg(OH)_2$ with a morphology of 30 nm × 300 nm platelets [1]. Increase in the pH decreased the corrosion rate of Mg. Even though MgO layer was considered to form during the corrosion of Mg, the corrosion rate was related to the dissolution kinetics of $Mg(OH)_2$, since MgO hydrolyzed to $Mg(OH)_2$ layer [3]. Surface reaction between the OH^- and protons with an activation energy of 10 kcal/mole was considered a rate limiting step for the $Mg(OH)_2$ dissolution. At high pH conditions, the diffusion of dissolved $Mg(OH)_2$ away from the Mg surface was a rate limiting step [3]. Mg-Al-Zn alloy (AZ21) formed a surface film consisting of three layers such as a) an inner layer enriched in Al_2O_3, b) intermediate layer of MgO, and c) outer layer of $Mg(OH)_2$ [4].

Ismail and Virtanen [5] reported for the first time the fluctuations in OCP of AZ31 in 0.5 M KOH. The potential fluctuations were attributed to the breakdown of the surface layer by the internal stress developed within the outer layer during transformation of MgO to $Mg(OH)_2$. The Pilling-Bedworth ratio (PBR) of MgO is 0.81 and for $Mg(OH)_2$ is 1.74. The volume expansion incurred during the MgO $\rightarrow$ $Mg(OH)_2$ transformation induced significant internal stress on the outer layer. The rupture of the passive layer allowed the electrolyte permeated through the surface layer and attack the bottom layer causing formation of a new $Mg(OH)_2$ layer. This process repeated and showed fluctuations in the OCP of AZ31 [5]. Similar type of potential fluctuation was reported for commercial purity Mg in 1 M NaOH by Taheri and Kish [6]. The surface film formed in 1 M NaOH was found to be 50 - 150 nm thick crystalline MgO layer that was hydrated to different degrees to form amorphous $Mg(OH)_2$-rich nodules. The coverage of the $Mg(OH)_2$ nodules was reported to be partial in the alkaline solutions [6] whereas a continuous coverage of $Mg(OH)_2$ was noted in the pure water [7]. The effect of microstructures on the potential oscillations of AZ31B cast alloy was investigated by Li et al. [8] and the passive film breakdown at the oxide interface between primary α-matrix and eutectic phase was attributed to the potential oscillations.

Nordlien et al. [9] investigated the passive film formed on Mg-Al-Zn and Mg-Al-RE alloys after exposure to high purity water for 48 h. All the alloys showed a triple-layered surface film. Alloying with aluminum increased the stability of the passive film of Mg. Addition of RE

to the Mg-Al alloy system enhanced the stability of the passive layer further. However, Mg-RE binary alloy without Al-addition did not show improvement in the corrosion protection. Yamasaki et al. [10] investigated the passivation behavior of rapidly solidified Mg-Zn-Y-Al alloys in 0.17 M NaCl. The cooling rate and resulting supersaturated solid solution of material significantly affected the corrosion behavior. The outer layer of the passive film consisted mostly of $MgO/Mg(OH)_2$ and the inner layer had Y and Al incorporated $MgO/Mg(OH)_2$. The thickness of inner layer decreased with increase in the Al alloying addition.

Pinto et al. reported the electrochemical behavior of Mg-RE alloys in borate buffer solution (pH 9.2) and the corrosion resistance increased when the RE was present in solid solution [11]. Presence of amorphous Y_2O_3 increased the corrosion resistance of WE54 alloy. On the other hand, when the Mg-Zr-RE alloys were tested in alkaline solution (pH 13), presence of RE was not detected on the surface films even though the semiconducting behavior was different from that of pure $MgO/Mg(OH)_2$ [12]. Plasma electrolytic oxidation of WE43 alloy in T6 condition using silicate or phosphate based electrolytes revealed uniform distribution of Y and Nd throughout the coating [13]. Thicker film of Al_2O_3 from sputtering on Mg showed better corrosion resistance than thinner film of ZrO_2 [14]. Xu et al. [15] compared corrosion behavior of pure Mg, and pure RE (Y, Nd, Gd, Dy). The passivation behavior of pure RE in saline environment (pH 7) is weaker than of pure Mg.

The present authors reported threshold chloride concentrations required for breakdown of the passive formed on the EV31A, and WE43C alloys in the 0.1 M NaOH solutions by potentiodynamic polarization studies in their earlier publications [16, 17]. However, the effect of RE additions on the kinetics of passivation of Mg alloys is not fully understood, especially in the alkaline solutions. In this study, the kinetics of passivation of two Mg-RE alloys such as Mg-Nd-Gd-Zn-Zr alloy (EV31A), and Mg-Y-Nd-Gd-Zr alloy (WE43C) were systematically investigated in different concentrations of NaOH. The specimens were investigated in solution treated (ST) and overaged (OA) heat treatment conditions in order to understand the effect of secondary phases on the passivation kinetics. The hydrogen evolution behavior of the passive film covered surface of the Mg-RE alloys has been investigated. The NaOH electrolyte may not represent the real life service conditions in which magnesium alloys are generally used. Since the surface film formed on the Mg alloys are stable only above pH 10.5, the investigations using NaOH solutions help develop fundamental understanding of the passivation behavior.

The results point out that Mg alloys can potentially be used for storing caustic soda, an important chemical in paper and pulp, and textile industries.

4.2 Experimental

Mg-Nd-Gd-Zn-Zr (EV31A), and Mg-Y-Nd-Gd-Zr (WE43C) were provided by Magnesium Elektron N.A. Inc. in forms of 16-mm thick plates. Both materials were cut into 16 mm × 25 mm × 3 mm. EV31A designated as "solution treated (ST)" was given a solution heat treatment by soaking at 525°C for 8 h followed by quenching in room temperature water. The overaged (OA) specimens were given a solution heat treatment as described earlier and aged at 300°C for 4 h and cooled down in air to room temperature after the solution heat treatment. The samples were metallographically polished down to 1500 grit in dry condition for electrochemical tests, and to a 1 micron finish in wet condition for microstructural investigation, then cleaned with acetone. The optical microstructure investigation was conducted by using an OLYMPUS PMG3 optical microscope. The scanning electron microscopy (SEM) was conducted by using LEO SUPRA 35VP electron microscope.

The test solutions used in the electrochemical experiments were 0.01, 0.1, and 1 M NaOH which were prepared by using a reagent grade NaOH (EMD Chemicals, Inc.) and high purity deionized water (resistivity 18.2 MΩ-cm) obtained using a water purification system (Millipore, Model: Milli-Q PF Plus). Electrochemical tests were conducted using a home-made PTFE flat-cell (volume of electrolyte: 150 ml) exposing 1 cm^2 area of sample surface to the electrolyte and a 3-electrode configuration which consisted of Pt-wire counter electrode (2 cm^2 surface area), Ag/AgCl reference electrode (199 mV vs SHE), and the specimen as a working electrode. A computer controlled potentiostat (PAR VersaSTAT MC with VersaStudio software) was used to measure electrochemical data. The open circuit potential (OCP) was measured for 48 h from the samples exposed to 0.1 M NaOH solution. Potentiostatic tests were conducted at 0.1 and 0.5 V vs reference electrode in different NaOH concentrations. The data was plotted every 0.02 s for 2 min, and every 1 s for 1 h. The electrochemical impedance spectroscopy (EIS) was conducted at the passivation potential by scanning the frequency from 100 kHz to 10 mHz. Mott-Schottky measurements were carried out at a frequency of 316 Hz by scanning the potential from the potentiostatic passivation potential to the open circuit potential at 50 mV steps. All the electrochemical tests were duplicated, and in some cases

triplicated to verify the reproducibility. The tabulated values are average of the test runs, and the plots represent the best condition.

Gracing angle XRD, XPS, and Raman spectroscopy analyses were carried out on the surfaces of select samples after potentiostatic passivation. Gracing angle X-ray diffraction patterns were obtained using a Rigaku Smartlab 3 kW with Cu kα X-ray tube operated to 40 kV and 44 mA, where the incident angle of the X-rays was 0.5° with respect to the sample surface. A Thermo-Scientific DXR dispersive Raman microscope was used to characterize the Raman vibrational modes of the surface films. Raman spectra were obtained for individual spots with a diameter of 0.7 μm with 4 exposures of 8 seconds at 100 X magnification using a 532 nm laser operated at 10 mW.

4.3 Results and Discussion

Figure 4.1(a) – (b) shows the microstructure of the EV31A in solution treated and overaged conditions, respectively. The average grain size was 30 μm. Secondary phase precipitates could be observed even in the solution treated condition. These particles were identified as Nd/Gd-rich particles. High melting point of Nd and Gd could be the reason why they did not dissolve in solid solution as Y-rich and Zr-rich particles observed in solution treated of WE43 [18]. The cellular-type β phase (Mg_3RE) was observed in the overaged sample. Precipitates of $Mg_{12}Nd$ was observed in both the solution treated and overaged conditions [16].

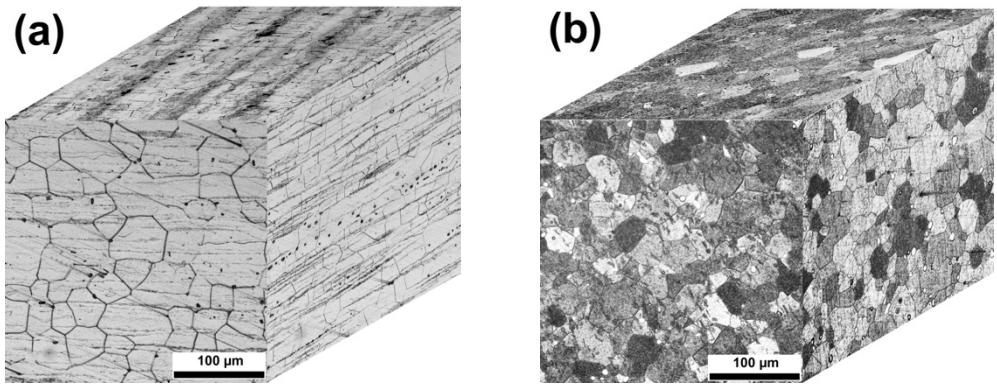

Fig. 4.1 Optical microstructures of EV31A: **(a)** Solution treated, **(b)** Overaged.

Figure 4.2(a) – (b) shows the microstructures of the WE43C specimen in solution treated and overaged conditions, respectively. Similar to EV31A in solution treated condition, the

undissolved $Mg_{12}Nd$ precipitates could be observed in solution treated of WE43C [17]. The average grain size was 46 μm. The overaged specimen showed dark-etched grains as seen in Fig. 4.2(b). The secondary phases observed in the overaged condition were $Mg_{11}NdY_2$, Mg_3RE, $Mg_{41}Nd_5$, and $Mg_{24}Y_5$ [17].

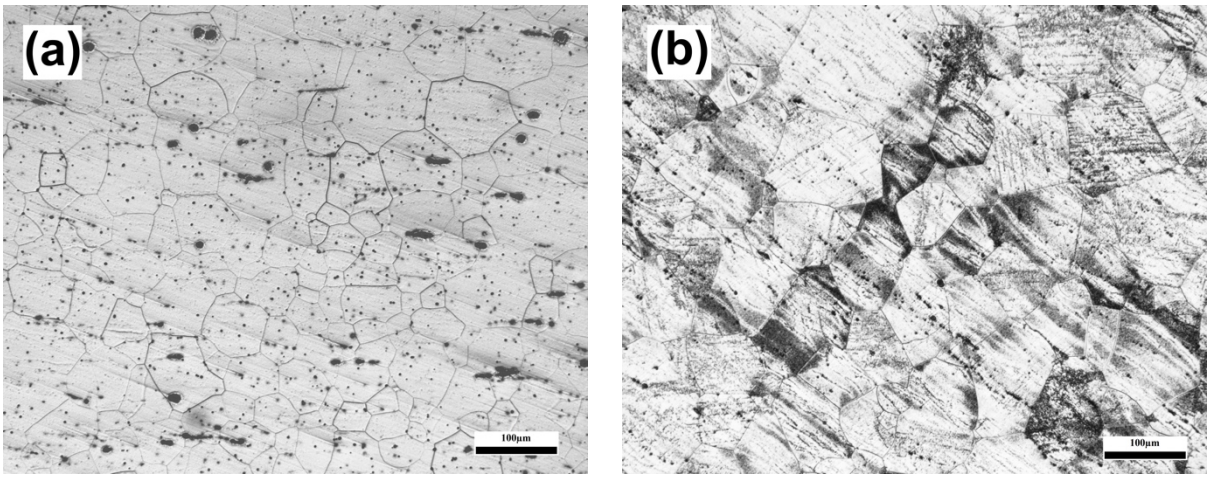

Fig. 4.2 Optical microstructures of WE43C: **(a)** Solution treated, **(b)** Overaged.

Figure 4.3(a) – (b) shows the open circuit (OCP) plots of EV31A specimens in solution treated and overaged conditions, respectively. The results showed that the OCP of solution treated specimen fluctuated quickly during the initial exposure, and the period of fluctuation was wider when exposure time increased. The OCP increased after each fluctuation and the third loop showed stabilization of the OCP for approximately 5.5 h before the OCP dropped to -1.6 $V_{Ag/AgCl}$. When the OCP recovered (moved upward) again, it was constant until the end of 48 h. The OCP showed an increasing trend even though periodic fluctuations occurred and after ~ 15 h it stabilized at about -0.4 $V_{Ag/AgCl}$. The OCP of overaged (OA) specimen increased sharply from -1.79 $V_{Ag/AgCl}$ to -1.2 $V_{Ag/AgCl}$ and then abruptly decreased to -1.6 $V_{Ag/AgCl}$ within the first 20 minutes of immersion. This type of abrupt fluctuation occurred again and then the OCP gradually increased exhibiting two shoulder like steps until 26 hours of exposure to a value of -0.53 $V_{Ag/AgCl}$. The OCP then dropped significantly to -1.47 $V_{Ag/AgCl}$, and swung back to -0.4 $V_{Ag/AgCl}$. After that point, the OCP was constant until 48 h.

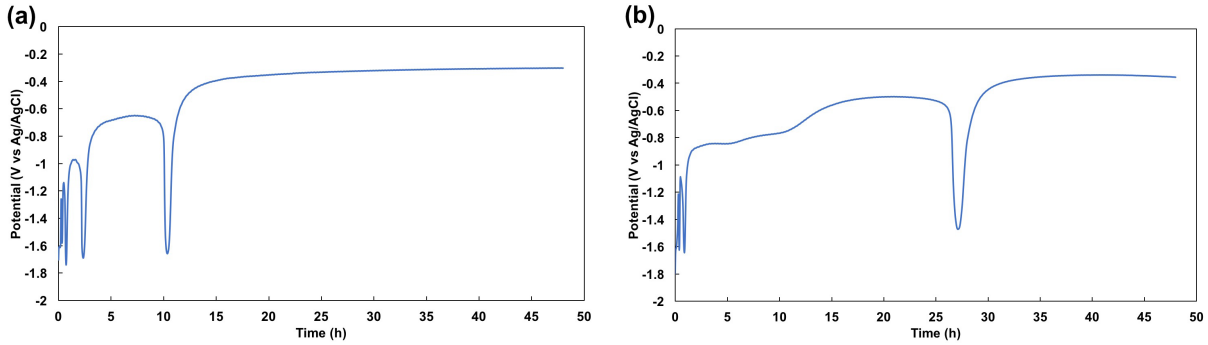

Fig. 4.3 OCP of EV31A specimens in 0.1 M NaOH solution recorded for 48 h: **(a)** Solution treated, **(b)** Overaged.

Figure 4.4(a) – (b) shows the open circuit (OCP) plots of WE43C specimens in solution treated and overaged conditions, respectively. OCP of both heat treatment conditions showed almost a similar behavior as that of their EV31A counterparts except that the overaged WE43C specimen did not show the fluctuation in the middle period (at ~ 26 h) of exposure. The fluctuation of OCP observed in EV31A and WE43C specimen may be attributed to the passive film formation-breakdown-recovery behavior due to internal stresses associated with the volume expansion of hydrated oxides [5 – 8, 18]. The fluctuations of the OCP of WE43 in NaCl solution as reported by Chu and Marquis [18] were much smaller than that observed in the NaOH solution of this study. The smaller fluctuations of the OCP values in the chloride solution could be attributed to the highly porous nature of the passive film and higher hydrogen evolution activity [18]. The gas evolution rate was significantly low in high pH conditions. In order to understand the film formation process on the Mg-RE alloys, the anodic and cathodic reactions were separated by potentiostatic control.

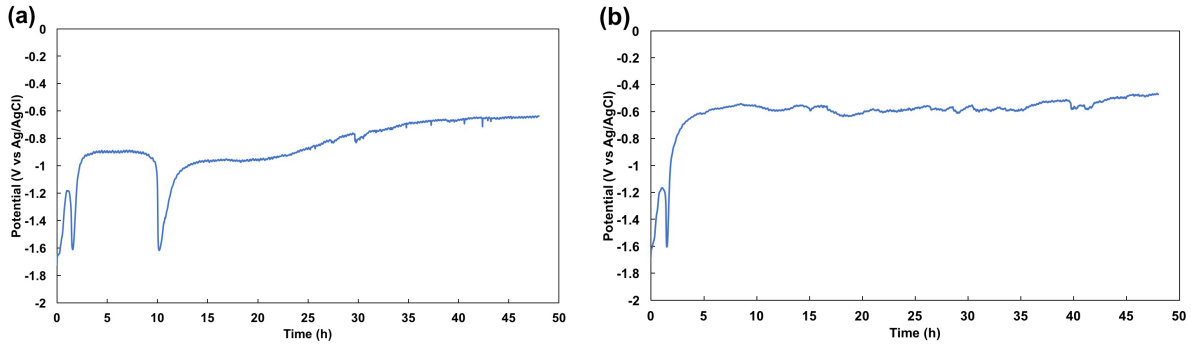

Fig. 4.4 OCP of WE43C specimens in 0.1 M NaOH solution recorded for 48 h: **(a)** Solution treated, **(b)** Overaged.

Under applied anodic potentials, formation of surface film could occur by the following reaction routes [19]:

$$Mg + H_2O \rightarrow MgO + 2H^+ + 2e^- \quad (1)$$

$$MgO + H_2O \rightarrow Mg(OH)_2 \quad (2)$$

$$Mg + 2H_2O \rightarrow Mg(OH)_2 + 2H^+ + 2e^- \quad (3)$$

$$Mg \rightarrow Mg^{2+} + 2e^- \quad (4)$$

$$Mg^{2+} + H_2O \rightarrow MgO + 2H^+ \quad (5)$$

$$Mg^{2+} + 2H_2O \rightarrow Mg(OH)_2 + 2H^+ \quad (6)$$

The reaction (2) could occur after the electrochemical reaction (1) or the MgO layer could form during exposure of the specimen surface to air. The air formed MgO layer could hydrolyze to $Mg(OH)_2$ which is a chemical reaction. On the same note the reaction (5) and (6) are chemical reactions. The reaction (1) and (3) could occur in multiple steps as proposed by Williams et al. [20, 21].

$$Mg + H_2O \rightarrow Mg(OH_{ads})\,(H_{ads}) \quad (7)$$

which is similar to Volmer reaction.

$$Mg(OH_{ads})\,(H_{ads}) \rightarrow Mg(O_{ads}) + 2H^+ + 2e^- \quad (8)$$

$$Mg(O_{ads}) + Mg(O_{ads}) \rightarrow 2MgO \quad (9)$$

$$Mg(OH_{ads})\,(H_{ads}) + H_2O \rightarrow Mg(OH_{ads})_2\,(H_{ads})_2 \quad (10)$$

$$Mg(OH_{ads})_2\,(H_{ads})_2 \rightarrow Mg(OH_{ads})_2 + 2H^+ + 2e^- \quad (11)$$

The above reactions are relevant for water adsorption conditions. In alkaline conditions, the above reactions under the anodic polarization conditions can be written as followed:

$$Mg + OH^- \rightarrow Mg(OH_{ads}) + e^- \quad (12)$$

$$Mg(OH_{ads}) + OH^- \rightarrow Mg(OH)_2 + e^- \quad (13)$$

$$Mg(OH_{ads}) + OH^- \rightarrow MgO^- + H_2O \quad (14)$$

$$MgO^- \rightarrow MgO + e^- \quad (15)$$

Reactions (14) and (15) imply the presence of Mg as Mg^+, which is controversial. Song and Atrens [22] proposed presence of Mg^+ reaction intermediates. However, existence of Mg^+ has not been experimentally verified and the theory has been contradicted by other researchers [23]. Here, the reaction (14) and (15) are hypothetically proposed to describe the formation of MgO in two steps. Presence of MgO was supported by Raman spectroscopy results as described in

a latter section. Hydrolysis of MgO to $Mg(OH)_2$ was attributed to the OCP fluctuations. In addition to Mg, other alloying elements also participate in the film formation. Chu and Marquis [18] reported incorporation of Nd in the oxide of the WE43 alloy, and Unocic et al. [24] reported incorporation of Nd in the oxide film of E717 alloy and enrichment of Nd, and Zn at the film/metal interface. The oxide or hydroxide formation of the RE elements such as Y, Nd, and Gd under potentiostatic conditions in alkaline solutions could be given by the reaction [25]:

$$RE + 3OH^- \rightarrow RE(OH)_3 + 3e^- \qquad (16)$$

Enhanced hydrogen evolution reaction kinetics have been reported on the $Mg(OH)_2$ covered surfaces by different groups [26, 27]. Such enhancement was attributed to the reduction in work function of the [OH^-] adsorbed surface which made the electron removal process easy for hydrogen reduction reaction (Heyrovsky pathway: $Mg(OH)_{ad} + H_3O^+ + e^- \rightarrow Mg(OH)_2 + H_2\uparrow$) [28]. Hydrogen evolution reaction (HER) kinetics of the surface film covered surface of the EV31A and WE43C specimens were evaluated by carrying out potentiodynamic polarization tests in the cathodic reaction. The results were compared with the cathodic polarization of the freshly polished specimens of identical heat treated conditions. The specimens were immersed in 0.1 M NaOH solution at open circuit condition for 48 hours and then passivated at 0.5 $V_{Ag/AgCl}$ for 1 h to obtain the surfaces covered with a passive layer. The cathodic polarization was carried out immediately after the potentiostatic passivation. The potential was scanned from the open circuit potential to -2.4 $V_{Ag/AgCl}$ at scan rate of 1 mV/s. Tafel slope, exchange current density of the HER, and over potential required for obtaining a current density of -1 mA/cm^2 were calculated from the polarization plots, and summarized in Table 4.1. The exchange current densities of the EV31A specimens increased significantly after the surfaces were covered with the passive layer. However, the Tafel slopes, and the over potential at -1 mA/cm^2 increased for the passive film covered surface of the EV31A alloy. The specimens of WE43C alloy also showed almost a similar behavior even though the increase in the Tafel slope and over potential values were less pronounced. Interestingly, there was no change in the exchange current density values of the WE43C specimens with and without passive film coverage. No significant difference in the HER kinetics could be observed between the solution treated (ST) and overaged (OA) specimens of both the alloys, even though the solution treated condition showed marginally higher exchange current density than the overaged condition. The reason for not showing improved HER behavior could be attributed

to the distribution of rare earth alloying elements in the passive layer that shielded the electrons from participating in the hydrogen reduction reaction. Based on the electronegativity values, and work functions [29], partial electron transfer could occur from the rare earth alloying elements to the magnesium matrix. However, presence of Zr or Zn atoms at the surface of the specimens would adversely affect the HER kinetics because of their higher work function and increased electronegativity. Furthermore, the adsorption energy or binding energy of hydrogen at alloying element sites also needs to be considered. Since the rare earth elements and Zr show high affinity to hydrogen and form hydrides, the HER kinetics will be adversely affected [30]. Overall, the results indicated that surface coverage of passive film of Mg-RE alloys did not increase the HER activity. This result has significant bearing on the hydrogen assisted environmental cracking behavior of the material which suggests that Mg-RE alloys may be less susceptible to hydrogen embrittlement.

Table 4.1 Summary of the cathodic polarization results of EA31A and WE43C specimens in two different heat-treated conditions in 0.1 M NaOH with different surface conditions.

Sample		Tafel slope V/dec	Exchange current density for hydrogen evolution, i_0 A/cm^2	Over potential for -1 mA/cm^2
EV31A	ST-fresh surface	-0.16	2.9×10^{-10}	-1.03
	ST-Film covered	-0.30	7.5×10^{-8}	-1.53
	OA-Fresh surface	-0.17	5.5×10^{-10}	-1.04
	OA-Film covered	-0.24	2.5×10^{-8}	-1.51
WE43C	ST-fresh surface	-0.21	6.0×10^{-9}	-1.15
	ST-film covered	-0.23	6.0×10^{-9}	-1.38
	OA-Fresh surface	-0.18	2.0×10^{-9}	-1.05
	OA-film covered	-0.21	1.7×10^{-9}	-1.33

Figure 4.5 shows the *i-t* plots in log-log scale of the EV31A solution treated specimens in different concentrations of NaOH at two different potentials (0.1 and 0.5 $V_{Ag/AgCl}$). The current recorded at 0.02 s was the highest in all the cases and the current decayed continuously with time, indicating formation of a surface film rendering passivity. The current density was higher in the 0.01 M NaOH than that in the 0.1 M or 1 M NaOH. In other words, the passivation current increased with decrease in the pH of the solution. The rate of current decay (slope of the log *i* vs log *t*, d(log *i*)/d(log *t*)) was shallower at the first 200 ms of potentiostatic condition which transitioned to a steeper slope between 1 and 10 s of passivation. After 10 s, the slope

become shallower or in some cases the sign of the slope changed indicating increase in the current density instead of a current decay.

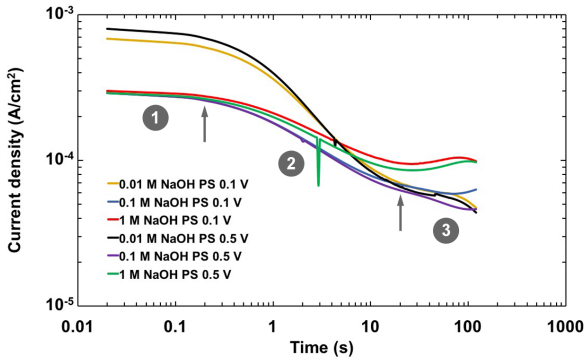

Fig. 4.5 *i-t* plots of the EV31A (solution treated condition) in different concentrations of NaOH at two different potentiostatic conditions.

The current decay behavior could be described using a simple relation [31]:

$$i_t = i_0 t^{\alpha} \qquad (17)$$

where i_t = current at time t

i_0 = instantaneous current at the time of application of the potential

α = exponent of the current transient or slope of the log i vs log t. More the negative value of the exponent, faster the kinetics of the passivation.

Table 4.2 summarizes the passivation exponent, α or slope of the log i vs log t, for different specimens at different passivation potentials. The negative values indicate current decay and continuation of the passivation whereas positive values of "α" indicate increase in current due to corrosion dissolution or passivity breakdown. From Table 4.2, it can be seen that the passivation kinetics of the solution treated EV31A increased with time in the dilute alkaline solution (0.01 M NaOH), but the passivation kinetics decreased with time in higher concentrations, at both applied potentials. Similar trends were observed for the overaged specimens of EV31A, as summarized in Table 4.2 and in Fig. 4.6. The overaged specimens of EV31A showed relatively larger oscillations in the current decay between 1 and 10 s of passivation. The passive current oscillations those were more significant in the overaged specimens could be related to the incoherent precipitates present in the overaged condition. The solution treated specimens showed faster passivation kinetics (more negative values of "α") than that of the overaged specimens. The faster kinetics could possibly be attributed to the

Table 4.2 Summary of slopes of log *i* vs log *t* of EV31A in different concentrations of NaOH at 0.1 and 0.5 $V_{Ag/AgCl}$.

NaOH concentration	Slope, α	EV31A				WE43C			
		Solution treated		Overaged		Solution treated		Overaged	
		Passivation potential ($V_{Ag/AgCl}$)		Passivation potential ($V_{Ag/AgCl}$)		Passivation potential ($V_{Ag/AgCl}$)		Passivation potential ($V_{Ag/AgCl}$)	
		0.1	0.5	0.1	0.5	0.1	0.5	0.1	0.5
0.01 M	Region 1	-0.149	-0.069	-0.085	-0.072	-0.084	-0.082	-0.082	-0.078
	Region 2	-0.643	-0.697	-0.662	-0.556	-0.663	-0.736	-0.632	-0.689
	Region 3	-0.144	-0.147	-0.324	-0.229	-0.093	-0.095	-0.206	-0.134
0.1 M	Region 1	-0.054	-0.054	-0.054	-0.052	-0.070	-0.066	-0.054	-0.058
	Region 2	-0.377	-0.398	-0.337	-0.376	-0.417	-0.396	-0.394	-0.417
	Region 3	-0.110	-0.203	0.037	-0.272	-0.253	-0.198	-0.187	-0.176
1 M	Region 1	-0.049	-0.053	-0.046	-0.040	-0.051	-0.053	-0.041	-0.040
	Region 2	-0.300	-0.324	-0.265	-0.281	-0.299	-0.336	-0.303	-0.293
	Region 3	0.040	0.073	-0.019	0.008	0.098	0.032	0.045	-0.005

uniform distribution of passivity inducing alloying elements in the solid solution. When large secondary phase precipitates formed in the overaged condition that were incoherent with the matrix, the stability of the passive film was affected as observed from the large current oscillations.

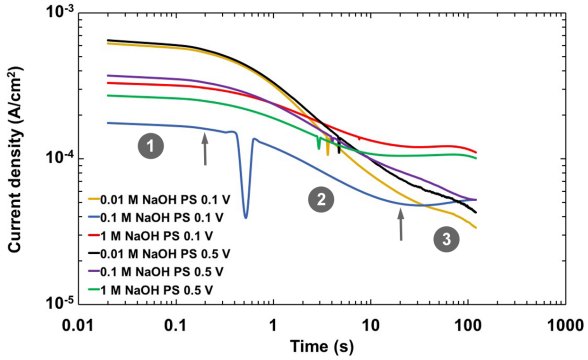

Fig. 4.6 *i-t* plots of the EV31A (overaged condition) in different concentrations of NaOH at two different potentiostatic conditions.

Figure 4.7 and 4.8 show the *i-t* plots of the WE43C specimens in solution treated and overaged conditions. The slopes of the *i-t* plots are summarized in Table 4.2. The passivation behavior of the WE43C alloy was similar to that of EV31A, including larger oscillations of current profile for the overaged condition. Figure 4.9(a) – (d) shows the passivation current at two different potentials as a function of the concentration of NaOH for the EV31A solution treated specimen. These plots are based on the data presented in Fig. 4.5.

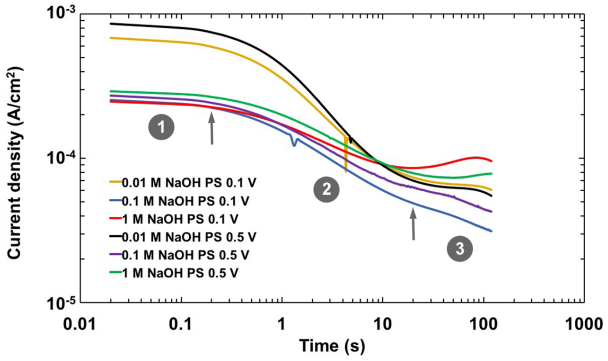

Fig. 4.7 *i-t* plots of the WE43C (solution treated condition) in different concentrations of NaOH at two different potentiostatic conditions.

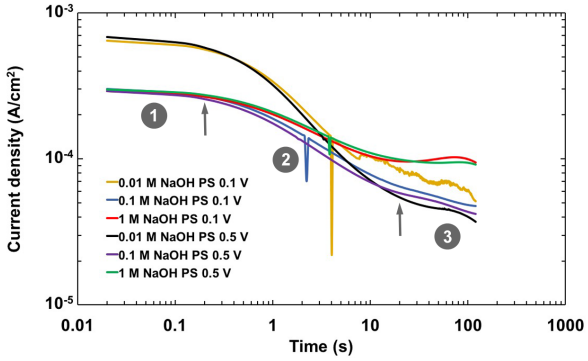

Fig. 4.8 *i-t* plots of the WE43C (overaged condition) in different concentrations of NaOH at two different potentiostatic conditions.

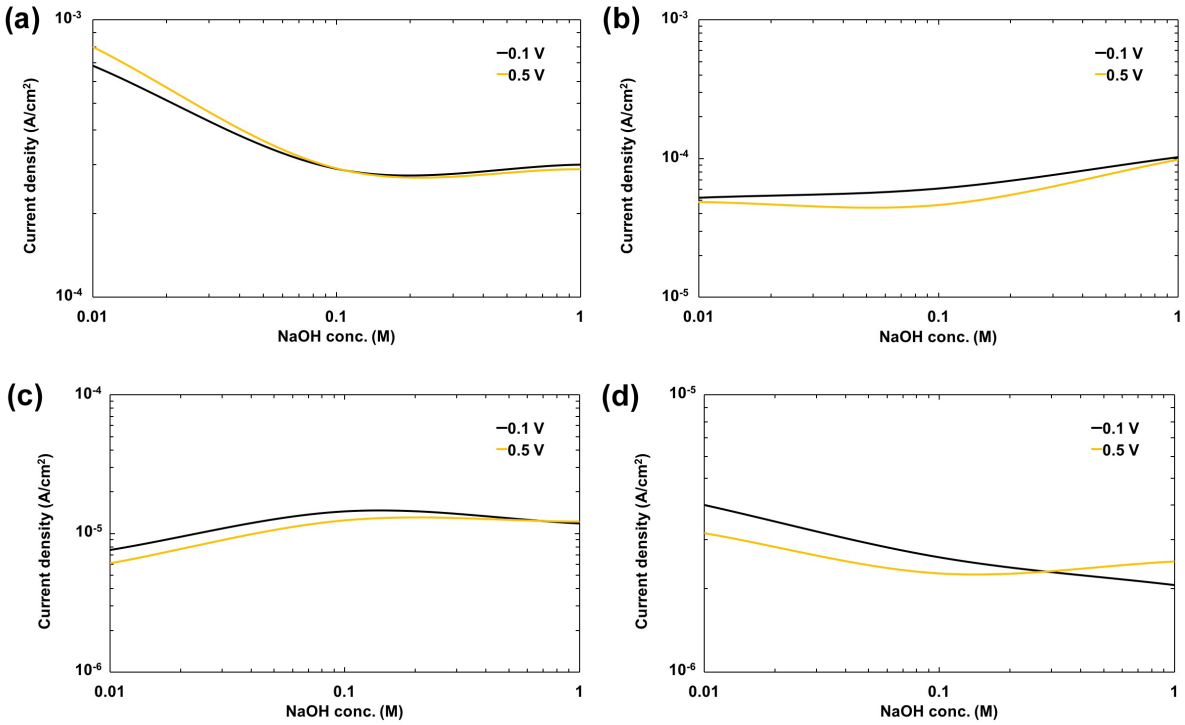

Fig. 4.9 Hydroxyl (OH^-) ion concentration vs current density plots recorded at two different potentiostatic conditions (0.1 and 0.5 $V_{Ag/AgCl}$) at different times for the EV31A solution treated (ST) specimens: **(a)** at t = 0.02 s, **(b)** t = 100.02 s, **(c)** t = 1000 s, **(d)** t = 3600 s.

Table 4.3 summarizes the slopes of the log *i* vs log C_{OH^-} at different time zones and different potentials. The slope gives an idea about the reaction order (*m*). The passivation current (i_p) can be given as (based on the reaction (12)):

$$i_p = Fk_1(C_{OH^-})^m (1 - \theta)exp(\frac{\beta F}{RT}\eta) \qquad (18)$$

where θ = surface coverage of adsorbed hydroxyl species

η = over potential

β = symmetry factor or transfer co-efficient [32]

k_1 = rate constant for the forward reaction (12)

m = order of the reaction

The variation in the surface coverage the passive $Mg(OH)_2$ as a function of time can be expressed using standard electrode kinetics relations as [32]

$$d\theta/dt = [k_1(1 - \theta)(C_{OH^-})^m] - [k_{-1}\theta(C_{OH^-})] + [k_2\theta(C_{OH^-})^m] - [k_{-2}(1-\theta)(C_{OH^-})] \quad (19)$$

where k_2 and k_{-2} are rate constants of forward and reverse reactions of (13)

The slope of the log i vs log C_{OH^-} plots at lower concentrations (between 0.01 and 0.1 M NaOH) of OH^- were negative and in the range of -0.053 and -0.543. The negative slope could be described as $m = d(\log i)/d(\log C_{OH^-}) = (\alpha_{an} - 1)$, where α_{an} is transfer co-efficient of the anodic reaction on the Mg-RE specimens [32]. The negative slope indicated that the passive current density decreased with increase in the hydroxyl ion concentration. At lower concentration of OH^- the surface coverage was low and therefore the corrosion current due to magnesium oxidation (reaction (4)) was high. With increase in the OH^- concentration in the solution the surface coverage "θ" increased, and therefore the i_p, decreased following the relation (18). During the initial period of potentiostatic conditioning (t < 100 s), all the specimens (both EV31A and WE43C in two heat treated conditions) showed a negative reaction order. Figure 4.10(a) – (d) shows the plots of log i vs log C_{OH^-} of the overaged specimens of EV31A alloy. Figures 4.11 and 4.12 illustrate the log i vs log C_{OH^-} plots of the WE43C alloy in solution treated and overaged conditions, respectively.

Positive reaction order ($m = 1 - \alpha_{an}$) was observed when the NaOH concentration increased to 1 M. Furthermore, mostly positive slopes were observed in between 100 - 1000 s of passivation. The slope increased with increase in the time of passivation, in general, for most of the specimens. After 1 h of passivation, a negative reaction order was observed on the Mg-RE alloy specimens except for the EV31A-OA. The overaged EV31A alloy showed a positive reaction order after 100 s of passivation. Increase in the passivation potential to 0.5 V showed relatively low values of the slope as compared to the slopes recorded at 0.1 V.

When the reaction order is compared between the heat treated conditions of a particular alloy based on the data given in Table 4.3, it can be observed that the overaged specimen of

Table 4.3 Summary of the slope m = [d(log i)/d(log C_{OH^-})] of the Mg-RE alloys in different concentrations of NaOH at two different bias potentials.

Material	sec	PS 0.1 V		PS 0.5 V	
		slope 0.01-0.1M	slope 0.1-1M	slope 0.01-0.1M	slope 0.1-1M
EV31A ST	0.02	-0.372	0.015	-0.438	-0.003
	0.12	-0.368	0.023	-0.431	0.003
	1.02	-0.298	0.067	-0.340	0.039
	10.02	-0.053	0.135	-0.057	0.112
	100.02	0.067	0.227	-0.021	0.327
	1000	0.279	-0.087	0.310	-0.009
	3600	-0.189	-0.100	-0.145	0.043
EV31A OA	0.02	-0.543	0.275	-0.240	-0.138
	0.12	-0.530	0.279	-0.230	-0.132
	1.02	-0.421	0.300	-0.145	-0.096
	10.02	-0.142	0.375	0.004	0.036
	100.02	0.151	0.347	0.061	0.294
	1000	0.412	0.241	0.369	0.094
	3600	0.161	0.169	0.121	0.117
WE43C ST	0.02	-0.433	-0.009	-0.497	0.028
	0.12	-0.428	-0.0002	-0.492	0.035
	1.02	-0.364	0.049	-0.412	0.070
	10.02	-0.180	0.181	-0.088	0.105
	100.02	-0.284	0.485	-0.119	0.243
	1000	0.118	-0.090	0.196	-0.040
	3600	-0.099	-0.140	0.040	-0.075
WE43C OA	0.02	-0.331	-0.013	-0.371	0.011
	0.12	-0.326	-0.006	-0.361	0.021
	1.02	-0.252	0.032	-0.261	0.078
	10.02	-0.124	0.128	-0.012	0.201
	100.02	-0.098	0.316	0.034	0.337
	1000	0.257	-0.086	0.266	-0.021
	3600	0.076	-0.169	-0.052	-0.029

EV31A showed steeper slopes at 0.1 V than those of solution treated specimens. On the other hand, the trend reversed at 0.5 $V_{Ag/AgCl}$. In case of WE43C alloy, the solution treated specimens showed steeper slopes than those of overaged specimens in both constant potential conditions. Comparing the results between two alloys in a given heat treated condition, it was observed that the WE43C showed steeper slopes in the solution treated condition than the EV31A. These

comparisons are based on the first 100 s of potentiostatic passivation. Steeper negative slope of log *i* vs log C_{OH^-} is expected to yield a continuous, pore free surface layer that will be more resistant to corrosion than that obtained under shallow negative slopes or positive slopes.

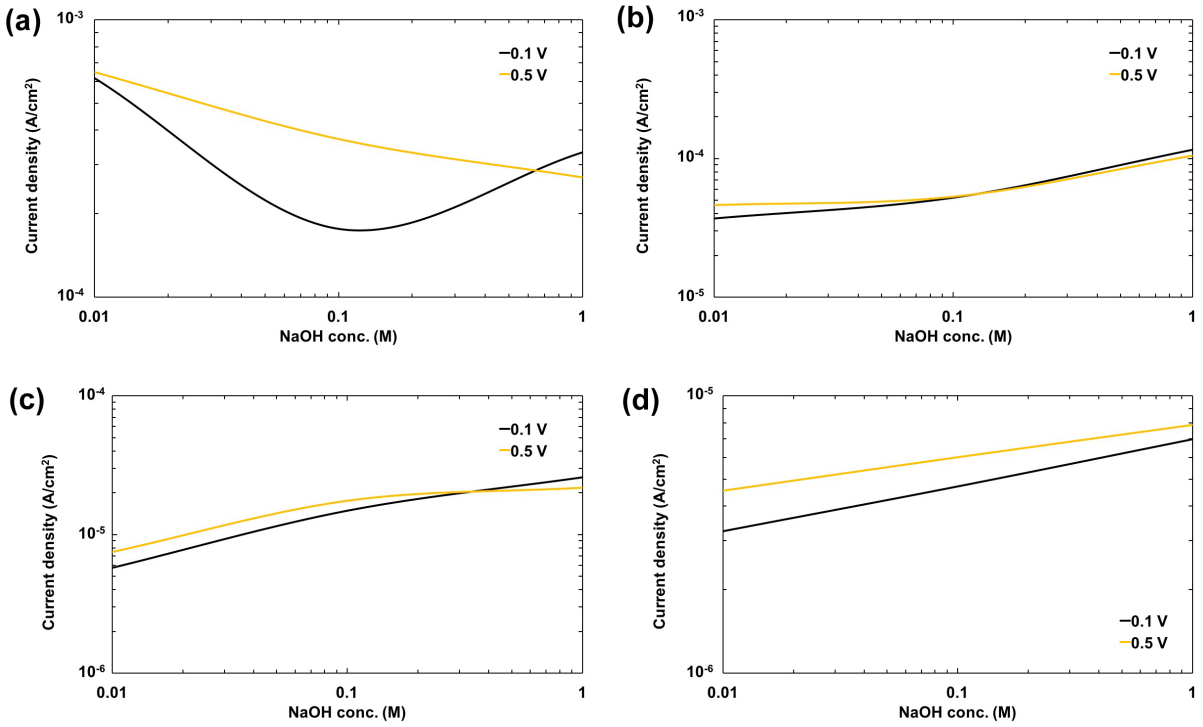

Fig. 4.10 Hydroxyl (OH^-) ion concentration vs current density plots recorded at two different potentiostatic conditions (0.1 and 0.5 $V_{Ag/AgCl}$) at different times for the EV31A overaged (OA) specimens: **(a)** at t = 0.02 s, **(b)** t = 100.02 s, **(c)** t = 1000 s, **(d)** t = 3600 s.

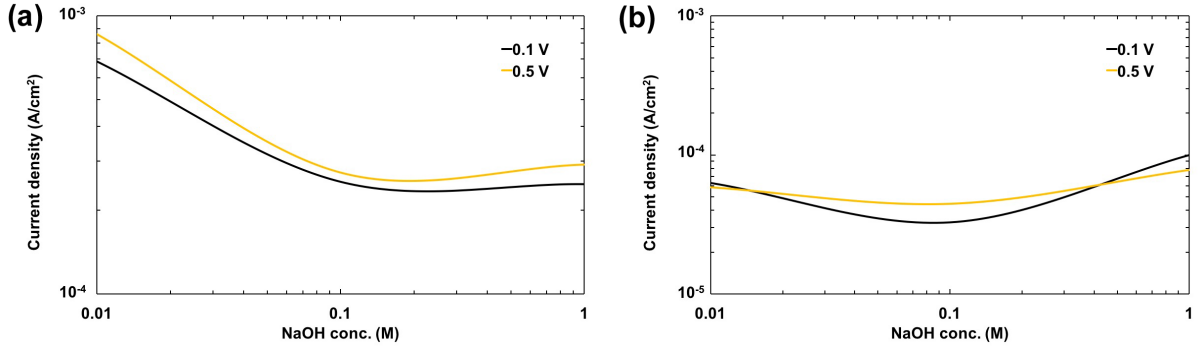

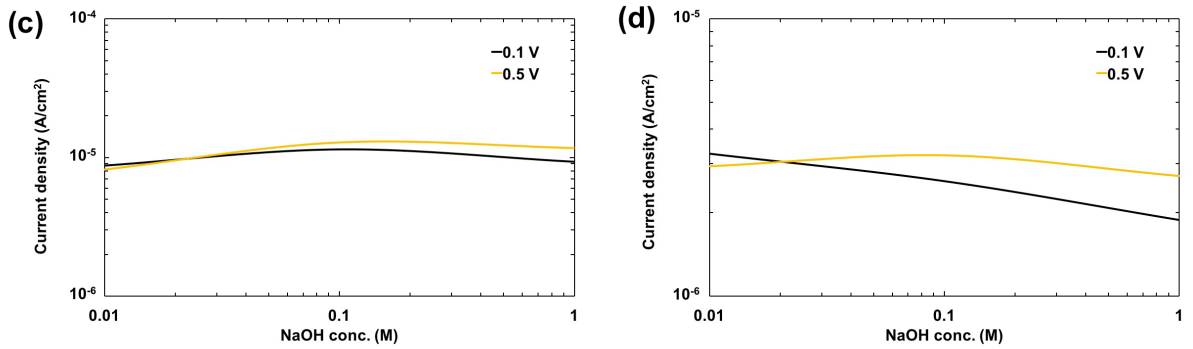

Fig. 4.11 Hydroxyl (OH^-) ion concentration vs current density plots recorded at two different potentiostatic conditions (0.1 and 0.5 $V_{Ag/AgCl}$) at different times for the WE43C solution treated (ST) specimens: **(a)** at t = 0.02 s, **(b)** t = 100.02 s, **(c)** t = 1000 s, **(d)** t = 3600 s.

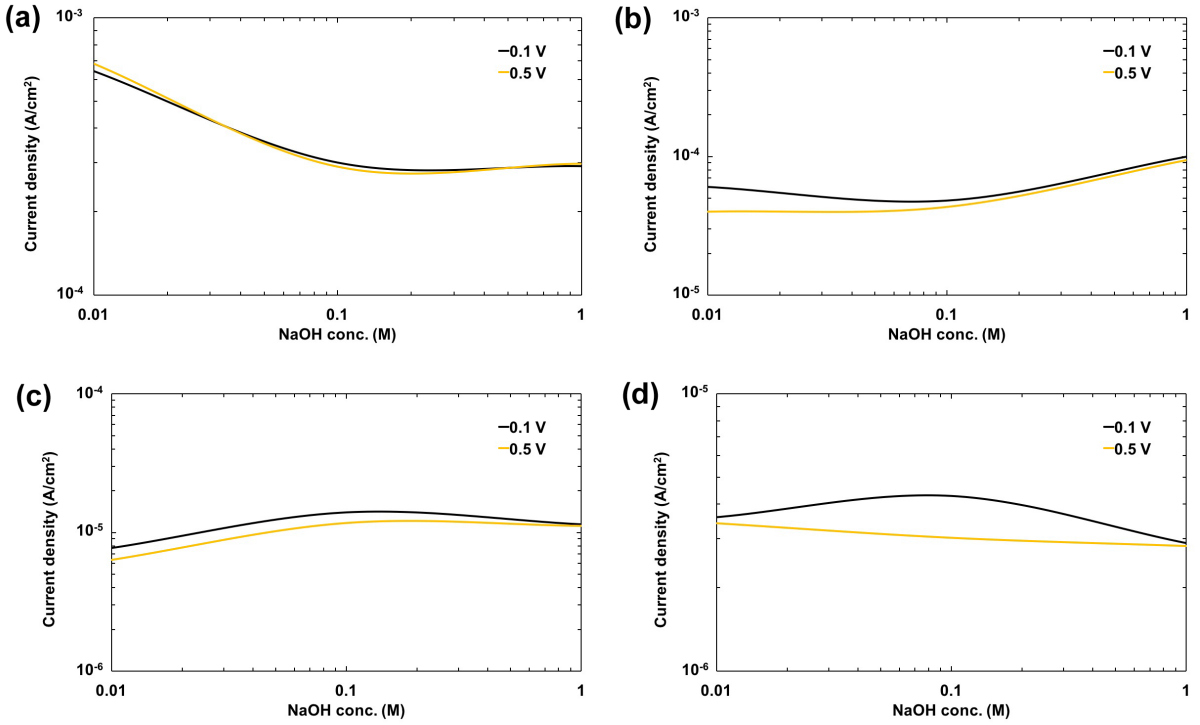

Fig. 4.12 Hydroxyl (OH^-) ion concentration vs current density plots recorded at two different potentiostatic conditions (0.1 and 0.5 $V_{Ag/AgCl}$) at different times for the WE43C overaged (OA) specimens: **(a)** at t = 0.02 s, **(b)** t = 100.02 s, **(c)** t = 1000 s, **(d)** t = 3600 s.

Table 4.4 summarizes the theoretically calculated surface layer thickness based on the charge passed on during the potentiostatic passivation. The calculated thickness values are much higher than the experimentally determined values, in general. This is because during the theoretical calculation, 100% Faradaic efficiency is assumed for film formation but in reality the dissolution of Mg as Mg^{2+} in the electrolyte is significant. In this work, no attempt was made to determine the concentration of Mg^{2+} in the electrolyte after passivation runs.

Furthermore, accurate determination of the surface film thickness using FESEM was not possible without employing focused electron beam to get the cross sectional view. The values in Table 4.4 can be used for a qualitative comparison between different heat treated conditions. At lower concentration of NaOH (0.01 and 0.1 M), the thickness of film formed at 0.1 V during first 2 min of passivation was almost similar for both of the heat treated conditions of EV31A. Increased concentration of NaOH to 1 M showed relatively thicker film. Interestingly, passivation at 0.5 V showed thinner film than that obtained at 0.1 V for both alloys. Overaged EV31A samples revealed thinner films in 0.01 and 0.1 M NaOH solutions than the solution treated EV31A specimens.

Table 4.4 Comparison of theoretical thickness of passive film (calculated based on charge accumulated) formed under potentiostatic conditions in different concentrations of NaOH at two different time durations.

Material	NaOH concentration (M)	Passivation potential (V)	Thickness (nm) after 2 min	after 1 h
EV31A ST	0.01	0.1	485	1680
		0.5	467	1432
	0.1	0.1	466	2828
		0.5	399	2431
	1	0.1	728	2666
		0.5	672	2755
EV31A OA	0.01	0.1	376	1260
		0.5	465	1777
	0.1	0.1	369	2928
		0.5	493	3394
	1	0.1	867	4723
		0.5	756	4388
WE43C ST	0.01	0.1	530	1896
		0.5	521	1706
	0.1	0.1	302	2070
		0.5	393	2419
	1	0.1	680	2305
		0.5	522	2390
WE43C OA	0.01	0.1	540	1841
		0.5	381	1418
	0.1	0.1	415	2759
		0.5	377	2280
	1	0.1	721	2619
		0.5	694	2604

WE43C specimens showed thicker passive films after 2 min of passivation in most cases. After 1 h of passivation, the thickness of the passive film increased with increase in the concentration of NaOH for both alloys. WE43C in solution treated condition showed relatively thinner film than that of EV31A solution treated in 0.1 and 1 M NaOH. Similar trend was observed also in the overaged conditions. WE43C in solution treated condition showed relatively thinner films than those observed in the overaged condition after 1 h of passivation. Overall, WE43C showed thinner surface layers than that of EV31A.

Figures 4.13 and 4.14 illustrate Nyquist plots of the electrochemical impedance spectroscopy (EIS) results of the EV31A and WE43C specimens, respectively. Tables 4.5 and 4.6 summarize the EIS equivalent circuit model parameters. The EIS measurement was conducted after passivation for 1 h under potentiostatic condition. The impedance of solution treated of EV31A in 1 M NaOH was the highest while that of overaged in 1 M NaOH was the lowest as seen in Fig. 4.13. When comparing the impedance in different pH electrolytes for the same heat treatment condition, it could be seen that the impedance of solution treated condition decreased as the OH^- concentration decreased. In contrast, the impedance of overaged specimen decreased as the OH^- concentration increased. The impedance of the WE43C in solution treated condition in 1 M NaOH also showed the highest magnitude as observed in the EV31A. In addition, solution treated conditions showed higher impedance than overaged conditions in all NaOH concentrations. Both of the heat treatment conditions showed a decrease in the impedance as the OH^- concentration decreased.

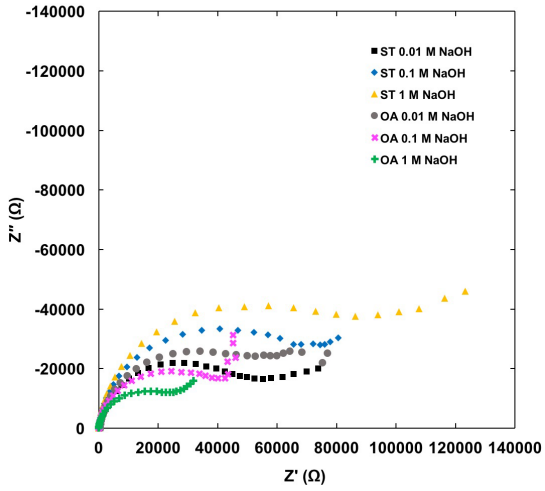

Fig. 4.13 Comparison of Nyquist plots of EV31A specimens with different heat treatment conditions in different concentrations of NaOH under potentiostatic 0.1 V condition.

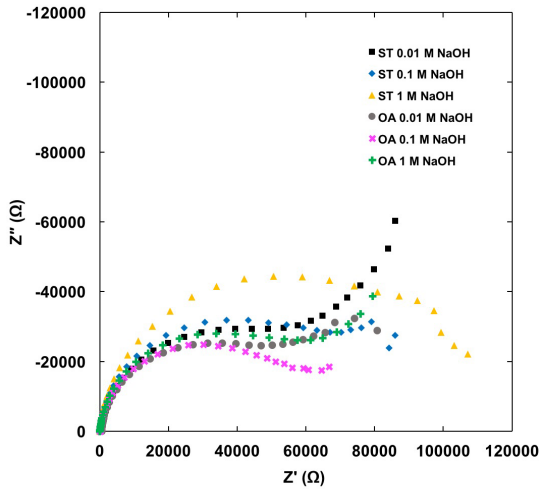

Fig. 4.14 Comparison of Nyquist plots of WE43C specimens with different heat treatment conditions in different concentrations of NaOH under potentiostatic 0.1 V condition.

The passive films of EV31A and WE43C showed two different electrical equivalent circuits as shown in Figures 4.15 and 4.16. EV31A showed a disconnected porous structure (represented by R_2 and Q_2) embedded in a thicker matrix represented by R_1 and Q_1 in parallel. A physical representation of this circuit could be discrete distribution of embedded $Mg(OH)_2$ or $RE(OH)_3$ nodules in a matrix of MgO [18, 33]. The overaged condition of EV31A showed higher Q_1 and Q_2 values, in general, than that of solution treated condition. Furthermore, the values of Q_1 and Q_2 of the overaged E31A specimen increased with increase in the OH^- concentration. This observation indicates that the incoherent secondary phase precipitates possibly acted as conducting paths and detrimentally affected the passivation.

The EIS data of WE43C alloy specimens could be fitted with a 2-parallel RC circuits connected in series, as seen in Fig. 4.16. This represents a dual-layered passive layer structure based on the existing literature data [17, 18, 33]. The bottom layer possibly be attributed to the MgO/RE_2O_3 represented by R_2 and Q_2 and the hydrated $Mg(OH)_2/RE(OH)_3$ type top layer represented by R_1 and Q_1. Table 4.6 summarizes the model parameters of WE43C. The resistance of the electrolyte, R_s, decreased with increase in the NaOH concentration as expected. The R_1 values of the overaged were higher than those calculated for the solution treated specimens. There were no significant variations in the Q_1 and Q_2 values between the two heat treatment conditions. The R_2 values of the solution treated condition were higher than those of overaged condition which could be attributed to the RE in the solid solution.

Table 4.5 Summary of model parameters of the EIS equivalent circuit components of the EV31A alloy after 1 h potentiostatic passivation at 0.1 $V_{Ag/AgCl}$.

Sample	NaOH concentration (M)	R_s (Ohm)	Q_1 ($S{\cdot}s^{\alpha}$)	α	Q_2 ($S{\cdot}s^{\beta}$)	β	R_1 (Ohm)	R_2 (Ohm)	Goodness of Fitting
Solution-	0.01	0.01	2.010×10^{-5}	0.8	8.402×10^{-6}	0.8	1.714×10^{5}	5.579×10^{2}	6.275×10^{-4}
treated	0.1	63.71	1.406×10^{-5}	0.926	1.976×10^{-4}	0.646	4.456×10^{12}	7.185×10^{3}	5.449×10^{-4}
	1	7.183	1.539×10^{-5}	0.917	2.589×10^{-5}	1	1.455×10^{5}	3.273×10^{5}	2.514×10^{-3}
Overaged	0.01	502.4	9.618×10^{-6}	0.94	4.863×10^{-5}	0.483	2.299×10^{5}	5.873×10^{4}	2.986×10^{-4}
	0.1	0.01	2.519×10^{-5}	0.8	1.567×10^{-5}	0.94	1.000×10^{16}	5.711×10^{2}	4.854×10^{-3}
	1	7.374	2.949×10^{-5}	0.914	3.665×10^{-4}	0.679	4.009×10^{11}	2.680×10^{5}	1.505×10^{-3}

Table 4.6 Summary of model parameters of the EIS equivalent circuit components of the WE43C alloy after 1 h potentiostatic passivation at 0.1 $V_{Ag/AgCl}$.

Sample	NaOH concentration (M)	R_s (Ohm)	Q_1 ($S{\cdot}s^{\alpha}$)	α	Q_2 ($S{\cdot}s^{\beta}$)	β	R_1 (Ohm)	R_2 (Ohm)	Goodness of Fitting
Solution-	0.01	492.8	1.140×10^{-5}	0.935	1.178×10^{-4}	0.828	5.365×10^{4}	1.894×10^{6}	6.916×10^{-4}
treated	0.1	56.27	1.304×10^{-4}	0.8	1.389×10^{-5}	0.8	6.840×10^{3}	5.615×10^{4}	3.675×10^{-4}
	1	6.59	5.258×10^{-5}	0.8	1.837×10^{-5}	0.8	7.162×10^{4}	5.187×10^{4}	5.759×10^{-4}
Overaged	0.01	554.2	1.304×10^{-4}	0.832	1.222×10^{-5}	0.937	7.481×10^{5}	4.483×10^{4}	4.160×10^{-4}
	0.1	54.8	1.635×10^{-5}	0.953	1.578×10^{-4}	0.793	4.291×10^{4}	4.166×10^{4}	3.180×10^{-4}
	1	6.832	1.390×10^{-4}	0.799	1.852×10^{-5}	0.965	8.461×10^{5}	4.757×10^{4}	8.525×10^{-4}

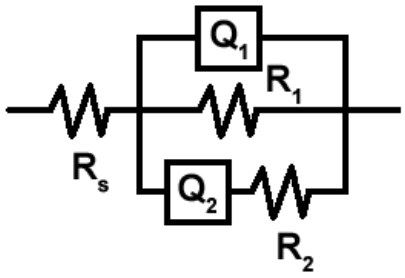

Fig. 4.15 Electrical equivalent circuit fitted the data of Nyquist plots of EV31A specimens.

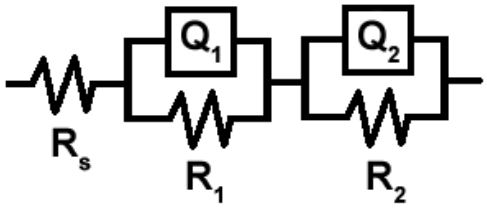

Fig. 4.16 Electrical equivalent circuit fitted the data of Nyquist plots of WE43C specimens.

Table 4.7 Summary of the charge carrier densities of the passive films of EV31A and WE43C alloys formed in different concentrations of NaOH after 1 h passivation at 0.1 $V_{Ag/AgCl}$.

Sample	NaOH concentration (M)	Charge carrier density of EV31A, N_D ($1/cm^3$)	Charge carrier density of WE43C, N_D ($1/cm^3$)
Solution treated	0.01	2.29×10^{21}	3.21×10^{21}
	0.1	3.61×10^{21}	4.18×10^{21}
	1	4.14×10^{21}	4.30×10^{21}
Overaged	0.01	2.52×10^{21}	3.91×10^{21}
	0.1	5.03×10^{21}	4.90×10^{21}
	1	12.33×10^{21}	6.06×10^{21}

Table 4.7 summarizes the charge carrier densities calculated based on the Mott-Schottky plots. All the plots showed *n*-type semiconducting behavior. The charge carrier density increased with increase in the concentration of NaOH, for both alloys and both heat treated conditions. The overaged specimen of both alloys showed higher charge carrier densities than the solution treated specimen. The passive film of the solution treated specimen of both alloys showed almost similar charge carrier densities, implying that the alloy chemistry did not significantly alter the electronic property of the passive layer. On the other hand, the passive film of overaged EV31A showed much higher charge carrier density than that determined for the overaged WE43C alloy. This implies that the WE43C overaged specimen may have better

corrosion resistance than the EV31A overaged. The EIS and Mott-Schottky results obtained on the specimens passivated at 0.5 $V_{Ag/AgCl}$ were similar to that of the results obtained at 0.1 $V_{Ag/AgCl}$.

Figure 4.17(a) – (d) shows the morphology of the surface layer formed under potentiostatic conditions on the EV31A alloy specimens in solution treated and overaged conditions. The film formed in 0.01 M NaOH showed platelet morphology of the $Mg(OH)_2$ phase. At higher concentration (0.1 M NaOH) and high applied potential, dissolution of the $Mg(OH)_2$ possibly occurred that resulted in relatively smoother surface film as seen in Fig. 4.17(b) or much smaller platelet structure as seen in Fig. 4.17(c). The surface film formed on the overaged sample in 0.01 M NaOH showed a densely packed platelet morphology.

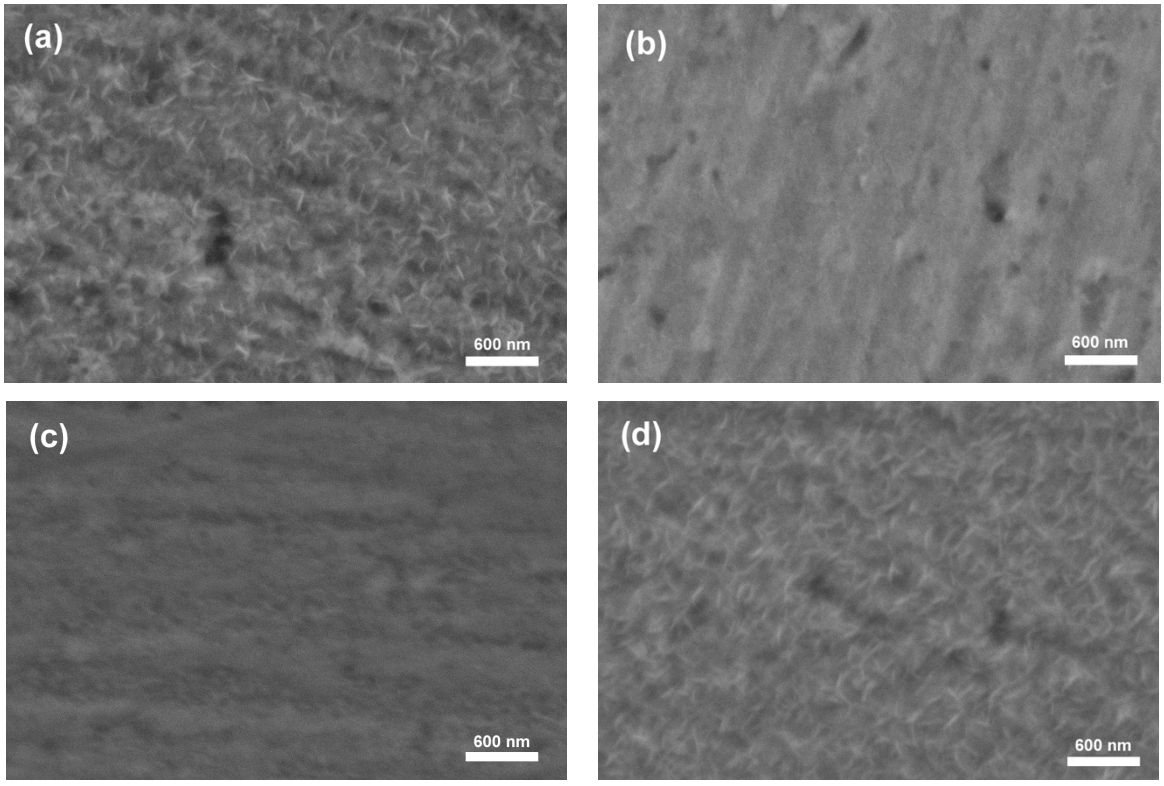

Fig. 4.17 SEM images the outer surface layer of the EV31A specimens passivated under different conditions for 1 h: **(a)** ST specimen passivated at 0.5 $V_{Ag/AgCl}$ in 0.01 M NaOH, **(b)** ST specimen passivated at 0.5 $V_{Ag/AgCl}$ in 0.1 M NaOH, **(c)** ST specimen passivated at 0.1 $V_{Ag/AgCl}$ in 0.1 M NaOH, **(d)** OA specimen passivated at 0.1 $V_{Ag/AgCl}$ in 0.01 M NaOH.

Figure 4.18(a) – (e) shows the morphology of the surface film on the WE43C specimens. The size of the platelets decreased with the increase in the NaOH concentration. It can be concluded that such reduction in the size of the platelet resulted in a more resistant porous free

surface film. There was no significant difference in the morphology of the surface films formed on the solution treated and overaged specimens as seen in Fig. 4.17(a) and 4.17(d).

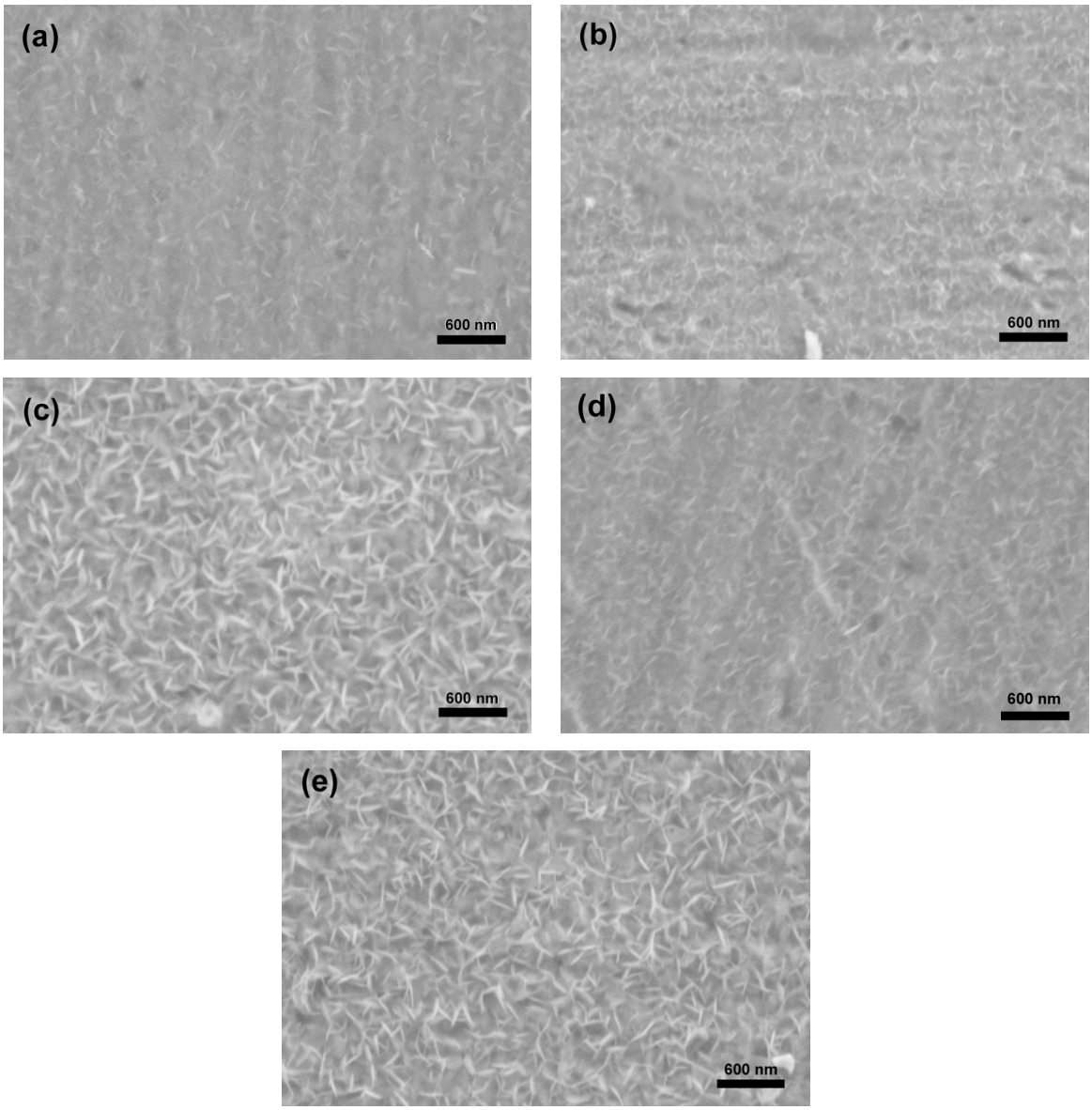

Fig. 4.18 SEM images the outer surface layer of the WE43C specimens passivated under different conditions for 1 h: **(a)** ST specimen passivated at 0.5 $V_{Ag/AgCl}$ in 0.1 M NaOH, **(b)** ST specimen passivated at 0.5 $V_{Ag/AgCl}$ in 1 M NaOH, **(c)** OA specimen passivated at 0.5 $V_{Ag/AgCl}$ in 0.01 M NaOH, **(d)** OA specimen passivated at 0.5 $V_{Ag/AgCl}$ in 0.1 M NaOH, **(e)** OA specimen passivated at 0.1 $V_{Ag/AgCl}$ in 0.01 M NaOH.

Figure 4.19(a) – (b) shows the glancing angle XRD patterns of the passivated specimens of the EV31A and WE43C alloys. In addition to the peaks corresponding to the substrate, peaks associated with $Mg(OH)_2$, $MgGd_2Zr_2O_8$ (JCPDS# 03-065-0426), and $NaGdO_2$ (JCPDS# 01-072-7629) could be identified in both alloys.

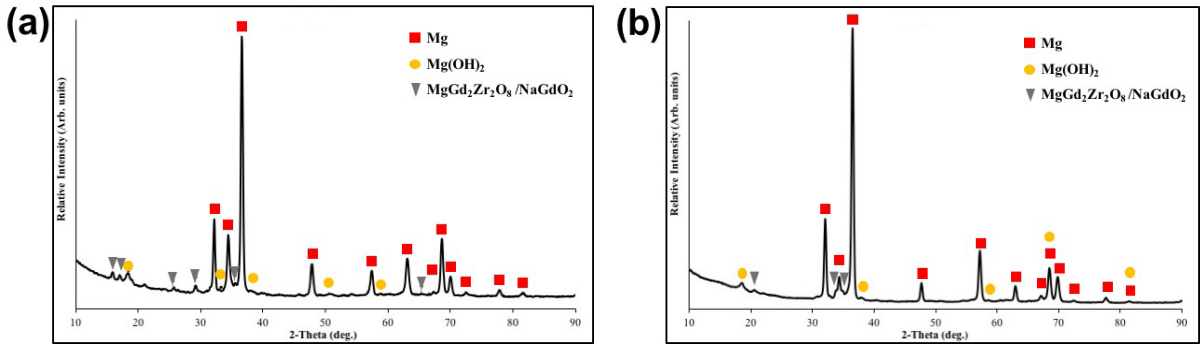

Fig. 4.19 Glancing angle XRD of the solution treated Mg-RE specimens after passivation at 0.5 $V_{Ag/AgCl}$ for 36 h in 0.1 M NaOH solution: **(a)** EV31A, **(b)** WE43C. The peak with (▼) could be identified as $MgGd_2Zr_2O_8$ through JCPDS card No: 03-065-0426, or $NaGdO_2$ through JCPDS card No: 01-072-7629.

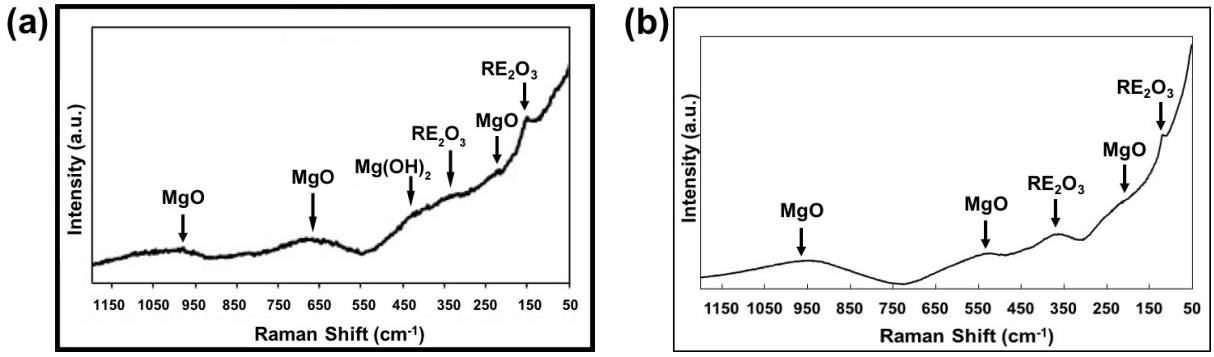

Fig. 4.20 Raman spectra of the solution treated Mg-RE specimens after passivation at 0.5 $V_{Ag/AgCl}$ for 36 h in 0.1 M NaOH solution **(a)** EV31A, **(b)** WE43C.

Figure 4.20(a) – (b) shows the Raman spectra of the passive layers formed on the EV31A and WE43C specimens, respectively. In Fig. 4.20(a), a broad peak between 650 – 680 cm^{-1} was observed which could be attributed to the present of MgO. Raman [34] identified the peaks of MgO at 652, 658 and 680 cm^{-1} and assigned the peaks with ν_3 (oscillation of Mg and O in opposite phases), $\nu_6 + \nu_9$ (normal oscillation of octahedral layers of Mg + tangential oscillations of cubic planes Mg and O in same phase) and ν_2 (tangential oscillation of cubic planes, Mg and O in opposite phase), respectively. The broader peak observed at 1001 cm^{-1} is also assigned to $\nu_5 + \nu_6$ vibrations of the MgO. The broader peak around 443 cm^{-1} is assigned to A_{1g} vibration mode of $Mg(OH)_2$. Figure 4.20(b) shows the Raman spectra of the WE43C surface layer. The observed peaks were at 130, 330, 530, and 975 cm^{-1}. The peaks at 130, 330 cm^{-1} could possibly be assigned to Y_2O_3 as reported by Yu et al. [35], and the peaks at 530 and 975 cm^{-1} could be identified as MgO based on the reported values of 527 and 980 cm^{-1} for the ν_5 (tangential oscillation of octahedral O layers and Mg at rest), and $\nu_1 + \nu_8$ (normal oscillation

of cubic planes, Mg and O atoms in same phase ($_{v1}$) + normal oscillation of cubic planes, Mg and O atoms in opposite phases ($_{v8}$)) oscillations, respectively [34]. The ex-situ Raman analyses of the passive layer showed that the passive layers of EV31A and WE43C were composed of MgO, $Mg(OH)_2$, and RE_2O_3.

4.4 Conclusions

1. The slope of the passivation current vs time in log-log scale was considered as a parameter for characterizing the passivation kinetics of the Mg-RE alloys. The passivation kinetics increased initially and decreased after about 100 s of passivation at constant potentials. Furthermore, the kinetics decreased with increase in the OH^- concentration. There was no significant difference in the kinetic exponent values between the solution treated and overaged conditions, even though the solution treated specimens showed relatively faster kinetics.
2. The slope of log i vs log C_{OH^-}, reaction order, was negative at low OH^- concentrations and positive at high OH^- concentration during the first 100 s of passivation. At longer passivation times only a positive reaction order was observed.
3. The ex-situ Raman analyses of the passive layer showed that the passive layers of EV31A and WE43C were composed of MgO, $Mg(OH)_2$, and RE_2O_3.
4. The passive film formed on the Mg-RE alloys showed platelet morphology in the NaOH electrolyte and the size of the platelets decreased with increase in the concentration of the NaOH.
5. The passive layer formed on the WE43C (Mg-Y-Nd-Gd-Zr) alloy was relatively thinner than the layer formed on the EV31A (Mg-Nd-Gd-Zn-Zr) alloy.
6. The thickness of the passive film increased with the increased concentration of NaOH under potentiostatic conditions.
7. The passivation behavior of the overaged condition was inferior to that of solution treated condition.
8. The passive layer covered EV31A specimens showed higher exchange current density for the hydrogen evolution reaction (HER) than the polished surface condition.
9. No improvements on the HER kinetics were observed for the passive layer covered WE43C alloy specimens compared to that of polished surface conditions.

Acknowledgements

The support provided by the U.S. Nuclear Regulatory Commission through a faculty development grant NRC-HQ-84-15-G-0025 is gratefully acknowledged. J. Ninlachart acknowledges the support by Royal Thai Navy. Glancing angle XRD, and Raman spectroscopy were carried out using the facilities available at the Materials Characterization Center, University of Nevada, Reno. The authors thank Prof. Dev Chidambaram, and Zach Karmiol for carrying out the surface analyses.

References

[1] D.A. Vermilyea, C.F. Kirk, J. Electrochem. Soc. 116 (1969) 1487 – 1492

[2] G. Song, A. Atrens, D. St John, J. Nairn, Y. Li, Corros. Sci. 39 (5) (1997) 855 – 875

[3] D.A. Vermilyea, J. Electrochem. Soc. 116 (1969) 1179 – 1183

[4] G. Song, A. Atrens, X. Wu, B. Zhang, Corros. Sci. 40 (1998) 1769 – 1791

[5] K.M. Ismail, S. Virtanen, Electrochem. Solid-State Lett. 10 (3) (2007) C9 - C11

[6] M. Taheri, J.R. Kish, J. Electrochem. Soc. 160 (2013) C36 - C41

[7] M. Taheri, R.C. Phillips, J.R. Kish, G.A. Bolton, Corros. Sci. 59 (2012) 222 – 228

[8] S. Li, A.C. Bacco, N. Birbilis, H. Cong, Corros. Sci. 112 (2016) 596 – 610

[9] J.H. Nordlien, K. Nisancioglu, S. Ono, N. Masuko, J. Electrochem. Soc. 144 (1997) 461 – 466

[10] M. Yamasaki, S. Izumi, Y. Kawamura, H. Habazaki, Appl. Surf. Sci. 257 (2011) 8258 – 8267

[11] R. Pinto, M.G.S. Ferreira, M.J. Carmezim, M.F. Montemor, Electrochim. Acta 56 (2011) 1535 – 1545

[12] R. Pinto, M.G.S. Ferreira, M.J. Carmezim, M.F. Montemor, Electrochim Acta 55 (2010) 2482 – 2489

[13] R. Arribal, E. Matykina, P. Skeldon, G.E. Thompson, A. Pardo, J. Electrochem. Soc. 155 (2008) C101 - C111

[14] R. Kotoka, S. Yarmolenko, D. Pai, J. Sankar, J. Mater. Sci. Technol. 31 (2015) 873 – 880

[15] X. Zhao, L-l. Shi, J. Xu, J. Mater. Sci. Technol. 29 (9) (2013) 781 – 787

[16] J. Ninlachart, K.S. Raja, Acta Metall. Sinica (Engl. Lett.) 30 (4) (2017) 352 – 366

[17] J. Ninlachart, Z. Karmiol, D. Chidambaram, K.S. Raja, in press, J. Magnesium Alloys, 10.1016/j.jma.2017.03.003

[18] P-W. Chu, E.A. Marquis, Corros. Sci. 101 (2015) 94 – 104

[19] M. Pourbaix, *Atlas of Electrochemical Equilibria in Aqueous Solutions* (NACE International, CEBELCOR, Houston Texus, Brussels, 1974)

[20] K.S. Williams, V. Rodriguez-Santiago, J.W. Andzelm, Electrochim. Acta 210 (2016) 261 – 270

[21] K.S. Williams, J.P. Labukas, V. Rodriguez-Santiago, J.W. Andzelm, Corrosion 71 (2015) 209 – 223

[22] G. Song, A. Atrens, D. St John, X. Wu, J. Nairn, Corros. Sci. 39, (1997) 1981 – 2004

[23] S. Thomas, N.V. Medhekar, G.S. Frankel, N. Birbilis, Curr. Opin. Solid State Mater. Sci. 19 (2015) 85 – 94

[24] K.A. Unocic, H.H. Elsentriecy, M. P. Brady, H.M. Meyer III, G.L. Song, M. Fayek, R.A. Meisner, B. Davis, J. Electrochem. Soc. 161 (6) (2014) C302 - C311

[25] W.M. Latimer, *Oxidation Potentials* (Prentice-Hall Inc., New York, 1952) p. 293

[26] S.H. Salleh, S. Thomas, J.A. Yuwono, K. Venkatesan, N. Birbilis, Electrochim. Acta 161 (2015) 144 – 152

[27] G.L. Song, K.A. Unocic, Corros. Sci. 98 (2015) 758 – 765

[28] J.A. Yuwono, N. Birbilis, K.S. Williams, N.V. Medhekar, J. Phys. Chem. C 120 (2016) 26922 – 26933

[29] H.B. Michaelson, J. Appl. Phys. 48 (1977) 4729 – 4733

[30] V.A. Yartys, O. Gutfleisch, V.V. Panasyuk, I.R. Harris, Journal of Alloys Compd. 253 – 254 (1997) 128 – 133

[31] K.S. Raja, D.A. Jones, Corros. Sci. 48 (2006) 1623 – 1638

[32] E. Gileaid, *Physical Electrochemistry* (Wiley-VCH, Verlag GmbH & Co 2011) pp. 79

[33] H. Ardelean, A. Seyeux, S. Zanna, F. Prima, I. Frateur, P. Marcus, Corros Sci. 73 (2013) 196 – 207

[34] C.V. Raman, Proc. Indian Academy of Science, The vibration spectra of crystals Part IV magnesium oxide, A26 (1947) 383 – 390

[35] J. Yu, L. Cui, H. He, S. Yan, Y. Hu, H. Wu, J. Rare Earths, 32 1 (2014) 1 – 4

CHAPTER 5

Stress Corrosion Cracking of Mg-Zn-Gd-Nd-Zr Alloy (EV31A) and Mg-Y-Nd Alloy (WE43C) Using U-bend Test

Jakraphan Ninlachart, Krishnan S. Raja
Chemical and Materials Engineering, University of Idaho, Moscow, ID 83844-1021, USA

Stress Corrosion Cracking of Mg-Zn-Gd-Nd-Zr Alloy (EV31A) and Mg-Y-Nd Alloy (WE43C) Using U-bend Test. Submitted to *Corrosion Science.* Manuscript number CORSCI_2017_789.

Abstract

Stress corrosion cracking (SCC) of Mg-Zn-Gd-Nd-Zr (EV31A) and Mg-Y-Nd (WE43C) alloys was investigated by using U-bend method. Open circuit potential (OCP) was measured during the tests in 0.1 M NaOH solution with different chloride concentrations. EV31A and peak-aged WE43C failed by SCC in 80 ppm chloride solution at OCP. When crack initiation occurred the OCP decreased continuously. The OCP profile could be used for monitoring SCC failure of the Mg-RE alloy components in real life service. Applied potentials in SCC susceptible zones did not cause SCC in EV31A specimens, but accelerated SCC of the WE43C peak-aged specimen in transpassive region.

Keywords: Magnesium rare earth alloy; Stress corrosion cracking; U-bend test; Chloride

5.1 Introduction

Magnesium alloys are candidate structural materials for the automobile and aircraft applications because of their high strength to weight ratio comparable to Al alloys. However, their corrosion resistance is inferior to Al alloys' corrosion resistance. In order to be used in aerospace and high performance automotive industries high strength at elevated temperature is required. Mg-RE-Zr alloys such as EV31A (Mg-Zn-Gd-Nd-Zr alloy), and WE43C (Mg-Y-Nd alloy) retain high strength at elevated temperatures (~300 ºC) [1]. Addition of rare earth elements such as Nd, Gd, and Y impart strengthening at high temperatures due solid solution strengthening and precipitation hardening due to formation of metastable β' and β_1 phases [2].

Mg alloys are susceptible to stress corrosion cracking (SCC) [3]. When materials with specific microstructures are subjected to stress above a threshold level and exposed to susceptible environment, SCC is likely to occur. The probability of SCC may depend on alloying elements; for example, Zr-containing alloys are less susceptible than Zr-free alloys [4], and Mg alloys with the compositions containing rare-earth elements are reported to have improved SCC resistance [5]. Manufacturing method of Mg alloy may be another factor which influences SCC; for example, wrought Mg alloys are more susceptible than casting Mg alloys [4].

Kannan et al. [5] studied SCC behavior of Mg-RE alloys such as ZE41, QE22 and EV31A (Elektron 21) and compared the results with that of AZ80 in distilled water, and 0.5 wt.% NaCl solution under slow strain rate test (SSRT) conditions. The results showed that AZ80 was equally susceptible to SCC both in distilled water, and 0.5 wt.% NaCl solution, while ZE41, QE22 and EV31A were more susceptible to SCC in 0.5 wt.% NaCl than in distilled water. AZ80 showed transgranular cracking (TGSCC) along with pitting corrosion, and ZE41 showed mixed mode crack growth consisting of intergranular cracking (IGSCC) due to grain boundary dissolution, and TGSCC in some areas in 0.5 wt.% NaCl solution. QE22 also reportedly showed both TGSCC and IGSCC (predominant) and corrosion products were observed on the fracture surface [5]. EV31A also showed mixed TGSCC and IGSCC modes in 0.5 wt.% NaCl solution. These authors attributed TGSCC of Mg-RE alloys to mechanism involving hydrogen, while IGSCC was related to corrosion of secondary phase particles along grain boundaries [5]. The fracture mode was also a function of grain size of the materials. Finer grains in AZ80 showed TGSCC mode, whereas, coarser grains in ZE41, QE22, and EV31A showed mixed TGSCC and IGSCC modes [5].

Padekar et al. [6, 7, 8] investigated SCC behavior of EV31A (Elektron 21) in different electrolytes such as distilled water, 0.01 M and 0.1 M NaCl saturated with $Mg(OH)_2$ solution, and compared the results with that of AZ91E by using SSRT and constant load test (CLT). The SSRT results showed that both EV31A and AZ91E were susceptible to SCC in all three environments investigated. EV31A showed better SCC resistance than AZ91E. The fracture mode of AZ91E was TGSCC in all the test solutions, while EV31A revealed TGSCC in distilled water, and mixed IGSCC and TGSCC in chloride-containing solutions [7]. The constant load test was carried out only 0.1 M NaCl saturated with $Mg(OH)_2$ solution [6, 8]. The results

showed that 60% of the yield stress was sufficient to cause SCC in AZ91E, whereas no SCC failure was observed in EV31A even after 1008 h test at a stress level of more 100% of the yield strength [8].

Raman et al. [9] studied SCC behavior of biodegradable and Al-free Mg alloys ZX50, WZ21, and WE43 in simulated human body fluid by using SSRT. They found out that WE43 failed in ductile feature in air because of mechanical overload whereas it showed mixed TGSCC and IGSCC in simulated human body fluid. IGSCC was related to large precipitates at grain boundaries which caused electrochemical dissolution. They also applied potentiostatic polarization in cathodic region during SSRT, then compared with SSRT at OCP condition. The results showed not much difference in total strain-to-failure between cathodic bias and OCP of WE43, and the fracture mode was TGSCC and failure was associated with hydrogen assisted cracking [9].

Most of the reports on SCC of Mg-RE alloys pertain to testing under SSRT. Since the samples are subjected to continuous straining during the SSRT, passive film formed on the specimen surface may not be in a steady state and therefore it is difficult to investigate the role of stable passive film on SCC as suggested in Ref [6]. Under constant load conditions, SCC was not observed on the Mg-RE alloys (EV31A) within a reasonable time scale conducive in laboratory [6, 8]. In this study, SCC of EV31A, and WE43C in different heat treated conditions was investigated using U-bend type samples in 0.1 M NaOH with different chloride concentrations. The outer surface of the U-bend sample will have a constant tensile strain and inner surface will be under compressive strain whose magnitude is given by the relation:

$$\varepsilon = \frac{t}{2R+t} \qquad (1)$$

where ε = strain, t = thickness of sample, R = bend radius.

Using U-bend samples, threshold stress (σ_{SCC}) level for SCC cannot be determined but the susceptibility of different alloy compositions and heat treatment conditions can be ranked. Furthermore, the fracture mode and crack initiation behavior can be investigated using U-bend samples. This method is not only simple and economical (as multiple samples can be tested at the same time without requiring loading fixtures), but also the most severe load condition can be applied because large amounts of elastic and plastic strain are present [10]. Moreover, U-bend test is the most useful tool for studying different metals in different metallurgical conditions in different environments [10]. The test environment was selected based on our

previous work on the localized corrosion susceptibility of EV31A and WE43C alloys in alkaline solution containing chlorides [11, 12]. The results showed that the threshold chloride required for passive film breakdown in 0.1 M NaOH was 80 ppm for EV31A, and 200 ppm for WE43C. All the tests were duplicated or triplicated in some cases in order to check reproducibility. The variation in the results was within ±20%. The best representing results, that are reproducible are discussed in this report.

5.2 Experimental

5.2.1 Material and Characterization

The materials used in this investigation were Mg-Zn-Gd-Nd-Zr alloy (EV31A) and Mg-Y-Nd alloy (Elektron 43 or WE43C) in wrought 16-mm-thick plate form. Both Mg alloys were provided by Magnesium Elektron N.A. Inc. The specimens were cut in transverse to the rolling direction with the dimensions as shown in Figs. 5.1(a) – (b). They were machined close to the required thickness and ground to the required thickness (1.0 mm) at the last step. The as-received EV31A strips were solution heat-treated at 525 °C for 8 h and quenched in water at room temperature. This condition is referred to as ST. The solution treated EV31A strips were given two different aging treatments: 1) aging at 200 °C for 16 h, referred to as peak aging (PA), and 2) aging at 300 °C for 4 h which is referred to as overaging (OA). The as-received WE43C strips, also was solution heat-treated at 525 °C for 8 h and quenched in water at room temperature, which is referred to as ST. The WE43C-ST coupons were aged to two different conditions: peak aging at 200 °C for 168 h, and overaging at 300 °C for 2 h. All samples were cooled in air after aging. The strips were ground down to 1 mm thick with SiC paper up to 1500 grit, cleaned with acetone, dried in air before bending, and cleaned with acetone and dried in air again after bending. The bending was carried out in two stages following the procedure outline in ASTM G 30 [10] as shown in Figs. 5.2(a) – (b) with a bend radius of 10 mm. Stainless steel bolts and nuts, were used to maintain the legs of the U-bend parallel to each other. Plastic sheaths and washers were used for insulating the stainless steel bolts and nuts from galvanic coupling with the sample. The U-shape specimens were inspected for presence of any cracks with 10X magnifying glass after bending prior to SCC testing, and then they were assembled in the electrochemical cell. The specimens designated as “unstressed” were cut in transverse to the rolling direction with the dimensions of 1.6 cm × 2.5 cm × 0.3 cm. Heat treatment and

cleaning procedure were the same as that of the U-bend specimens. The unstressed specimens were ground with SiC paper up to 1500 grit for electrochemical measurement, and up to 1-micron diamond suspension for microstructural observation.

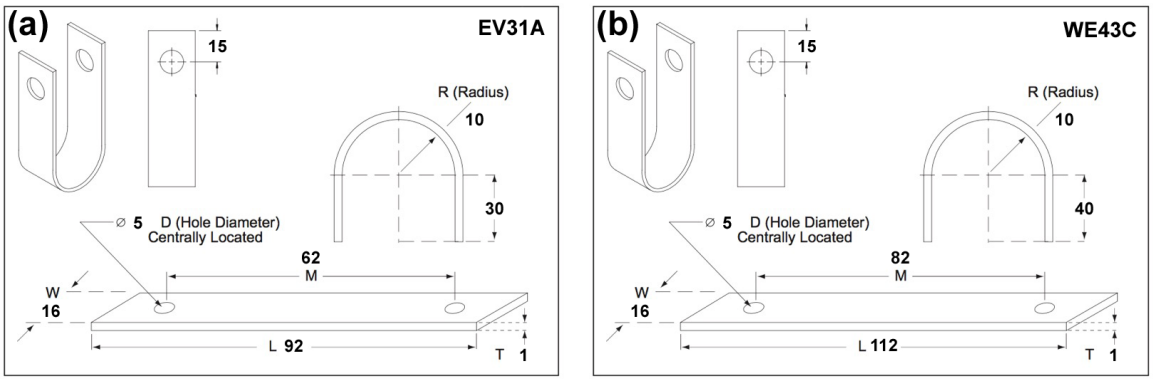

Fig. 5.1 U-bend dimensions of **(a)** EV31A, and **(b)** WE43C.

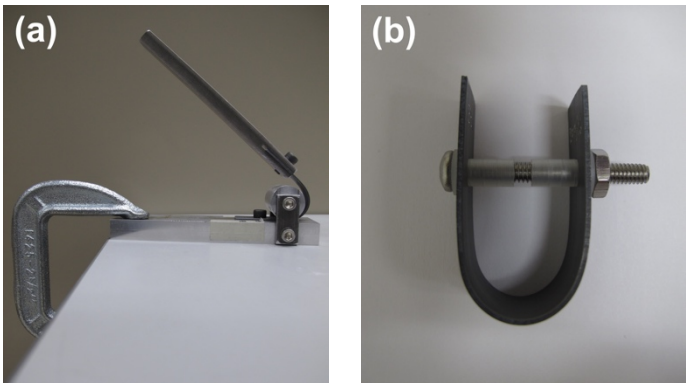

Fig. 5.2 Two-stage bending configuration; **(a)** first-stage to form approximately U-shape, and **(b)** second-stage to form test stress.

5.2.2 Electrochemical Tests and Environments

The U-bend specimens of EV31A and WE43C in all heat treatment conditions were assembled in 400 ml beakers filled with 250 ml of test solution and covered with lids. For the first 48 h, the open circuit potential (OCP) was measured by using a potentiostat (VersaSTAT MC, and VersaStudio software version 2.42.3 from Princeton Applied Research). Pt wire was the counter electrode, KCl-saturated Ag/AgCl (199 mV vs SHE) was the reference electrode, and the sample was the working electrode. After 48 h, the potentiostatic connection was removed from the electrochemical cell, and the OCP was measure twice a day by using a multimeter (Fluke Model 26III) with KCl-saturated Ag/AgCl as the reference electrode. The

OCP measurements continued until the samples failed. SCC tests were carried out on the U-bend samples by applying anodic potentials. SCC tests in cathodic bias was carried out by applying a cathodic current density of -10 mA/cm^2.

Cyclic polarization was carried out on both U-bend and unstressed samples by scanning the potential from 0 V vs OCP to 2.5 V vs reference electrode at scan rate of 1 mV/s. The scan direction was reversed when the potential reached 2.5 $V_{Ag/AgCl}$ or the transpassive current density reached 1 mA/cm^2 (whichever occurred first). The electrolytes were 0.1 M NaOH (pH 13.5) with different chloride concentrations (80, 100, 200 ppm Cl^- in the form of NaCl). Deionized (DI) water (resistivity 18.2×10^6 Ohm-cm) obtained from a water purifier (MilliPore Model: Milli-QPF Plus) and reagent grade chemicals were used for preparing the test solutions.

5.2.3 Microstructure and Fractography

The unstressed specimens were etched to reveal microstructure with glycol etchant containing 10 ml HNO_3, 24 ml DI water, 75 ml ethylene glycol. The SCC tested U-bend specimens were rinsed with DI water, and ultrasonic cleaned with acetone. The optical microscopy was conducted by using an OLYMPUS PMG3 optical microscope, and the scanning electron microscopy (SEM) was conducted by using a LEO SUPRA 35VP with the energy-dispersive X-ray spectroscopy (EDS) detector. Gracing angle X-ray diffraction patterns were obtained using a Rigaku Smartlab 3 kW with Cu kα X-ray tube operated to 40 kV and 44 mA, where the incident angle of the X-rays was 0.5° with respect to the sample surface.

5.3 Results and Discussion

5.3.1 Microstructure

Figs. 5.3(a) – (e) show optical microstructures of EV31A and WE43C in unstressed conditions. Fig. 5.3(a) shows the as-received specimen of EV31A with fine grains and texture across the sample. Grain size varied between 10 and 14 μm. The secondary phases were identified as $Mg_{12}Nd$, Mg_3RE, and $Mg_{41}Nd_5$ [11]. Grain size of peak-aged specimen of EV31A increased after solution treatment and was in the range of 20 to 33 μm as shown in Fig. 5.3(b). Texture was still present, but it decreased compare to the as-received condition. The secondary phase found in the peak-aged condition was β'' which had nanoscale size, and could not be detected by optical microscope [11]. This phase caused peak hardness of the specimen.

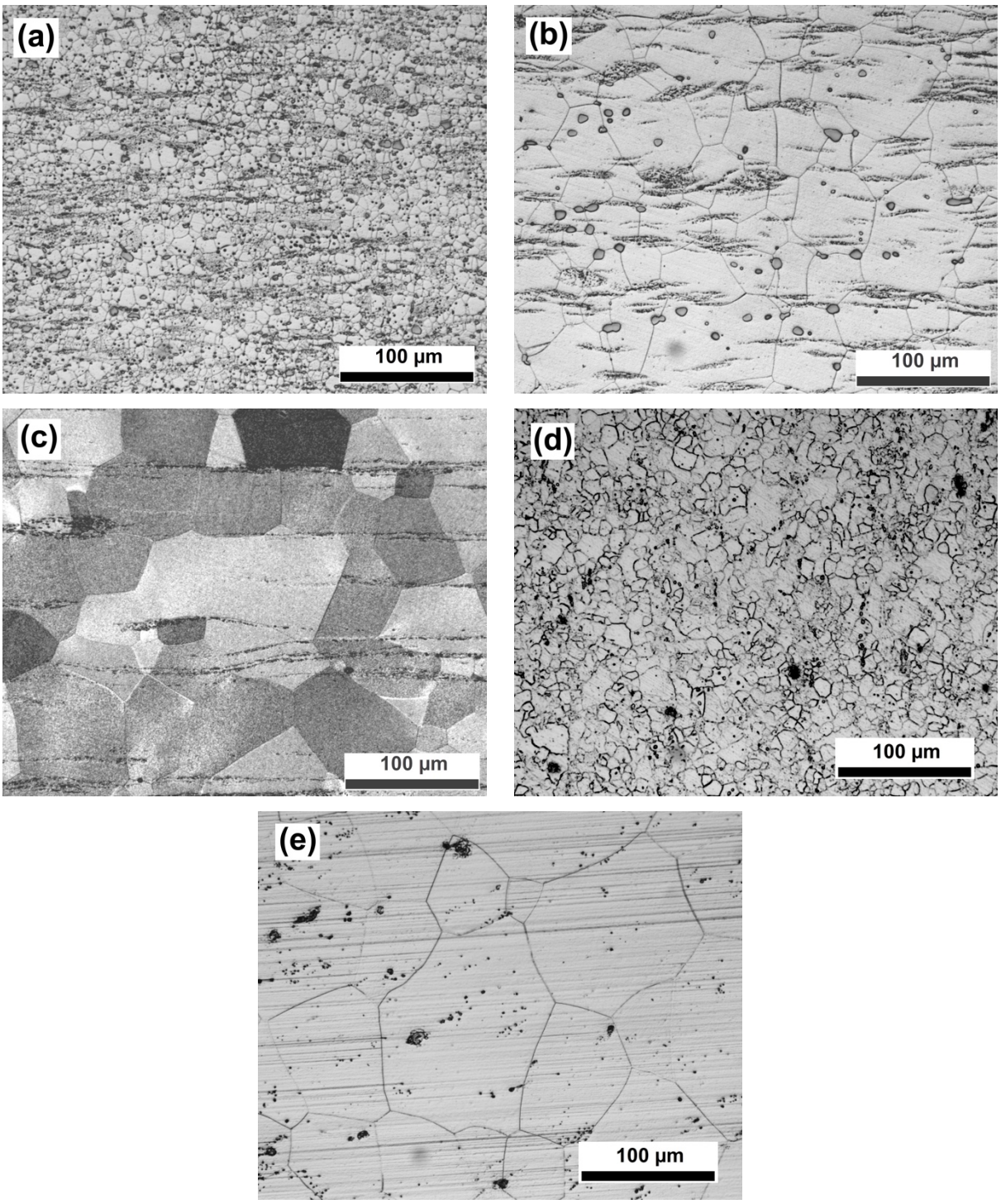

Fig. 5.3 Optical microstructures of EV31A and WE43C in unstressed condition; **(a)** as-received of EV31A, **(b)** peak-aged of EV31A, **(c)** overaged of EV31A, **(d)** as-received of WE43C, and **(e)** peak-aged of WE43C.

Microstructure of EV31A in overaged condition is shown in Fig. 5.3(c). Grain size of OA samples varied between 20 and 30 µm. The etched-dark grains were influenced by the high volume fraction of the cellular-type β phase (Mg_3RE) [11]. Fig. 5.3(d) illustrates microstructure

of as-received WE43C specimen. Fine grain size between 9 and 16 μm and texture were observed in this condition. The XRD revealed the secondary phases as $Mg_{12}Nd$, $Mg_{24}Y_5$, $Mg_{41}Nd_5$, and Mg_3Gd [12]. Microstructure of WE43C in peak-aged condition (WE43C-PA) is shown in Fig. 5.3(e). The grain size of the peak-aged sample was significantly larger than that of as-received. The grain growth occurred during the solution treatment and the textured feature completely disappeared in WE43C-PA, in contrast to the microstructure of EV31A-PA.

5.3.2 Open Circuit Potential (OCP)

Figs. 5.4(a) – (b) show open circuit potential (OCP) plots of the specimens in 0.1 M NaOH with 80 ppm chloride concentration for the first 48 hours, and after 48 hours, respectively. Table 5.1 summarized the initial, the most positive, final OCPs from the plots in Figs. 5.4(a) and (b), time at which crack first observed, and time to failure (that cracks propagated throughout the width of the specimen and total failure of sample). From Fig. 5.4(a), OCP of the unstressed peak-aged specimen increased significantly from -1.64 $V_{Ag/AgCl}$ to -1.16 $V_{Ag/AgCl}$ for the first 25 minutes then decreased steeply to -1.52 $V_{Ag/AgCl}$ for the next 7 minutes. This increase-decrease fluctuation occurred again, then the OCP increased sharply to -0.86 $V_{Ag/AgCl}$ at hour 2. After the significant fluctuations, the OCP gradually increased to -0.77 $V_{Ag/AgCl}$ at hour 26. From 26 to 48 hours, the OCP fluctuated in the range of -0.79 and - 0.94 $V_{Ag/AgCl}$. Marquis and co-worker [13] observed this behavior in WE43 Mg alloy immersed in 3.5 wt.% NaCl. They attributed the increase in the OCP to the formation of passive film, and the decrease in the OCP to the passive film break-down. The subsequent increase of OCP was associated with the repair of the ruptured passive film. After recovery, the film became thicker [13]. Similar OCP fluctuations were reported in alkaline solutions for the Mg-Al alloys without chloride in unstressed samples [14]. Potential fluctuations were observed in the unstressed Mg-RE samples in 0.1 M NaOH without chloride addition [15]. The magnitude of fluctuations was not affected by the addition of 80 ppm chloride.

For the U-bend EV31A, OCP of the as-received specimen increased significantly from -1.39 $V_{Ag/AgCl}$ to -0.71 $V_{Ag/AgCl}$, and two small bumps were present at the first 5 hours of exposure. After that, the OCP was almost constant at -0.62 $V_{Ag/AgCl}$ until 20 hours. The OCP decreased sharply after 20 hours to -1.30 $V_{Ag/AgCl}$, and increased steeply again to -0.88 $V_{Ag/AgCl}$

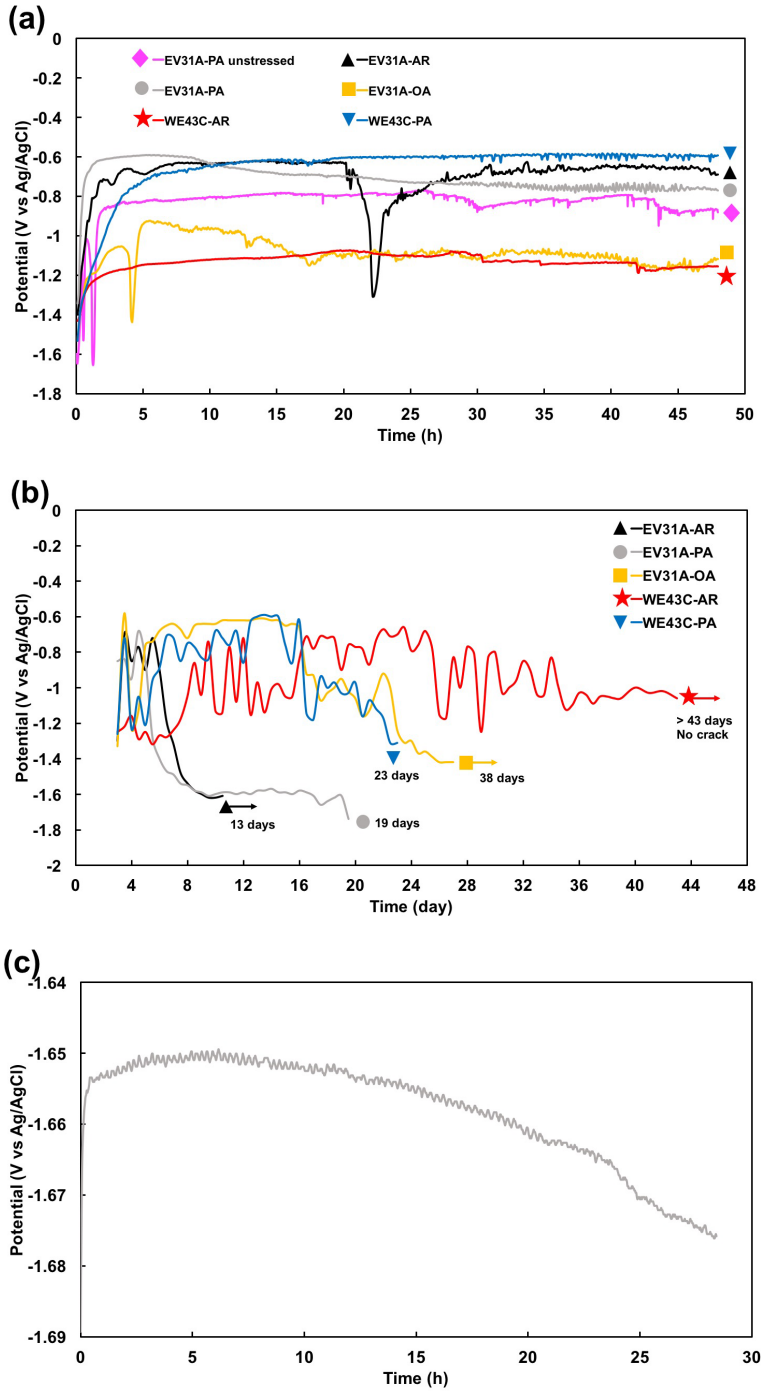

Fig. 5.4 Open circuit potential (OCP) plots of the specimens in 0.1 M NaOH with 80 ppm chloride concentration; **(a)** the first 48 h, **(b)** after 48 h, and **(c)** OCP of EV31A as-received after cracks showed. AR as-received, PA peak-aged, OA overaged.

Table 5.1 Summary of the initial, the most positive, final OCPs from the plots in Fig. 5.4(a) and (b), and time to crack completely.

Material		Initial OCP ($V_{Ag/AgCl}$)	Most positive OCP ($V_{Ag/AgCl}$)	Final OCP ($V_{Ag/AgCl}$)	Time to crack initiation (day)	Time to crack completely (day)
EV31A	PA unstressed	-1.62	-0.77	N/A	N/A	N/A
	AR	-1.39	-0.63	-1.61	9	13
	PA	-1.34	-0.59	-1.74	19	19
	OA	-1.53	-0.92	-1.42	26	38
WE43C	AR	-1.43	-0.66	-1.06	N/A	No crack (> 43)
	PA	-1.53	-0.59	-1.31	23	23*

* WE43C-PA took 8 h from crack initiation to completely crack at day 23.

within 3 hours. Even though the OCP slightly increased after this point, it showed the narrow range of fluctuation until 48 hours. This fluctuation could have occurred because of pits initiation on the sample's arms, at the solution/air interface. The overaged specimen spent more time to form a thicker passive layer compared to the as-received sample. From Fig. 5.4(a), OCP of the overaged specimen increased from -1.53 to -1.05 $V_{Ag/AgCl}$, during the first 3 hours and then decreased steeply to -1.43 $V_{Ag/AgCl}$. When the passive film repaired, the OCP moved upward to -0.92 $V_{Ag/AgCl}$, and fluctuated as shown in Fig. 5.4(a). The fluctuations could possibly be attributed to initiation of pitting at the solution/air interface on the arms (unstressed part) of the U-bend sample. No pits were observed on the bent (strained) region. The OA samples showed the most active OCP values among the samples tested. Interestingly, peak-aged specimens of EV31A, WE43C in as-received and peak-aged conditions showed similar OCP profile without significant fluctuation. The OCP of EV31A in peak-aged condition increased significantly from -1.34 to -0.6 $V_{Ag/AgCl}$ and was constant for 9 hours. The OCP gradually decreased to -0.77 $V_{Ag/AgCl}$ when it reached 48 hours. The increase of OCP in WE43C as-received sample at the initial stage is quite low compared to the OCP of both EV31A and WE43C in peak-aged conditions. The OCP of WE43C as-received specimen moved in positive direction from -1.43 $V_{Ag/AgCl}$ to -1.20 $V_{Ag/AgCl}$, then slightly increased to -1.07 $V_{Ag/AgCl}$ at hour 20. From this point to hour 48, the OCP profile showed fluctuations due to pitting corrosion at the arms of the sample at the solution/air interface. For the peak-aged WE43C, the OCP increased significantly from -1.53 $V_{Ag/AgCl}$ to -0.79 $V_{Ag/AgCl}$ for the first 3 hours of exposure. Then the OCP gradually increased to -0.61 $V_{Ag/AgCl}$ for the next 11 hours, and was almost constant until hour 48.

Fig. 5.4(b) shows the OCP vs time plots recorded at every 12 hours during the SCC tests of U-bend samples after initial 48-h continuous recording. EV31A as-received specimen showed that the OCP fluctuated in the range of -1.30 $V_{Ag/AgCl}$ and -0.7 $V_{Ag/AgCl}$ for 3 days (day 5 of total exposure). Then the OCP decreased significantly for the next 3 days before the OCP became constant to -1.6 $V_{Ag/AgCl}$. At the constant potential region, many small cracks were observed with the average crack length of 3.5 mm. After 12 hours, the average crack length became 6.1 mm, which showed a crack growth rate of $\sim 6 \times 10^{-8}$ m/s. This crack velocity was similar to the order of magnitude (2.2×10^{-8} m/s) reported for the case of galvanically induced crack growth by Atrens' group [16]. At this stage, the OCP was recorded continuously using a potentiostat. The plot of OCP is shown in Fig. 5.4(c). A saw-tooth like potential fluctuations were observed at the crack propagation stage. Each fluctuation wave could possibly be associated with crack increment. The width of each fluctuation peak varied between 10 and 15 minutes, and the height of the peak varied between 0.9 and 1.5 mV. The width and amplitude of the potential fluctuations were consistent which implied that each fluctuation could correspond to a constant magnitude of crack increment. The potential decreased continuously during the final crack growth stage. The EV31A as-received sample completely cracked in 13 days of exposure to the 80 ppm chloride solution as summarized in Table 5.1. A second specimen cracked in 14 days. The OCP profile of EV31A peak-aged specimen showed similar characteristic to the as-received specimen. The fluctuation of OCP for the first 2 days (day 4 of total exposure) was between -0.95 and -0.68 $V_{Ag/AgCl}$. The OCP moved downward (more negative direction) from -0.68 $V_{Ag/AgCl}$ to -1.60 $V_{Ag/AgCl}$ within 3 days, then the OCP was constant and cracks were observed. Before the specimen completely cracked, the OCP decreased from -1.61 to -1.74 $V_{Ag/AgCl}$. The peak-aged specimen of EV31A cracked in 19 days of exposure, while the second specimen cracked in 16 days. The EV31A overaged specimen showed extreme fluctuation of OCP (-1.33 to -0.58 $V_{Ag/AgCl}$) during the first 2 days, and became almost constant at -0.6 $V_{Ag/AgCl}$ for 11 days. The OCP then fluctuated in negative direction to -1.42 $V_{Ag/AgCl}$ and stayed constant until cracks propagated throughout the width of the specimen at day 38. For the WE43C as-received specimen, the OCP showed periodic extreme and regular fluctuations after 48 hours of exposure. The negative and positive OCPs after 48 hours fluctuated in the range of -1.32 and -0.66 $V_{Ag/AgCl}$. The fluctuations could be attributed to the corrosion on the arms of the specimen above the aqueous solution whereas the U-bend area

under the solution did not show any evidence of pitting corrosion or cracks due to SCC. The specimen did not show stress corrosion crack initiation for more than 43 days and the experiment was terminated after 43 days of exposure. The peak-aged specimen of WE43C showed the OCP plot more or less similar to that of EV31A specimen in overaged condition. However, the OCP showed more number of fluctuations in the range of -0.86 and -0.59 $V_{Ag/AgCl}$ instead of a plateau profile as observed in the overaged specimen of EV31A. The WE43C in peak-aged condition cracked into 2 pieces in 23 days. The second sample failed in 25.5 days. The crack growth rate of the two WE43C peak-aged specimens approximated 5.56×10^{-7} m/s (~8 h from crack initiation to completely crack).

In terms of crack initiation and crack propagation, it could be seen from Table 5.1 that EV31A in overaged condition had the longest time for crack initiation and crack propagation which were 26 and 38 days, respectively. Even though the peak-aged specimens of both EV31A and WE43C had longer time for crack initiation than EV31A as-received specimen, crack propagation rates were much faster than that of EV31A as-received condition. Crack growth rate depends on heat treatment conditions which are related to mechanical properties such as hardness. Higher the hardness [11, 12] the faster was the crack growth rate.

Figs. 5.5(a) and (b) show OCP plots of the EV31A specimens in as-received condition in 0.1 M NaOH with different chloride concentrations for the first 48 hours, and after 48 hours, respectively. In 100 ppm Cl^- solution, two small fluctuations due to formation-breakdown-repair of passive film were present on the plot with the -1.49 $V_{Ag/AgCl}$ of initial OCP. At the third time of repassivation, the OCP was constant for around 1.5 hours, increased again to -0.48 $V_{Ag/AgCl}$, and was almost constant at that potential. The specimen immersed in 200 ppm Cl^- solution passivated continuously as the potential increased from -1.51 $V_{Ag/AgCl}$ to -0.81 $V_{Ag/AgCl}$ within 3 hours, and the OCP fluctuated for approximately 2.5 hours. The OCP then plunged to -1.39 $V_{Ag/AgCl}$, and moved upward again to -0.72 $V_{Ag/AgCl}$. After that potential recovery, the OCP fluctuated in a narrow range and gradually decreased. After 40 hours, the fluctuation of OCP was in a higher amplitude than that observed in the earlier period. At the end of 48 hour exposure, localized corrosion at the solution/air interface was significant at the arms of the specimen. After 48 hours of the measurement by potentiostat, the OCP was recorded manually of the specimens in 80, 100, 200 ppm Cl^- electrolyte are shown in Fig. 5.5(b). The OCP of the sample in the 100 ppm Cl^- solution fluctuated for the whole period of the experiment. Even

though the OCP of the sample in the 200 ppm Cl^- solution did not significantly fluctuate for the whole period of the experiment as in 100 ppm Cl^-, localized corrosion was observed on the arms of the specimen at the solution/air interface line. Interestingly, the as-received of EV31A specimens in 100 and 200 ppm Cl^- solution did not show any cracks at the bent (strained) regions of the U-bend sample which were immersed deep in the solution.

Figs. 5.5(c) and (d) show OCP plots of the WE43C specimens in as-received condition in 0.1 M NaOH with different chloride concentrations for the first 48 hours, and after 48 hours, respectively. From Fig. 5.5(c), the OCP of the specimen in 100 ppm Cl^- showed the fluctuation pattern due to formation-breakdown-repair of passive film without the fluctuation caused by localized corrosion. Three and a half loops of fluctuations could be observed during the first 48 hours. When chloride concentration was increased to 200 ppm, the fluctuation of OCP due to localized corrosion could be observed after 5 hours of exposure while the fluctuation for the first 5 hours could be attributed to formation-breakdown-repair of passive film. After 48 hours, the OCP fluctuations of the specimens in 100 and 200 ppm Cl^- showed featureless pattern. Interestingly, WE43C in as-received condition in 100 and 200 ppm Cl^- showed similar resistance to SCC to the specimen in 80 ppm Cl^- as discussed early.

From the OCP profile, it could be noticed that the OCP of the specimens, which failed by SCC, decreased when cracks initiated and propagated. On the other hand, the OCP of the specimens which were susceptible to localized corrosion without SCC showed the fluctuating behavior without the monotonously decreasing trend. This observation could be applied to in-service monitoring of components.

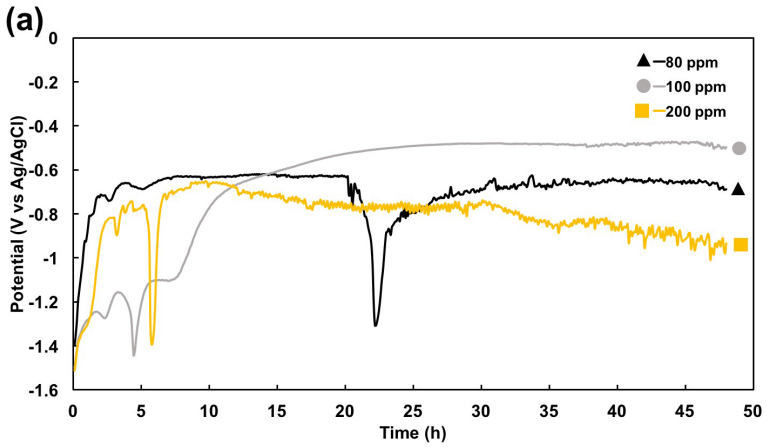

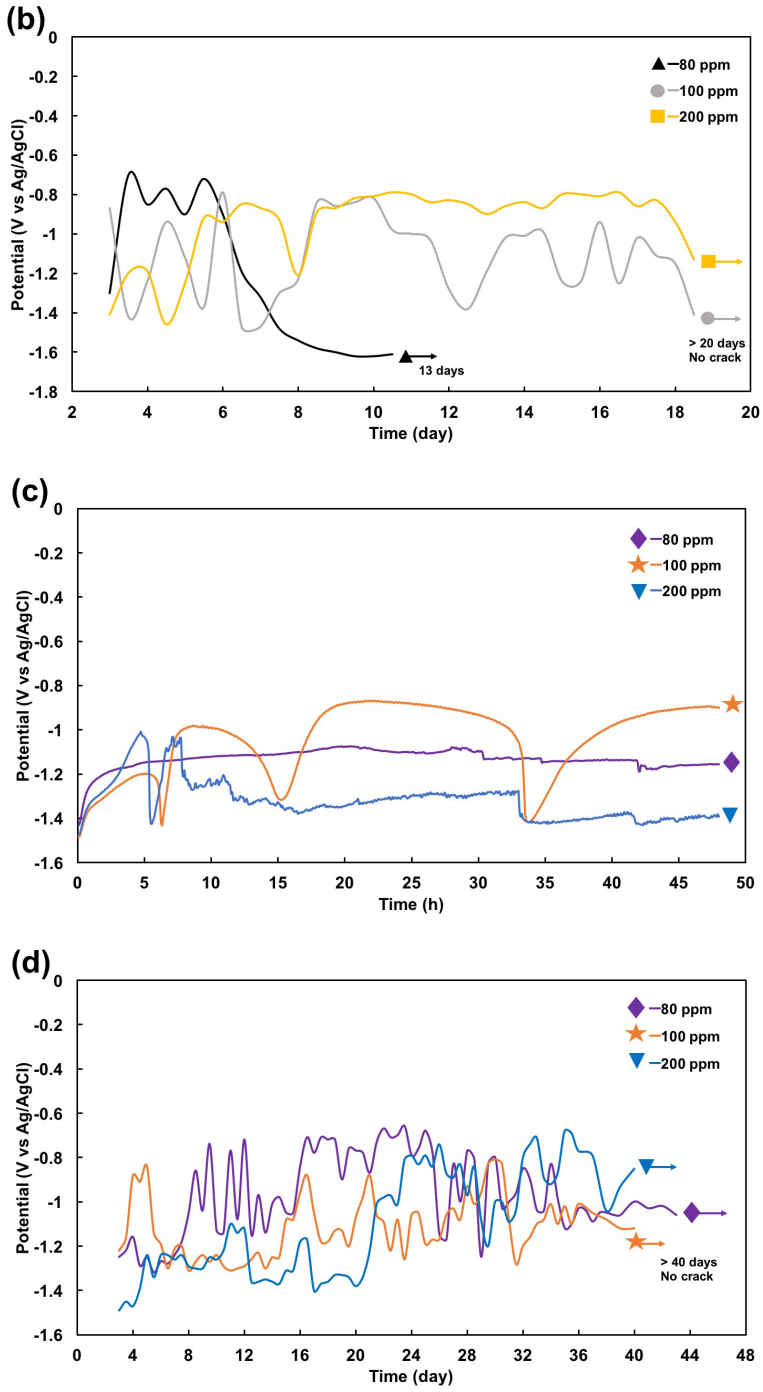

Fig. 5.5 OCP plots of the specimens in as-received condition in 0.1 M NaOH with different chloride concentrations; **(a)** EV31A at the first 48 h, **(b)** EV31A after 48 h, **(c)** WE43C at the first 48 h, and **(d)** WE43C after 48 h.

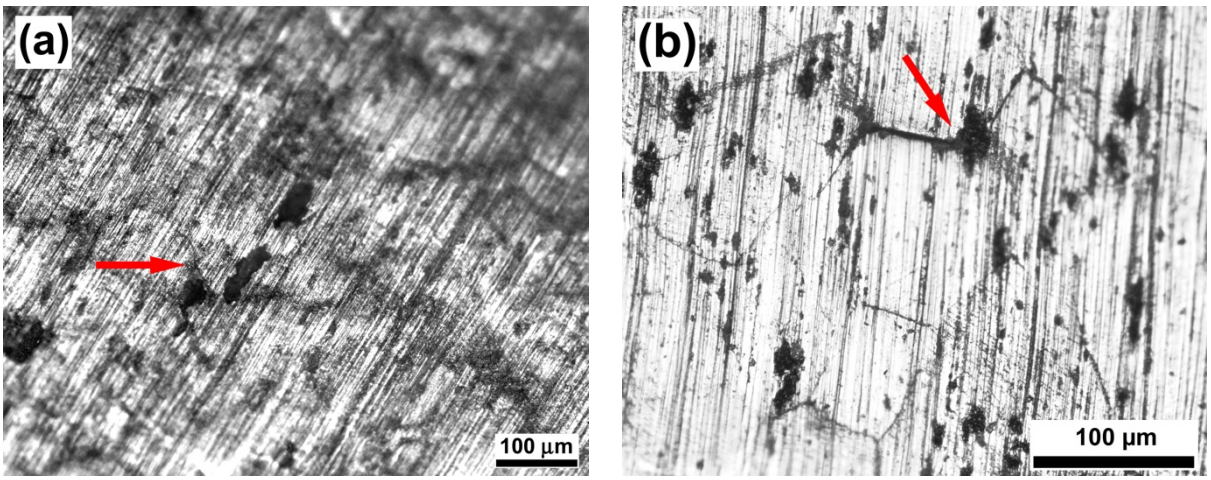

Fig. 5.6 Optical micrograph; **(a)** EV31A overaged, and **(b)** WE43C peak-aged.

5.3.3 Fractography at OCP

Figs. 5.6(a) – (b) show optical micrographs of EV31A in overaged condition and WE43C peak-aged condition, respectively. From Fig. 5.6(a), it could be seen that there were cracks initiated at pits. It is not clear from the micrograph that if cracks propagated along grain boundaries. However, cracks on the area around localized corrosion were observed as intergranular. Cracks also initiated at the localized corrosion and propagated along grain boundaries in WE43C peak-aged specimen (Fig. 5.6(b)). Our earlier work on localized corrosion of EV31A [11] and WE43C [12] in different heat treatment conditions exposed to 500 ppm Cl^- + 0.1 M NaOH showed that pit initiation occurred within spherical secondary phase particles, that were enriched in Zr. The localized corrosion observed on the U-bend specimens could also be attributed to the preferential dissolution of secondary particles. The intergranular cracking observed on the samples indicated possible SCC mechanism could be due to anodic dissolution of regions adjacent to the secondary phases [3]. Figs. 5.7(a) – (g) show features of the fractured surface of EV31A in as-received condition. Fig. 5.7(a) shows the fractured surface at a low magnification where four different morphologies are seen in each segment with dimensions around 145, 525, 55, and 100 µm across the thickness of the specimen. Fig. 5.7(b) shows the magnified view of outer fiber region (top 145 µm deep). Secondary cracks are seen on the surface that was covered with a layer of corrosion product. The second region showed transgranular crack growth due to SCC with the localized secondary cracks as shown in Fig. 5.7(c). The length of this region was around 525 µm. The third region was predominantly ductile with dimples and decohesion of secondary particles (Fig. 5.7(d)). This

region showed crack growth mainly by mechanical stress because around 3/4 of the cross-sectional area was already affected by SCC. This part was around 55 μm long. The mechanical fracture in the third part could lead to featureless smooth fracture surface which was the characteristic of the last part as shown in Fig. 5.7(e). Plastic deformation was also observed on the smooth surface. This area was around 100 μm long. Fig. 5.7(f) shows planar view of the outer surface of the U-bend sample that reveals mixed mode (primary intergranular cracks along with transgranular secondary cracks) cracking morphology. The outer surface was covered with $Mg(OH)_2$ film as seen in Fig. 5.7(g) at high magnification, and secondary cracks due to SCC could be seen.

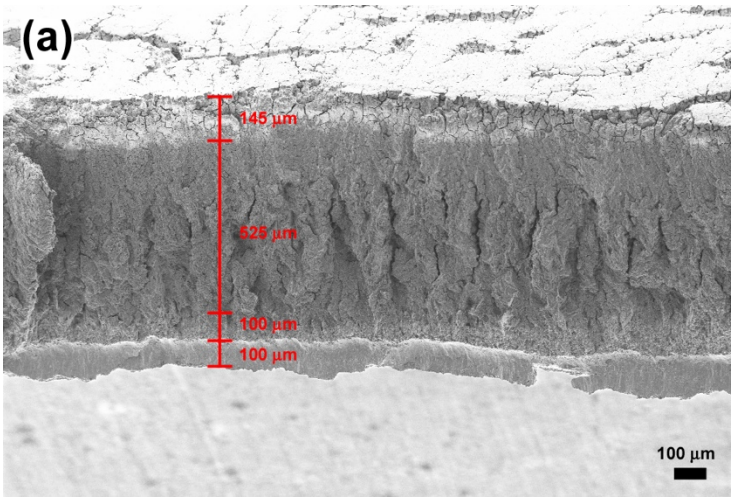

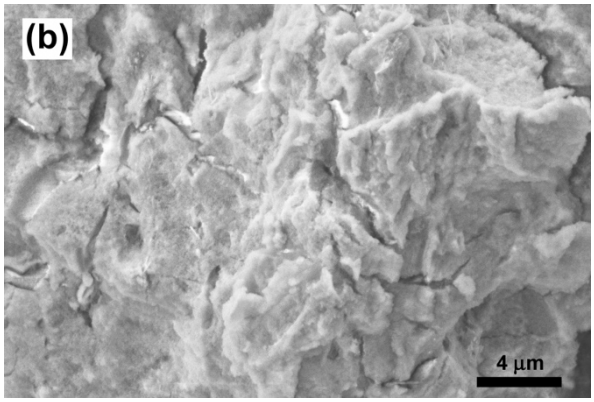

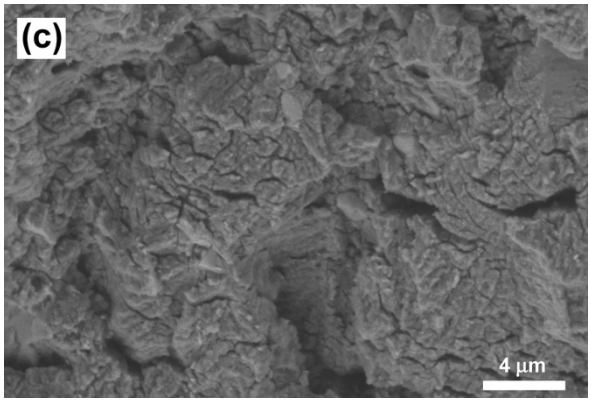

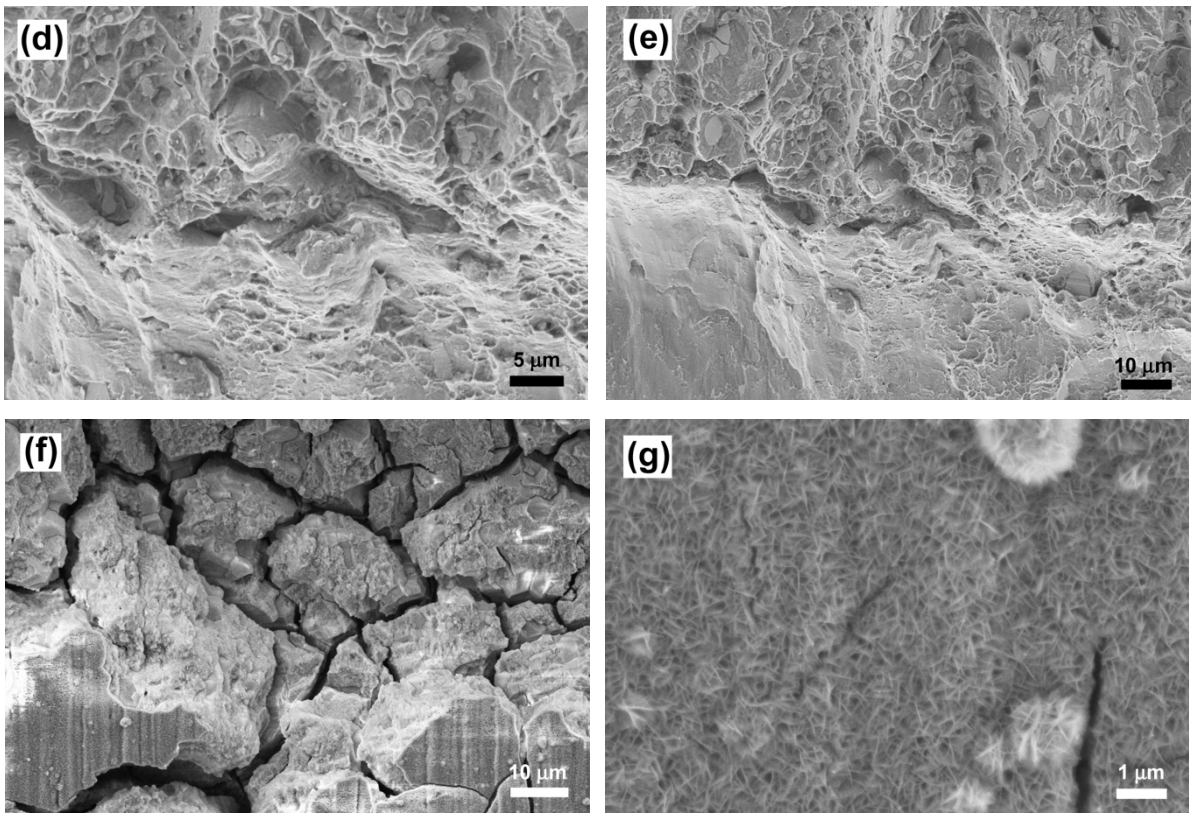

Fig. 5.7 Fracture feature of EV31A in as-received condition; **(a)** cross sectional view showed 4 different fracture features, **(b)** top section of (a), **(c)** second section of (a), **(d)** third section of (a), **(e)** bottom section of (a), **(f)** top view of tension side surface, and **(g)** passive film on the surface in (f). Noted that the length of each section in Fig. 5.7a was not the actual length, but it could be close to the actual length. The measurement gives an idea of the proportion of each fracture feature.

Figs. 5.8(a) – (d) show fracture feature of EV31A in peak-aged condition. The fracture showed both transgranular and intergranular modes, and secondary cracks were also observed as seen in Fig. 5.8(a). Attack on specific crystallographic planes that resembled transgranular morphology could be seen in Fig. 5.8(b) (marked by arrow). Figs. 5.8(c) – (d) show top view of the tension side surface. The characteristic of fracture was similar to the EV31A as-received specimen. The fracture morphology indicated that the SCC mechanism could be associated with film rupture – dissolution as the major cause of cracking and the cracking at specific crystallographic planes indicated possible hydrogen adsorption on certain planes that decreased the surface energy [17].

Figs. 5.9(a) – (b) show crack propagation on outer (tensile) surface of the EV31A overaged U-bend sample. The flake morphology of $Mg(OH)_2$ formed on the surface of the overaged (Fig. 5.9(a)) specimen appeared to be less dense than that observed on the as-received specimen. However, the overall thickness of the surface layer was significantly higher than that

formed on the other heat treated conditions. The thick surface layer formed on the overaged specimen could be attributed to the longer incubation time required for crack initiation than that required for the as-received specimen. The first crack of the as-received specimen was observed on day 9 with crack length of 3.5 mm, while for the overaged specimen a 2 mm long of crack was observed on day 26. Fig. 5.9(b) shows significant dissolution of the fracture surface and deposition of corrosion products. The time taken for crack growth was significantly long during which time the cracked surfaces were exposed to the test solution and allowing the corrosion products to re-precipitate. It was noticed that even though crack propagated throughout the width of the U-bend specimen, the specimen did not crack into 2 pieces. In addition, primary crack on the compressive surface was present at the center around 1/3 of the surface width.

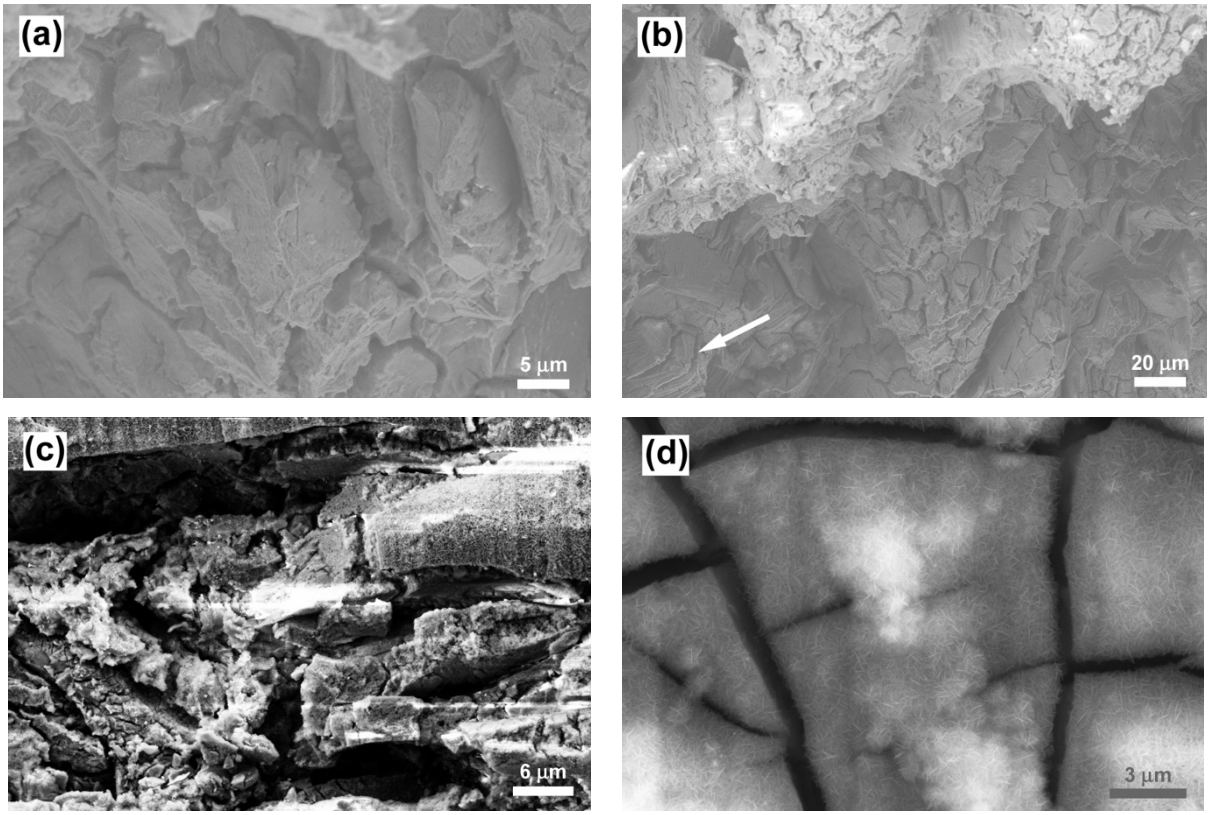

Fig. 5.8 Fracture feature of EV31A in peak-aged condition; **(a)** transgranular and intergranular mode, and secondary cracks, **(b)** specific crystallographic planes attack (marked by arrow), **(c)** top view of tension side surface, and **(d)** passive film on the surface in (c).

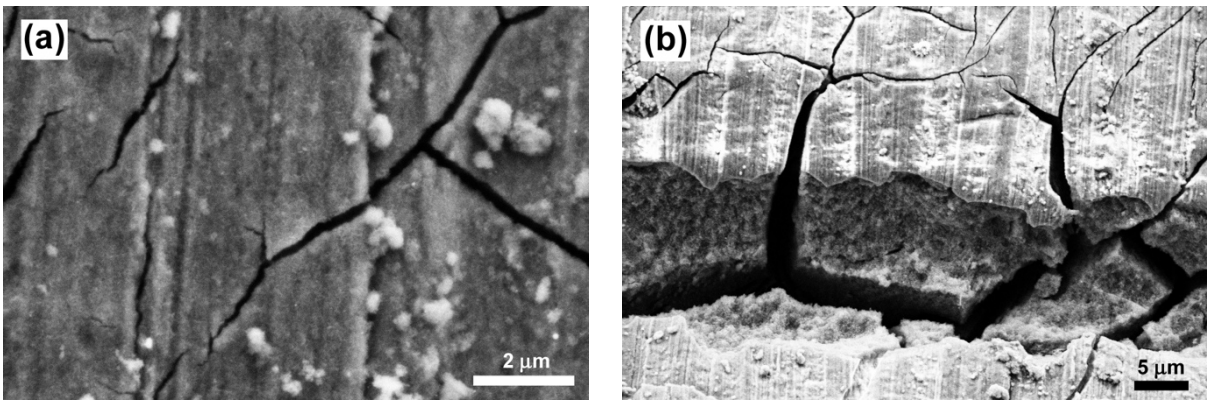

Fig. 5.9 Crack propagation on top of the tension side surface of the EV31A overaged sample; **(a)** passive film on crack surface, and **(b)** crack surface at low magnification.

Figs. 5.10(a) – (e) show fractograph of WE43C in peak-aged condition. The cross-sectional fracture surface had two different fractographic features as seen in Fig. 5.10(a). The upper section which was the tension side of the U-bend showed predominantly intergranular with preferential attack on specific crystallographic planes as seen in Fig. 5.10(b). Some of the fracture planes appeared featureless, possibly indicating {0001} basal planes as cleavage planes where cracks propagated. Adjacent to those cleavage planes, fine parallel crystallographic planes running almost perpendicular to the basal planes could be observed as seen in Fig. 5.10(b). These planes could be {10-1X} fluted planes similar to that reported by Trevena and Lynch [18]. The deposition of corrosion product could be observed on the fractured surface beneath the outer fiber. Minor cracks were observed running perpendicular to the primary crack growth direction as shown in Fig. 5.10(c). Fig. 5.10(d) shows predominantly transgranular mode at the region closer to the original neutral axis of the U-bend specimen, and smooth fracture surface with local plastic deformation was observed at the final fracture surface where mechanical overload played a significant role. Fig. 5.10(e) shows the crack initiation sites on the top surface of the outer fiber of the U-bend specimen. The crack initiation occurred at the intersection of pit and dislocations emerging from slip steps indicated by an arrow. Overall, SCC of the peak-aged WE43C specimen at open circuit potential in alkaline chloride solution occurred in two stages viz., stage 1: crack initiation which was controlled by the film rupture and dissolution at the slip steps; and stage 2: crack propagation which occurred by reduction in cohesive strength of crystallographic planes by hydrogen adsorption.

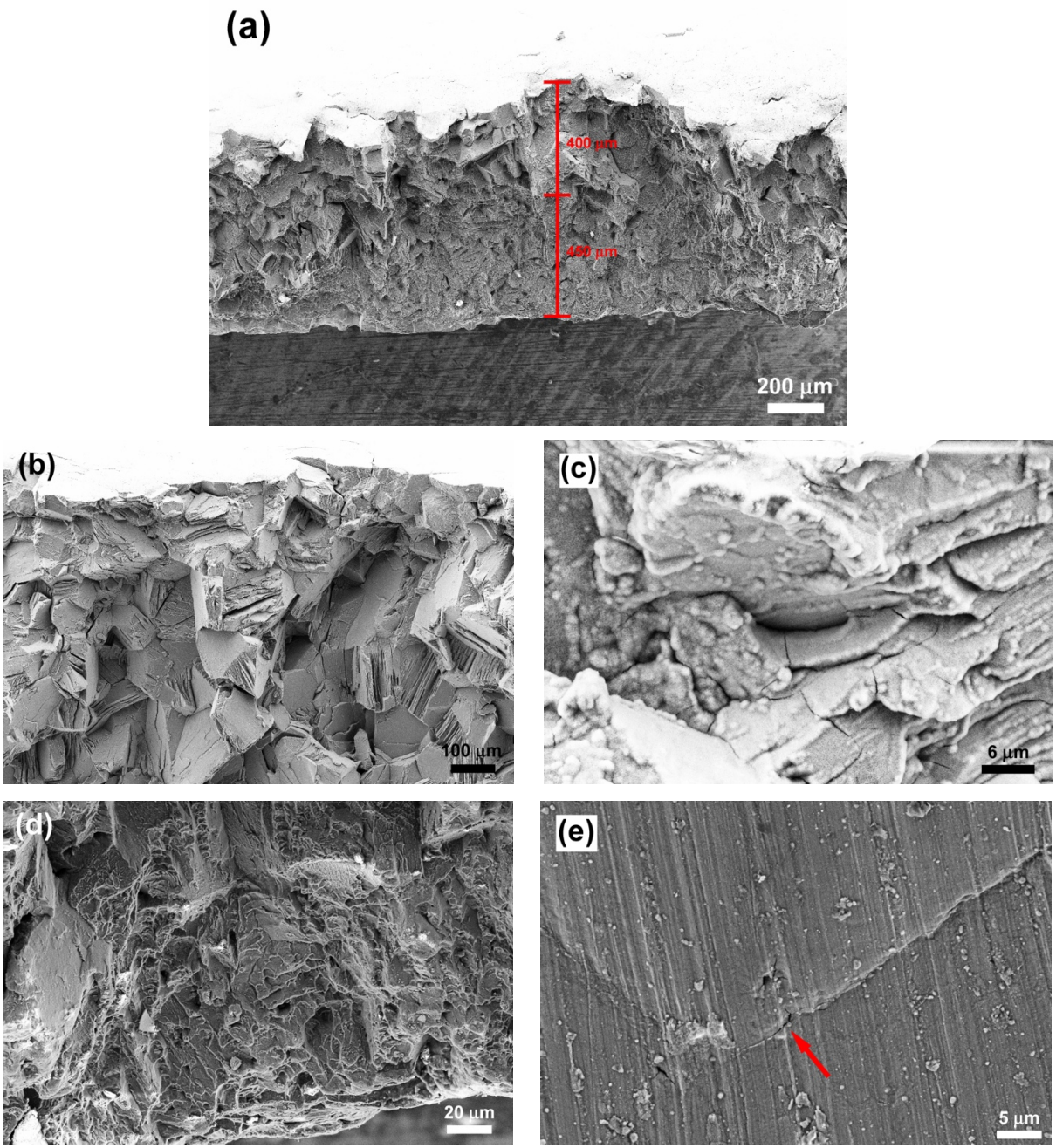

Fig. 5.10 Fractures of WE43C in peak-aged condition; **(a)** two different fracture features, **(b)** upper section, **(c)** shallow level under tension surface, **(d)** lower section, and **(e)** crack propagation at the edge of slip step region. Noted that the length of each section in Fig. 5.10a was not the actual length, but it could be close to the actual length. The measurement gives an idea of the proportion of each fracture feature.

5.3.4 Cyclic Polarization

In order to understand the relation between the stability of passive layer and the SCC susceptibility, cyclic polarization was carried out on the U-bend specimens and the results were compared with the polarization behavior of the unstressed coupons. Figs. 5.11(a) – (b) show cyclic polarization plots of EV31A as-received and WE43C peak-aged specimens with and without applied stress in 80 ppm Cl^- + 0.1 M NaOH solution. Table 5.2 summarizes cyclic polarization results from Figs. 5.11(a) – (b). From Fig. 5.11(a), it can be seen that transpassive potential and pitting protection potential of the unstressed EV31A as-received specimen were higher than that of the stressed specimen. The passive current density of the unstressed specimen was two decades lower than the stressed specimen. The polarization results indicated that the passive film of the unstressed specimen was more protective and stable than the passive film of stressed specimen. It could be observed from Figs. 5.4(a) and 5.11(a) that after passive film broke down the specimen tried to repassivate, but the film was not able to recover which lead to initiation of pits. When the OCPs of EV31A as-received specimen from Figs. 5.4(a) and (b) were superimposed on Fig. 5.11(a), the highest OCP value recorded was in the passive range just negative to the pitting protection potential of the U-bend specimen; whereas the potential recorded during the crack growth period was in the cathodic region of the cyclic polarization plots. The transpassive potential and pitting protection potential of WE43C peak-aged specimens with and without applied stress were similar to each other, but the unstressed specimen showed lower passive current density. The passivation behavior from cyclic polarization plot correlated with the plot of OCP in Fig. 5.4(a). When the OCPs from Figs. 5.4(a) and (b) were superimposed on Fig. 5.11(b), they were at the anodic region, while the potential recorded during the crack growth stage coincided with the Flade potential of the stressed sample.

Table 5.2 Cyclic polarization results from Fig. 5.11(a) – (b).

Material		$E_{Transpassive}$ ($V_{Ag/AgCl}$)	E_{Prot} ($V_{Ag/AgCl}$)	Passive current density ($\mu A/cm^2$)
EV31A	unstressed	1.64	1.27	2.50
	stressed	0.73	-0.34	56.46
WE43C	unstressed	1.59	1.35	3.97
	stressed	1.57	1.52	16.66

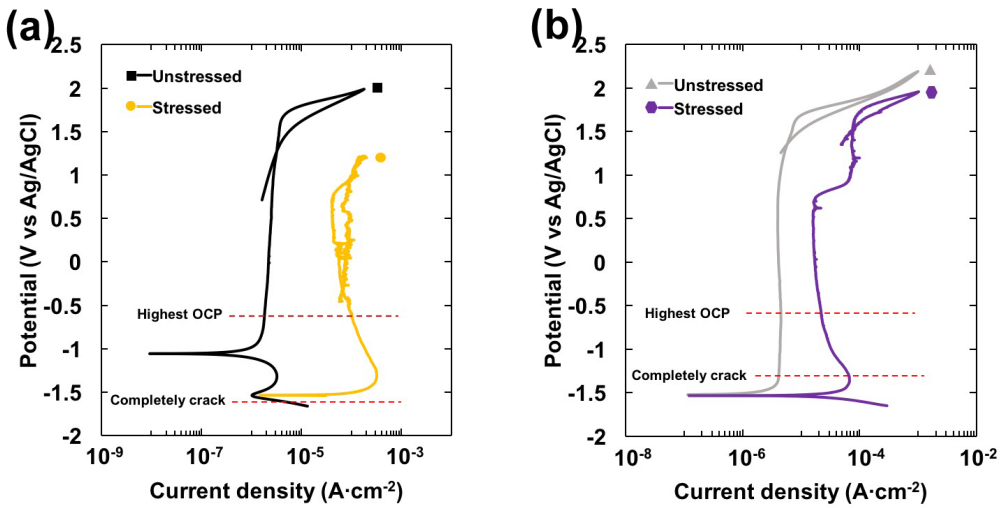

Fig. 5.11 Cyclic polarization plots of the specimens with and without applied stress in 80 ppm Cl^- + 0.1 M NaOH solution; **(a)** EV31A as-received, and **(b)** WE43C peak-aged.

5.3.5 Failure at SCC Susceptible Zones

Fig. 5.12 illustrates the schematic polarization curve showing SCC susceptible zones and hydrogen induced cracking (HIC) zone [19]. At the zone 1, passive film breaks down and causes pit initiation, that acts as precursor for SCC initiation. At the zone 2, passive film is in the initial stage of forming and the passive film is in metastable condition due to the transition from active to passive region. The passive film is not stable in both zone 1 and 2 and therefore the material is more susceptible to SCC. At the HIC zone, hydrogen evolution reaction (HER) occurs, that caused hydrogen damage on the material [20].

In order to understand if the metastable state of the passivation behavior of Mg-RE alloys leads to SCC, potentials within the transition zones were applied to the U-bend specimens and the SCC behavior was investigated. Fig. 5.13 shows images of post tested EV31A samples in different heat treatment conditions and different bias potentials in 0.1 M NaOH solution with 80 ppm Cl^-. Fig. 5.13(a) shows the failure of EV31A in peak-aged condition which was applied 1.6 $V_{Ag/AgCl}$ (transpassive potential). EV31A peak-aged sample failed by localized corrosion of the arms of U-bend specimen at the air/solution interface. There was no evidence of cracking at the strained region of the U-bend specimen. Therefore, it is shown that application of potential associated with zone 1 resulted in localized corrosion but not SCC. When the applied potential was -0.2 $V_{Ag/AgCl}$ (passive region, zone 2), EV31A peak-aged specimen showed uniform corrosion of the curved area, as seen in Fig. 5.13(b). Severe pitting corrosion occurred at the U-curve of the EV31A as-received specimen when the applied potential was -1.0 $V_{Ag/AgCl}$

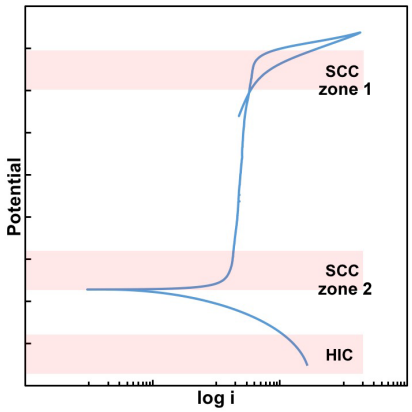

Fig. 5.12 The schematic polarization curve showing SCC susceptible zone and hydrogen induced cracking (HIC) zone.

(potential in zone 2), as seen in Fig. 5.13(c). When the applied potential was in the cathodic region, the failure time increased as compared to the open circuit condition. The EV31A as-received specimen was conditioned under galvanostatic condition at a current density of -10 mA/cm^2 that evolved hydrogen on the U-bend specimen surface. No crack initiation was observed even after 340 hours under the cathodically polarized hydrogen evolution condition. Fig. 5.13(d) shows the specimen surface after the galvanostatic cathodic polarization after 340 hours. The edges of the specimen were observed to be attacked possibly due to dissolution of MgH_2 phases that formed during the cathodic polarization. The formation of MgH_2 was confirmed by the XRD analysis as shown in Fig. 5.14. MgH_2 peaks were present on both tension side and compressive side of the specimen. Formation of the MgH_2 phase did not result in crack initiation on the specimen. Fig. 5.13(e) shows the cross-sectional area of WE43C peak-aged sample after SCC at the applied potential of 1.6 $V_{Ag/AgCl}$ (transpassive potential, zone 1). Application of high anodic potential caused accelerated SCC failure compared to the OCP condition. It could be seen that the sample failed in mixed mode. However, each fracture mode was uniformly distributed throughout the cross section. It was different from the samples failed by SCC at OCP (Figs. 5.7(a), and 5.10(a)) which had quite clear zones of separate intergranular and transgranular fracture modes. From Fig. 5.13(f), attack on specific crystallographic planes that resembled transgranular were present next to the intergranular fracture. In addition, the evidence of corrosion attack on the cracked region could be seen. Fig. 5.13(g) revealed transgranular fracture mode with the decohesion of precipitates.

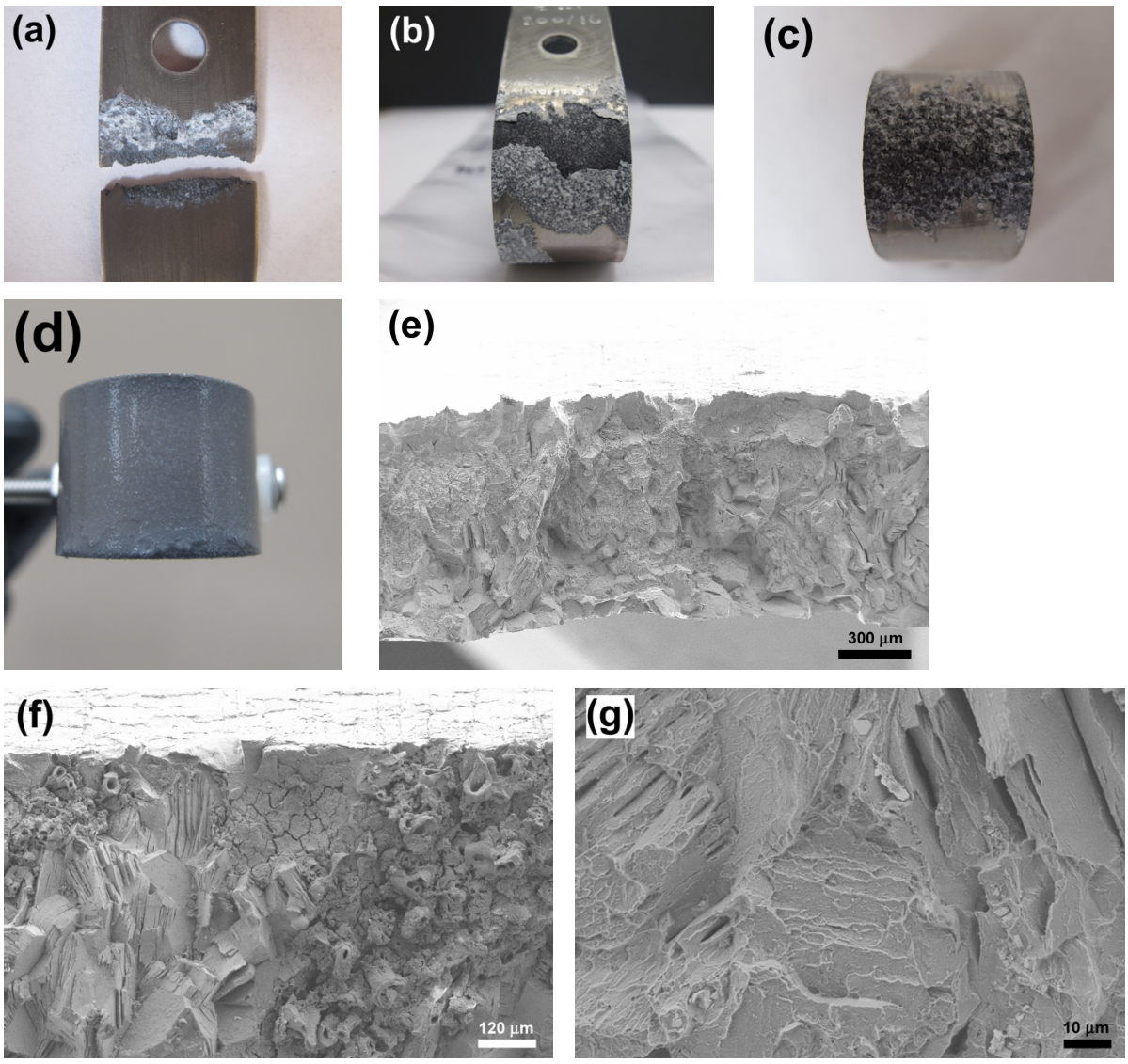

Fig. 5.13 EV31A sample in different heat treatment conditions which were applied the potential and current in different regions from Fig. 5.11 (unstressed plot) in 0.1 M NaOH solution with 80 ppm Cl^-; **(a)** EV31A peak-aged (E_{app} = 1.6 $V_{Ag/AgCl}$: transpassive potential), **(b)** EV31A peak-aged (E_{app} = -0.2 $V_{Ag/AgCl}$: passive region), **(c)** EV31A as-received (E_{app} = -1.0 $V_{Ag/AgCl}$: active/passive region), **(d)** EV31A as-received (i_{app} = -10 mA/cm^2: galvanostatic condition at hydrogen charge region), **(e)** cross-sectional view of WE43C peak-aged (E_{app} = 1.6 $V_{Ag/AgCl}$: transpassive potential), **(f)** mixed mode of fracture of WE43C peak-aged, and **(g)** transgranular mode of WE43C peak-aged.

Mg-RE alloys failed by SCC in the open circuit condition and applied anodic potentials, in general. Cathodic polarization resulted in formation of MgH_2 but prevented SCC initiation. EV31A showed mostly localized corrosion under applied anodic potentials, whereas WE43C-PA specimen showed mixed mode cracking under anodic potential in the transpassive region. These SCC results indicated that both film rupture and hydrogen adsorption were responsible for SCC. Corrosion layers were observed on the fracture surfaces. In order to understand the effect of passive layer on the hydrogen evolution, cathodic polarization was carried out on the

unstressed Mg-RE alloy coupons that were covered with surface layers. Initially the samples were conditioned at the open circuit condition in 0.1 M NaOH solution for 48 hours. A thick passive layer formed on the specimen surfaces during this OCP conditioning period. These samples were potentiostatically passivated at 0.5 $V_{Ag/AgCl}$ for 1 hour. Potentiodynamic polarization was carried out on these surface film covered specimens from OCP to -0.5 $V_{Ag/AgCl}$ vs OCP (~ -2.0 $V_{Ag/AgCl}$ vs reference) at a scan rate of 1 mV/s. Exchange current density for hydrogen evolution, and Tafel slope of the hydrogen evolution reaction (HER) were determined from the cathodic polarization plots and summarized in Table 5.3. For comparison, the results of cathodic polarization of freshly polished specimens are also included. The results indicated that presence of $Mg(OH)_2$ layer helped increase the exchange current density for the HER. Enhanced hydrogen evolution on the hydroxide covered magnesium was reported by other researchers [21, 22]. However, the Tafel slopes were higher on the surface oxide covered specimens than the Tafel slopes of freshly polished specimens. Figs. 5.15(a) – (d) shows the SEM images of the specimens after cathodic polarization. EV31A in as-received and peak-aged conditions showed significant amount of surface crack initiation on the surface film after cathodic polarization as seen in Figs. 5.15(a) and (b), while EV31A overaged and WE43C peak-aged specimens did not have cracks on the surface (Figs. 5.15(c) – (d)). The cracking tendency of the surface film of EV31A could not be related to the HER electrochemical parameters. The blisters present on the surface film would help hydrogen diffuse into the bulk of the specimen. Otherwise, in the presence of a surface layer, the diffusion of hydrogen into the specimen thickness would be slower because atomic hydrogen cannot diffuse through $Mg(OH)_2$ and diffusion will be in the form of H^+ [23].

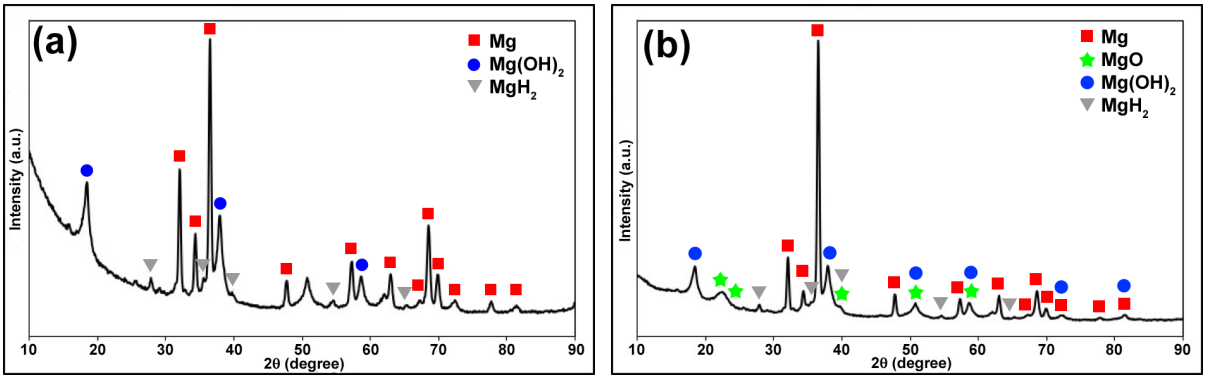

Fig. 5.14 XRD patterns of EV31A as-received specimen under galvanostatic condition at hydrogen charge region (applied current = -10 mA/cm^2); **(a)** tension side, and **(b)** compression side.

Table 5.3 Summary of the cathodic polarization results of the unstressed specimens.

Sample		Freshly polished specimen surface		Surface covered with passive layer	
		Tafel slope V/dec	Exchange current density for hydrogen evolution, i_0 A/cm^2	Tafel slope V/dec	Exchange current density for hydrogen evolution, i_0 A/cm^2
EV31A	AR	-0.14	1.3×10^{-11}	-0.27	5.5×10^{-9}
	PA	-0.29	5.0×10^{-8}	-0.24	1.2×10^{-8}
	OA	-0.17	5.5×10^{-10}	-0.24	2.5×10^{-8}
WE43C	PA	-0.24	2.3×10^{-8}	-0.28	3.0×10^{-8}

The accelerated failure of WE43C peak-aged specimen at a high anodic potential of 1.6 $V_{Ag/AgCl}$, and longer failure time or no failure at cathodic potentials of EV31A peak-aged specimens suggest that the SCC of Mg-RE alloys is determined by the stability of the surface layer of the alloys. Therefore, film rupture and dissolution could be the crack initiation mechanism. Once cracks initiated, the crack propagation was assisted by the hydrogen adsorption which reduced the surface energy of the crystallographic planes. Table 5.4 summarizes failure modes and time to failure of all specimens in the experiment.

Table 5.4 Summary of failure mode and time to failure of the specimens.

Material		Chloride conc. (ppm)	Electrochemical condition	Failure mode	Time to failure (day)
EV31A	AR	80	OCP	TGSCC/IGSCC	13
	PA	80	OCP	TGSCC/IGSCC	19
	OA	80	OCP	TGSCC/IGSCC	38
	AR	100	OCP	Pitting	> 20 (No crack)
	AR	200	OCP	Pitting	> 20 (No crack)
	PA	80	E_{app} = 1.6 $V_{Ag/AgCl}$	Pitting	3
	PA	80	E_{app} = -0.2 $V_{Ag/AgCl}$	Uniform	> 14 (No crack)
	AR	80	E_{app} = -1.0 $V_{Ag/AgCl}$	Pitting	> 14 (No crack)
	AR	80	i_{app} = -10 mA/cm^2	Hydrogen damage	> 14 (No crack)
WE43C	AR	80	OCP	Pitting	> 43 (No crack)
	PA	80	OCP	TGSCC/IGSCC	23
	AR	100	OCP	Pitting	> 40 (No crack)
	AR	200	OCP	Pitting	> 40 (No crack)
	PA	80	E_{app} = 1.6 $V_{Ag/AgCl}$	TGSCC/IGSCC	1

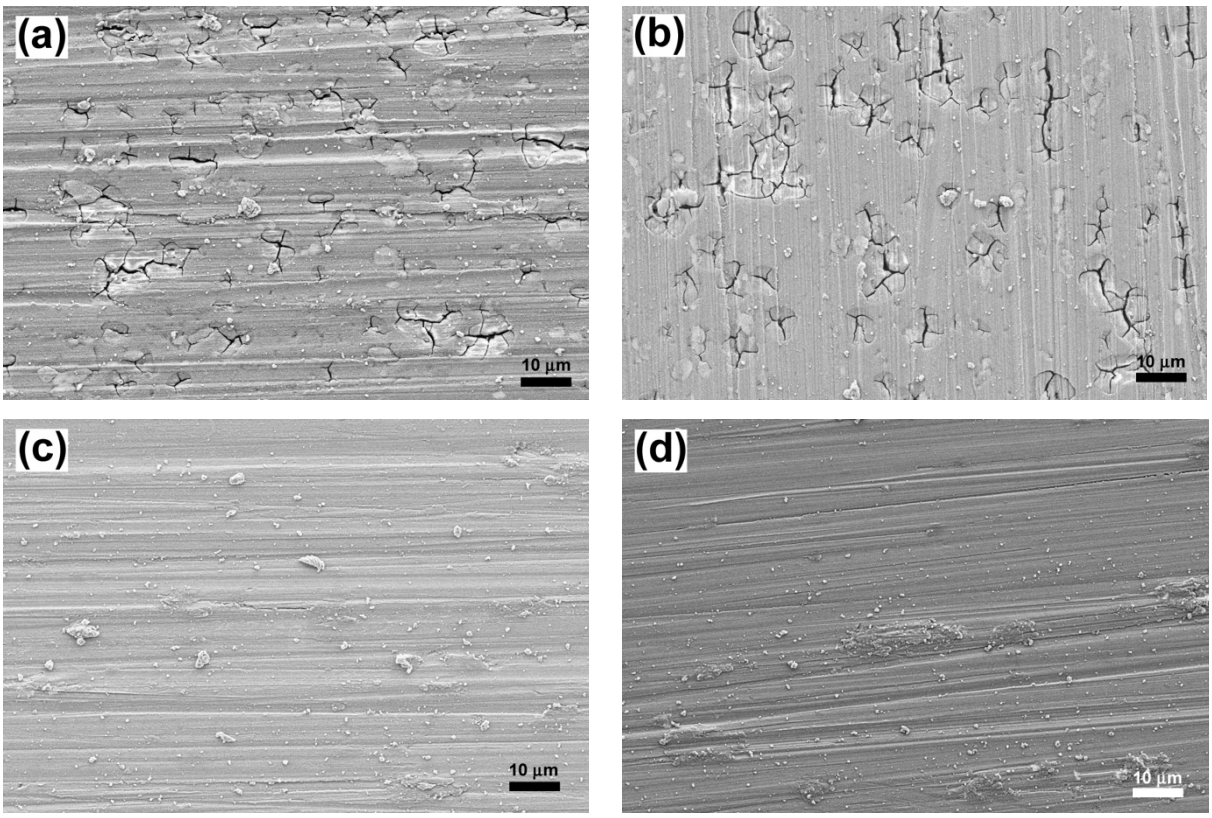

Fig. 5.15 SEM images of the unstressed specimens which were measured OCP for 48 h, followed by passivation for 1 h, and cathodic polarization in 0.1 M NaOH solution without chloride; **(a)** EV31A as-received, **(b)** EV31A peak-aged, **(c)** EV31A overaged, and **(d)** WE43C peak-aged.

5.4. Conclusions

SCC tests were carried out on the U-bend specimens of EV31A and WE43C specimens in 0.1 M NaOH solution with 80, 100, and 200 ppm Cl^- at room temperature under OCP and applied potentials. Based on the test results, the following conclusions can be drawn:

1. EV31A alloy in as-received and peak-aged conditions, and WE43C in peak-aged condition were susceptible to SCC in open circuit condition. Crack initiation of EV31A and WE43C in peak-aged condition started at localized corrosion site by anodic dissolution mechanism. In addition, cracks were present at the slip step region for WE43C.

2. SCC fracture of EV31A and WE43C revealed both intergranular and transgranular crack propagation.

3. Increasing chloride concentration did not increase susceptibility to SCC. On the other hand, the alloys were susceptible to localized corrosion.

4. Applied anodic potential in the metastable passive regions caused localized corrosion of EV31A specimens, and applied potential of 1.6 $V_{Ag/AgCl}$ caused accelerated SCC failure of WE43C peak-aged sample.

5. OCPs of EV31A and WE43C decreased when cracks initiated, and propagated. The OCP – time profile can be used for monitoring the SCC failure of Mg-RE alloy components in real life service conditions.

6. Overaged condition had the highest SCC resistance.

Acknowledgements

The support provided by the U.S. Nuclear Regulatory Commission through a faculty development grant NRC-HQ-84-15-G-0025 is gratefully acknowledged. J. Ninlachart acknowledges the support by Royal Thai Navy.

References

[1] G. Riontino, D. Lussana, M. Massazza, G. Barucca, P. Mengucci, R. Ferragut, Structure evolution of EV31 Mg alloy, J. Alloys Compd. 463 (2008) 200 – 206.

[2] Y.H. Kang, H. Yan, R.S. Chen, Creep behavior and microstructure evolution of sand-cast Mg-4Y-2.3Nd-1Gd-0.6Zr alloy crept at 523 - 573 K, J. Mater. Sci. Technol. 33 (2017) 79 – 89.

[3] N. Winzer, A. Atrens, G.L. Song, E. Ghali, W. Dietzel, K.U. Kainer, N. Hort, C. Blawert, A critical review of the stress corrosion cracking (SCC) of magnesium alloys, Adv. Eng. Mater. 7 (2005) 659 – 693.

[4] I. Polmear, Light Alloys From Traditional Alloys to Nanocrystals, fourth ed., Elsevier, Oxford, UK, 2007.

[5] M.B. Kannan, W. Dietzel, C. Blawert, A. Atrens, P. Lyon, Stress corrosion cracking of rare-earth containing magnesium alloys ZE41, QE22 and Elektron 21 (EV31A) compared with AZ80, Mater. Sci. Eng., A 480 (2008) 529 – 539.

[6] B.S. Padekar, V.S. Raja, R.K.S. Raman, P. Lyon, Stress corrosion cracking of a new rare-earth containing magnesium alloy Elektron 21 compared with AZ91E, Mater. Sci. Forum 690 (2011) 361 – 364.

[7] B.S. Padekar, V.S. Raja, R.K.S. Raman, P. Lyon, Stress corrosion cracking of rare-earth containing magnesium alloy EV31A compared with AZ91E using slow strain rate test, Proceedings of NACE International corrosion 2012 conference & expo (2012) 4470 – 4478.

[8] B.S. Padekar, R.K.S. Raman, V.S. Raja, P. Lyon, Stress corrosion cracking of a recent rare-earth containing magnesium alloy, EV31A, and a common Al-containing alloy, AZ91E, Corros. Sci. 71 (2013) 1 – 9.

[9] L. Choudhary, R.K.S. Raman, J. Hofstetter, P.J. Uggowitzer, In-vitro characterization of stress corrosion cracking of aluminium-free magnesium alloys for temporary bio-implant applications, Mater. Sci. Eng., C 42 (2014) 629 – 636.

[10] ASTM G30 - 97 (Reapproved 2003), Standard practice for making and using U-bend stress-corrosion test specimens, ASTM International, PA, USA, 2003.

[11] J. Ninlachart, K.S. Raja, Threshold chloride concentration for passivity breakdown of Mg-Zn-Gd-Nd-Zr alloy (EV31A) in basic solution, Acta Metall. Sinica (Engl. Lett.) 30 (4) (2017) 352 – 366.

[12] J. Ninlachart, K.S. Raja, Effect of heat treatment conditions on the passivation behavior of WE43C Mg-Y-Nd alloy in chloride containing alkaline environments, J. Magnesium Alloys DOI 10.1016/jma.2017.03.003.

[13] P.W. Chu, E.A. Marquis, Linking the microstructure of a heat-treated WE43 Mg alloy with its corrosion behavior, Corros. Sci. 101 (2015) 94 – 104.

[14] K.M. Ismail, S. Virtanen, Electrochemical behavior of magnesium alloy AZ31 in 0.5 M KOH solution, Electrochem. Solid-State Lett. 10 (3) (2007) c9 – c11.

[15] J. Ninlachart, K.S. Raja, Passivation Kinetics of Mg-Nd-Gd-Zn-Zr (EV31A) and Mg-Y-Nd-Gd-Zr (WE43C) in NaOH Solutions, J. Magnesium Alloys, Manuscript No. JMA-D-17-00030 (under review).

[16] J.X. Jia, G. Song, A. Atrens, Boundary element method predictions of the influence of the electrolyte on the galvanic corrosion of AZ91D coupled to steel, Mater. Corros. 56 (4) (2005) 259 – 270.

[17] M. Kappes, M. Iannuzzi, R.M. Carranza, Hydrogen embrittlement of magnesium and magnesium alloys: A review, J. Electrochem. Soc. 160 (4) (2013) c168 - c178.

[18] S.P. Lynch, P. Trevena, Stress corrosion cracking and liquid metal embrittlement in pure magnesium, Corrosion 44 (1988) 113 – 124.

[19] M. Iannuzzi, Are crack born from pits?, https://www.aboutcorrosion.com/2016/01/31/are-cracks-born-from-pits/, 2016 (accessed 4.1.17).

[20] D.A. Jones, Principles and prevention of corrosion second ed., Prentice-Hall, New Jersey, 1996.

[21] S.H. Salleh, S. Thomas, J.A. Yuwono, K. Venkatesan, N. Birbilis, Enhance hydrogen evolution on $Mg(OH)_2$ covered Mg surfaces, Electrochim. Acta 161 (2015) 144 – 152.

[22] G.L. Song, K.A. Unocic, The anodic surface film and hydrogen evolution on Mg, Corros. Sci. 98 (2015) 758 – 765.

[23] R.S. Stampella, R.P.M. Procter, V. Ashworth, Environmentally-induced cracking of magnesium, Corros. Sci. 24 (4) (1984) 325 – 341.

Appendix

Copyright letter of "Threshold Chloride Concentration for Passivity Breakdown of Mg-Zn-Gd-Nd-Zr Alloy (EV31A) in Basic Solution"

Springer license

Terms and conditions

Jun 11, 2017

This Agreement between Mr. Jakraphan Ninlachart ("You") and Springer ("Springer") consists of your license details and the terms and conditions provided by Springer and Copyright Clearance Center.

License Number	4126200655295
License date	Jun 11, 2017
License Content Publisher	Springer
License Content Publication	Acta Metallurgica Sinica (English Letters)
License Content Title	Threshold Chloride Concentration for Passivity Breakdown of Mg-Zn-Gd-Nd-Zr Alloy (EV31A) in Basic Solution
License Content Author	Jakraphan Ninlachart
License Content Date	Jan 1, 2017
License Content Volume	30
License Content Issue	4
Type of Use	Book/Textbook
Requestor type	Publisher
Publisher	ProQuest Dissertation Publishing
Portion	Full text
Format	Print and Electronic
Will you be translating?	No
Print run	1
Author of this Springer article	Yes and you are the sole author of the new work
Country of republication	other

Order reference number	
Title of new book	Electrochemical Investigation on Environmental Degradation of Magnesium Rare Earth Alloys
Publisher	ProQuest Dissertation Publishing
Author of new book	Jakraphan Ninlachart
Expected publication date of new book	Jul 2018
Estimated size of new book (pages)	130
Requestor Location	Mr. Jakraphan Ninlachart 875 Perimeter Drive MS 1021 MOSCOW, ID 83844 United States Attn: Mr. Jakraphan Ninlachart
Billing Type	Invoice
Billing Address	Mr. Jakraphan Ninlachart 875 Perimeter Drive MS 1021 MOSCOW, ID 83844 United States Attn: Mr. Jakraphan Ninlachart
Total	0.00 USD

Terms and Conditions

Introduction

The publisher for this copyrighted material is Springer. By clicking "accept" in connection with completing this licensing transaction, you agree that the following terms and conditions apply to this transaction (along with the Billing and Payment terms and conditions established by Copyright Clearance Center, Inc. ("CCC"), at the time that you opened your Rightslink account and that are available at any time at http://myaccount.copyright.com).

Limited License

With reference to your request to reuse material on which Springer controls the copyright, permission is granted for the use indicated in your enquiry under the following conditions:

- Licenses are for one-time use only with a maximum distribution equal to the number sated in your request.

- Springer material represents original material which does not carry references to other sources. If the material in question appears with a credit to another source, this permission is not valid and authorization has to be obtained from the original copyright holder.

- This permission

- is non-exclusive
- is only valid if no personal rights, trademarks, or competitive products are infringed.
- Explicitly excludes the right for derivatives.

- Springer does not supply original artwork or content.

- According to the format which you have selected, the following conditions apply accordingly:

- **Print and Electronics:** This License include use in electronic form provided it is password protected, on intranet, or CD-Rom/DVD or E-book/E-journal. It may not be republished in electronic open access.
- **Print:** This License excludes use in electronic form.
- **Electronics:** This License only pertains to use in electronic form provided it is password protected, on intranet, or CD-Rom/DVD or E-book/E-journal. It may not be republished in electronic open access.

For any electronic use not mentioned, please contact Springer at permissions.springer@spi-global.com.

- Although Springer controls the copyright to the material and is entitled to negotiate on rights, this license is only valid subject to courtesy information to the author (address is given in the article/chapter).

- If you are an STM Signatory or your work will be published by an STM Signatory and you are requesting to reuse figures/tables/illustrations or single text extracts, permission is granted according to STM Permissions Guidelines: http://www.stm.-assoc.org/permissions-guidelines/

For any electronic use not mentioned in the Guidelines, please contact Springer at permissions.springer@spi-global.com. If you request to reuse more content than stipulated in the STM Permissions Guidelines, you will be charged a permission fee for the excess content.

Permission is valid upon payment of the fee as indicated in the licensing process. If permission is granted free of charge on this occasion, that does not prejudice any rights we might have to charge for reproduction of our copyrighted material in the future.

- If your request is for reuse in a Thesis, permission is granted free of charge under the following conditions:

This license is valid for one-time use only for the purpose of defending your thesis and with a maximum of 100 extra copies in paper. If the thesis is going to be published, permission needs to be reobtained.

- includes use in an electronic form, provided it is an author-created version of the thesis on his/her own website and his/her university's repository, including UMI (according to the definition on the Sherpa website: http://www.sherpa.ac.uk/romeo/);

- is subject to courtesy information to the co-author or corresponding author.

Geographic Rights: Scope

Licenses may be exercised anywhere in the world.

Altering/Modifying Material: Not Permitted

Figures, tables, and illustrations may be altered minimally to serve your work. You may not alter or modify text in any manner. Abbreviations, additions, deletions and/or any other alterations shall be made only with prior written authorization of the author(s).

Reservation of Rights

Springer reserves all rights not specifically granted in the combination of (i) the license details provided by you and accepted in the course of this licensing transaction and (ii) these terms and conditions and (iii) CCC's Billing and Payment terms and conditions.

License Contingent on Payment

While you may exercise the rights licensed immediately upon issuance of the license at the end of the licensing process for the transaction, provided that you have disclosed complete and accurate details of your proposed use, no license is finally effective unless and until full payment is received from you (either by Springer or by CCC) as provided in CCC's Billing and Payment terms and conditions. If full payment is not received by the date due, then any license preliminarily granted shall be deemed automatically revoked and shall be void as if never granted. Further, in the event that you breach any of these terms and conditions or any of CCC's Billing and Payment terms and conditions, the license is automatically revoked and shall be

incorporated herein), comprise the entire agreement between you and Springer (and CCC) concerning this licensing transaction. In the event of any conflict between your obligations established by these terms and conditions and those established by CCC's Billing and Payment terms and conditions, these terms and conditions shall control.

Jurisdiction

All disputes that may arise in connection with this present License, or the breach thereof, shall be settled exclusively by arbitration, to be held in the Federal Republic of Germany, in accordance with German law.

Other conditions:

V 12AUG2015

Questions? customercare@copyright.com or +1-855-239-3415 (toll free in the US) or +1-978-646-2777.